



저작자표시-비영리-변경금지 2.0 대한민국

이용자는 아래의 조건을 따르는 경우에 한하여 자유롭게

- 이 저작물을 복제, 배포, 전송, 전시, 공연 및 방송할 수 있습니다.

다음과 같은 조건을 따라야 합니다:



저작자표시. 귀하는 원저작자를 표시하여야 합니다.



비영리. 귀하는 이 저작물을 영리 목적으로 이용할 수 없습니다.



변경금지. 귀하는 이 저작물을 개작, 변형 또는 가공할 수 없습니다.

- 귀하는, 이 저작물의 재이용이나 배포의 경우, 이 저작물에 적용된 이용허락조건을 명확하게 나타내어야 합니다.
- 저작권자로부터 별도의 허가를 받으면 이러한 조건들은 적용되지 않습니다.

저작권법에 따른 이용자의 권리는 위의 내용에 의하여 영향을 받지 않습니다.

이것은 [이용허락규약\(Legal Code\)](#)을 이해하기 쉽게 요약한 것입니다.

[Disclaimer](#)

공학박사 학위논문

생체 의료용 폴리우레탄 기반 복합체 개발

**Advanced polyurethane based composites for biomedical
applications**

2019년 2월

서울대학교 대학원

공과대학 재료공학부

송은호

생체 의료용 폴리우레탄 기반 복합체 개발

Advanced polyurethane based composites for biomedical applications

지도교수 김 현 이

이 논문을 공학박사 학위논문으로 제출함

2018 년 12 월

서울대학교 대학원

재료공학부

송 은 호

송 은 호의 박사 학위논문을 인준함

2018 년 12 월

위 원 장 안 철 희 (인)

부위원장 김 현 이 (인)

위 원 선 정 윤 (인)

위 원 김 석 화 (인)

위 원 고 영 학 (인)

Abstract

Advanced polyurethane based composites for biomedical applications

Eun Ho Song

Department of Materials Science and Engineering

Seoul National University

Polyurethane has many advantages as a tissue engineering scaffold used in various biomedical applications, including tunable wide range of mechanical property, chemical stability in physiological condition, inherent porous structure resulting from simple foaming reaction, and bio-inert property. However, its bio-inert property of polyurethane has limitation to accelerate the tissue regeneration or healing process as an advanced scaffold for complex medical problems. Thus, it is important to enhance biological property of polyurethane by modifying the chemical structure and incorporating biomolecules such as bioceramics, glass, or growth factors. In this work, we suggested three kinds of new composite systems; 1) silica incorporation through *in situ* sol gel process during foaming reaction, 2) stable and accelerated hydroxyapatite mineralization on phosphate groups conjugated on polyurethane chain, and 3) covalently linked BMP-2 by di-sulfide with thiolated polyurethane. We systematically demonstrated the improvement on biological property of the chemically modified polyurethane through well developed *in vitro* and *in vivo* evaluation and confirmed its potential to be

used as actual medical applications, including dressing material, cartilage replacement and drug delivery scaffold.

Polyurethane (PU)-based dressing foams have been widely used due to their excellent water absorption capability, good mechanical properties, and unequaled economic advantages. However, low bioactivity and poor healing capability of PU have limited the applications of PU dressings to complex wound healing cases. In this study, in order to improve healing capability of PU, bioactive silica nanoparticles have been hybridized with PU through a one-step foaming reaction coupled with the sol-gel process. The hybridization with silica didn't affect the intrinsic porous microstructure of PU foams at up to 10 wt% silica content, where 5~60 nm silica nanoparticles were well dispersed in the PU matrix. The incorporated silica enhanced the mechanical performance of PU to have better flexibility and durability, and maintained the good water absorption capability and WVTR characteristics of pure PU foam. Silica of PU-10wt% Si foams was gradually dissolved and released under physiological conditions during 14 days. The *in vitro* cell attachment and proliferation tests showed that the biocompatibility of PU-Si hybrid foams was significantly improved, demonstrating the silica effect on cell growth. More importantly, compared to PU-treated wounds, the healing capability of PU-Si as a wound dressing was verified through the *in vivo* animal tests. From the tests, full-thickness wounds treated with PU-Si foams exhibited the faster wound closure rates along with an accelerated collagen and elastin fiber regeneration in newly formed dermis, which became completely covered with new epithelial layer. Therefore, PU-Si hybrid foams have considerable potential as a wound dressing material for accelerated and superior wound healing.

Second, glycerol phosphate was introduced into polyurethane (PU) to promote the coating stability of hydroxyapatite (HA) during its mineralization on the PU surface. Glycerol phosphate was successfully conjugated with the PU chain during polymerization. Phosphate groups in glycerol phosphate accelerated the nucleation of HA under calcium phosphate ion-rich conditions (concentrated simulated body fluid), resulting in the enhancement in structural stability. The robust interface between HA and PU also improved mechanical properties. Hydrophilic phosphate groups and bioactive HA improved *in vitro* cellular responses in terms of the attachment and proliferation of

L929 fibroblasts and MC3T3-E1 preosteoblasts. Thus, the highly elastic and bioactive PU-gp-HA could be a promising candidate for tissue engineering applications that experience frequent deformation, including diverse cartilage replacements. Two candidates could be chosen for elastic PU-gp-HA system to be utilized; auricular prosthesis, and menisci replacement. To match the mechanical property of the natural cartilage, further mechanical enhancement should be performed. Densification process applying heat and pressure to deform the porosity and structure was chosen. The porosity of dense PU-gp-HA (PUH) was easily controlled (30%, 10%, and 7%) by adjusting the compressive pressure (5, 1000, 2000 kgf). The strength and elastic modulus of the densified PUH were significantly higher than those of the porous PUH because HA were trapped as fillers inside the densified matrix. Its biocompatibility beneath the soft tissue was evaluated by analyzing the degree of capsular contracture as a sort of foreign body reaction. PUH showed better cellular response, resulting in thin capsule thickness and loose collagen density since HA profoundly alleviated the foreign body reaction and enhance biocompatibility of the implant. Finally, auricular prosthesis was also successfully fabricated as designed in metal mold. In addition, Inspired by the anisotropic structure of natural menisci, porous and densified layers PUH, were alternately stacked to fabricate a biomimetic multilayered scaffold. Each layer was highly attached, resulting in good interfacial stability, resulting in good interfacial stability. The scaffold was stiff along the x- and y-directions and more flexible along the z-axis (the stacking direction), as designed.

Lastly, thiolated biodegradable polyurethane (TG-DPU) was synthesized using a one-pot reaction with thioglycerol adopted as a functionalized chain extender. After characterization of the chemical structure of TG-DPU using proton nuclear magnetic resonance spectroscopy, bone morphogenic protein (BMP-2) was loaded in the TG-DPU under oxidative conditions to form disulfides between the free thiol of TG-DPU and BMP-2. The interaction between TG-DPU and BMP-2, so-called bioconjugates, was investigated using X-ray photoelectron spectroscopy analysis; the appearance of disulfide (S–S) linkage indicated the formation of a polymer/growth factor conjugate system. The covalently linked bioconjugates provided stability with minimal loss during the drug delivery with prolonged release performance in *in vitro* release tests. The effects of the drugs delivered by TG-DPU

were also confirmed by *in vitro* alkaline phosphatase tests using pre-osteoblasts and *in vivo* bone regeneration tests. The drugs effectively induced cell differentiation and promoted mature bone recovery.

Keywords: Polyurethane, Silica, Sol-gel process, Wound healing, Dressing, Mineralization, hydroxyapatite, Cartilage, Auricle, Menisci, Thiol, Di-sulfide, Polymer-growth factor conjugate, drug delivery, scaffold, sustain release, bone graft

Student Number: 2015-20833

Contents

Abstract.....	iii
List of Tables.....	ix
List	of
Figures.....	x

Chapter 1. Introduction

1.1 Polyurethane scaffolds for biomedical applications.....	2
1.2 Synthesis of polyurethane and functionalization process.....	2

Chapter 2. Polyurethane-silica hybrid foams from a one-step foaming reaction, coupled with a sol-gel process, for enhanced wound healing

2.1 Introduction.....	5
2.2 Experimental procedure.....	6
2.3 Results and discussion.....	11
2.4 Conclusion.....	18

Chapter 3. Phosphate conjugated polyurethane with induced mineralized hydroxyapatite composite for elastic cartilaginous tissue replacements

3.1 Promoting the nucleation of hydroxyapatite on glycerol phosphate-conjugated polyurethane for the enhancement of bioactivity	
3.1.1 Introduction.....	31

3.1.2 Experimental procedure.....	32
3.1.3 Results and discussion.....	35
3.1.4 Conclusion.....	38
3.2 Densified polyurethane/hydroxyapatite composite for cartilaginous applications	
3.2.1 Introduction.....	45
3.2.2 Experimental procedure.....	48
3.2.3 Results and discussion.....	51
3.2.4 Conclusion.....	56

Chapter 4. Use of thioglycerol on porous polyurethane as a theranostic capping agent for bone tissue engineering

4.1 Introduction.....	67
4.2 Experimental procedure.....	68
4.3 Results and discussion.....	73
4.4 Conclusion.....	77

Chapter 5. Conclusion

5.1 Conclusion.....	87
5.2 Further works.....	87

References.....	90
------------------------	-----------

Abstract (Korean).....	102
-------------------------------	------------

Curriculum Vitae.....	104
------------------------------	------------

List of Tables

Table 1. Water absorption property and WVTR of PU and PU-Si

Table 2. Dermis Thickness, and relative density of collagen and elastin fiber in wound regions treated with gauze, PU and PU-10 wt% Si foams after 14 days, normalized by those in the intact skin regions

Table 3. Mechanical Properties (Strength, Strain at Failure, and Stiffness) of PU, PU-gp, and PU-gp-HA

Table 4. Anisotropic modulus of natural meniscus and multilayered PUH scaffold

List of Figures

Figure 2.1. SEM images of PU and PU-Si foams: (A, B) Cross-section images of PU (A) and PU-Si (B), and (C, D) high resolution images of PU (C) and PU-Si (D).

Figure 2.2. TEM images of silica nanoparticles dispersed in PU matrix at (A) low and (B) high magnification for PU-Si.

Figure 2.3. (A) FT-IR transmission spectrum of PU and PU-Si membranes (ν : stretching, δ : bending), and (B) TGA curve.

Figure 2.4. Mechanical properties of PU and PU-Si ($n=3$, $*p < 0.05$ and $p < 0.005$), (A) Representative stress-strain curve and (B) tensile modulus and elongation at break of PU and PU-Si**

Figure 2.5. Si ion release from PU-Si after immersing in SBF solution at 37 °C for 14 days

Figure 2.6. (A) CLSM images of fibroblasts after 1d-cell attachment to the surface of PU, and PU-Si membranes, and (B) cell proliferation of fibroblasts after culturing for 5 and 7 days ($n=3$, $*p < 0.05$)

Figure 2.7. Wound-healing rate of three dressing materials: (A) Macroscopic appearance of incised wounds in three wound dressing materials (gauze, PU and PU-Si)

at different time points (scale bar = 10mm) and (B) remaining defect area after 3, 7 and 14 days treatment with gauze, PU and PU-Si membranes (n = 3, *p < 0.05).

Figure 2.8. Histological and immunohistochemistry examination of the wound regions treated with gauze, PU, and PU-Si dressings after 14 days: (A) representative H&E staining images of the wound regions, (B) Masson's trichrome (MT) staining images of the collagen matrix in the wound regions and (C) van Gieson staining images of the elastin fibers in the wound regions after the removal of the covered wound dressing. O/D: original dermis, N/D: newly formed dermis

Figure 3.1.1. (A) Schemes of (1) PU-gp and (2) PU-gp-HA formation; (B) solid state P-NMR results according to existence of glycerol phosphate with chemical structure of designed PU-gp-HA and (C) SEM images of surfaces of PU-gp-HA at different precipitation time (0 , 4, and 12 h) (scale bar = 10 μ m)

Figure 3.1.2. HA morphology images at different mineralization stage according to the glycerol phosphate composition and mineralization time (scale bar : 20 μ m)

Figure 3.1.3. XRD peaks of PU-gp-HA (4 and 12 h treated specimens). The asterisk indicates the characteristic peaks of hydroxyapatite.

Figure 3.1.4. Stress-strain curve of PU, PU-x wt% gp, and PU-x wt% gp-HA (x=2.5 and 10) (n=3).

Figure 3.1.5. (A) Remaining HA amount of PU-HA and PU-gp-HA before and after sonication for 30 min, calculated based on TGA results. Surface morphology of (B) PU-HA and PU-gp-HA after sonication. The asterisk indicates statistically significant p-values of ** $p < 0.01$ with $n=3$ (scale bar = 10 μm)

Figure 3.1.6. In vitro fibroblasts (A, B, and C) and osteoblasts (D, E, and F) attachment cultured for 1 day (scale bar = 10 μm) and MTS analysis for 3 and 5 days (G and H). The asterisk indicates statistically significant p-values of * $p < 0.05$ and ** $p < 0.01$ with $n=3$ (scale :10 μm)

Figure 3.2.1. (A) μ -CT images of porous PUH foam and densified PUH 30, PUH 10, and PUH 7. The number indicates the porosity of each group. (B) 2D μ -CT images of XY, YZ, and ZX planes of PUH 10 sample.

Figure 3.2.2. FT-IR spectra of porous PUH and densified PUH 10

Figure 3.2.3. SEM images of (A) PUH foam and (B) outer surface and (C) cross-section of densified PUH 10. (D) High-magnification image of HA on PUH 10 surface (the arrows identify mineralized HA particles on the surface).

Figure 3.2.4. (A) Representative stress–strain curves of densified PU 10 and densified PUH (PUH 30, PUH 10, and PUH 7). (B) UTS and (C) stiffness change of densified PU and PUH (porosity: 30%, 10%, and 7%). (* $p < 0.05$, ** $p < 0.01$)

Figure 3.2.5 Histological evaluation of collagen capsule extracted from rat dorsal skin after 2 and 6 weeks of PU and PUH implantation

Figure 3.2.6 PU and PUH treated capsule thickness obtained from 2 week histology images

Figure 3.2.7 (A) metal mold designed from STL files to print auricle prosthesis and (B) PUH microtia after being inserted beneath the dorsal tissue of nude mice (balb/c, male)

Figure 3.2.8 (A) Cross-sectional SEM image of multilayered PUH and (B) representative stress–strain curves of multilayered PUH and porous PUH.

Figure 3.2.9 Representative stress–strain curves of multilayered structure: (A) compression test parallel to the stacking direction and (B) tensile test perpendicular to the stacking direction.

Figure 4.1. Schemes of synthesis of biodegradable polyurethane and thioglycerol conjugation

Figure 4.2. ¹H-NMR results of PU (TDI), DPU, and TG-DPU in the range of 0–6 ppm of chemical shift. Representative peaks corresponding to the PCL segment and conjugated thiols are denoted by the letters.

Figure 4.3. (A) Degradation profile for different PCL diol contents of DPU and (B)

surface morphology after being immersed for 14 days

Figure 4.4. (A) CLSM images of DPU and TG-DPU loaded with GFP after release for 0, 1, 4, and 7 days (scale = 500 μ m), (B) BMP-2 release profile of DPU-B (control group, PCL diol: 25 wt%) and TG-DPU-B (thioglycerol contents; 0.05 wt%, 0.1 wt%, and 0.2 wt%, and PCL diol: 25 wt%)

Figure 4.5. XPS spectra for TG-DPU, DPU-B, and TG-DPU-B, showing analysis of the interaction at the interface of BMP-2 and the scaffolds: (A) characteristic peak assigned to sulfur in 163-eV region and (B) schemes of TG-DPU-B forming covalent (-S-S-) and hydrogen bonds at the molecular level

Figure 4.6. (A) MTS results of DPU, TG-DPU, DPU-B, and TG-DPU-B (cell density: 3×10^4) after 3 and 5 days of culturing. (B) ALP activity (cell density: 0.5×10^4) after 14 days of culturing on DPU, TG-DPU, DPU-B, and TG-DPU-B, using ATCC pre-osteoblasts (*p < 0.05)

Figure 4.7. (A) CT images of rabbit calvaria treated with DPU, TG-DPU, DPU-B, and TG-DPU-B after 4 weeks of monitoring. The arrows indicate new bone regeneration inside the defects. (B) Quantitative analysis of bone coverage calculated using CTan software. (*p < 0.05)

Figure 4.8. Histology images ((A) $\times 2$ and (B) $\times 15$ magnification) of DPU, TG-DPU, DPU-B, and TG-DPU-B stained by Goldner's trichrome. (A) Overall view of defects recovered after 4 weeks (scale: 1 cm). (B) Newly generated tissues were investigated at

higher magnification, as sectioned with red boxes (scale: 100 μm). The connective tissues were loose and light blue and were not transformed into bones. The new bones were stained cyan blue and became darker as the tissues maturized. Osteocytes were embedded in the new bones as white round shapes.

Figure 5. Various applications of PU based material for further works

Chapter 1.

Introduction

1.1 Polyurethane scaffolds for biomedical applications

In tissue engineering application, systematically designed scaffold fabrication with adequate mechanical property, using appropriate material is essential for restoration, and recovery of damaged tissue [1]. The most fundamental demands on material selection for successful tissue engineering are biocompatibility and biochemical stability [2]. The higher the biological property, the better the completion for tissue regeneration without any signs of cytotoxicity. In addition to a good biological property, mechanical unity between implants and original tissue should be satisfied [3]. According to the targeting applications, required mechanical property varied; for wound dressing, scaffold should possess elastic property rather than just tough and stiff, or for articular cartilage replacement, the anisotropic moduli is needed [4, 5]. So the material which has a wide range of variability in elastic modulus, or strength is desirable in various tissue engineering applications. Besides, porous structure is mostly favorable in tissue engineering applications; (1) providing wet environment, and facilitating gas transfer for wound healing, (2) substituting the damaged tissues while possessing the space for cell infiltration similar with extracellular matrix and new tissue formation in terms of bone implants, and (3) having a large surface area for drugs to be carried in drug delivery system [1].

Polyurethane is one of the most appropriate biomaterials which can fulfill these requirements. It is chemically stable in physiological condition that it could be utilized as a drug carrier where the urethane protects the drug from exterior environments effectively [6]. Also it is biocompatible that there already are commercial urethane products in blood vessels, and textured coating in breast implants [7, 8]. Its mechanical property can be varied with the choice and composition of chain extender, and polyol in molecular level. Moreover, polyurethane scaffold is inherently formed into porous structure as a generated carbon dioxide gas during the foaming reaction without further additives.

1.2 Synthesis of polyurethane and functionality

Polyurethane is synthesized by reacting a monomer, containing two or more isocyanates per

molecule ($R-(N=C=O)_n$, $n \geq 2$) with a chemical agent which has two or more alcohol ($R'-OH$) or amines ($R''-NH_2$). The chemicals are called chain extender and polyol according to the molecular length. If alkyl groups are polymeric chain, a repetition of units, it is called polyol, otherwise a chain extender. They were reacted with monomer following the different reaction mechanisms according to the functional groups (hydroxyl groups or amines). Hydroxyl groups of the most of polyol and chain extender form urethane linkage ($-NHCOO-$) as reacted with monomer. Peculiarly, water ($H-OH$), a representative chain extender used to fabricate polyurethane, reacts exceptionally with monomers to form urea linkage ($-NHCONH-$), evolving CO_2 gas which generates inherent pores. On the other hands, amines directly formed urea bonds reacted with isocyanates. Physical property of polyurethane is determined by the type and amount of the polyol or chain extender to be reacted besides monomer species [9]. In most cases, flexibility is contributed by the polyol, in other words, soft segments, while rigidity is influenced by the chain extender, hard segment. So, mechanical property of polyurethane can be controlled easily by changing the composition of soft and hard segment.

Moreover, other advanced functions, including biodegradability, biocompatibility, induced mineralization, and improved affinity to biomolecules (peptide, proteins, drugs, etc) can be attributed to polyurethane, using a special polyol or chain extender to improve the bio-inert property of urethane itself. Herein, we introduced advanced methods to give biologically meaningful functions to polyurethane for various biomedical applications. In chapter 2, polyurethane/inorganic composite phase is introduced to accelerate wound healing process as a dressing material, incorporating silica sol-gel fabrication procedure with urethane polymerization step at once. Chemical structure of polyurethane was also modified to get highly improved bioactivity through promotion of CaP mineralization and stable and sustain drug carrying capability, by adopting a functionalized chain extender to introduce phosphate or thiol groups over the polymer chain, explained in detail in Chapter 3 and 4 respectively.

Chapter 2.

Polyurethane-silica hybrid foams from a one-step foaming reaction, coupled with a sol-gel process, for enhanced wound healing

2.1 Introduction

Various wound dressings have been widely used for decades as a practical way to treat skin wounds, by protecting the wound site from the risk of exterior impact and providing proper hydrated conditions for the wound/dressing interface through alleviating dehydration rates and absorbing excessive exudates [10, 11]. Among conventional wound dressing materials, hydrophilic polyurethane (PU) foam is one of the most widely used materials due to its excellent water absorption capability, good mechanical properties, and unequaled economic advantages [12-14]. Polyurethanes are produced by step-growth polymerization between a polyisocyanate and a polyol, in the presence of various additives (e.g., catalysts, crosslinkers, surfactants, hardeners, softeners, and blowing agents) [15-18]. In particular, hydrophilic PU foams are often obtained using a one-step foaming and polymerization reaction using toluene diisocyanate (TDI)/polyethylene glycol (PEG)-based prepolymer in water and with or without additions [19]. The physiological properties of the PU foams, such as hydrophilicity, water absorption ratio and water vapor transmission rate (WVTR), can be tuned by the type and amount of an addition [20, 21]. Those hydrophilic PU foams have been applied to severe wound cases, which have a great deal of exudates, and the PU foams can absorb excessive exudates effectively through its distinctive porous structure while providing adequate moisture over the wound area [22]. In addition, the PU-based dressing foams are not only more economical than other dressing materials made of natural polymers such as collagen, chitosan, gelatin, and fibrin but they also have mechanically outstanding properties in terms of having excellent flexibility and tensile strength even after being fully soaked in water [23-25].

In spite of physiological, mechanical, and economic advantages over other dressing materials, the PU foams still have poor healing capability, and are regarded as a passive wound dressing [26]. As such, bioactive additives such as growth factors (e.g., endothelial growth factor), biomolecules (e.g., dextrans) or cells (e.g., keratinocytes, adipose-derived stem cells) have been introduced to the PU foam dressings to improve their healing capability, particularly, for the treatment of complex wounds that cannot be cured by conventional dressings [27-31].

Silica nanoparticles are also one of the bioactive additives tested for PU-based dressings and in this context, they have a great potential in three aspects. First, it is reported that silica could accelerate wound healing by directly or indirectly stimulating the proliferation of fibroblasts. Our previous study on chitosan-silica dressing materials proved that by incorporating silica nanoparticles into the chitosan matrix, nanocomposites exhibited accelerated wound healing with fast wound closure and collagen regeneration [32]. Around the wound site, the released silicon ions promoted the inflammatory cells, which induce the secretion of growth factors (e.g., TNF- α , TGF- β), and turn on the complex wound healing cascade. Silica was also found to directly stimulate proliferation of human lung fibroblasts without any biosynthetic activities [33]. Second, because of the well-known hemostatic capability of silica, silica-incorporated dressing materials (e.g., polyphosphate, chitosan) exhibited significantly enhanced hemostasis ability, which is an important factor for innate wound healing [32, 34]. Lastly, silica has been applied as a reinforcing agent for various polymer systems [35-38]. PU-Si nanocomposites in particular have shown a great improvement on mechanical performance even with a small amount of silica nanofillers [39].

Therefore, in this study, polyurethane-silica (PU-Si) hybrid foams were fabricated as a wound dressing material with a one-step polymerization and foaming reaction of PU, coupled with a sol-gel process of silica. PU-Si hybrid foams with different silica contents were characterized through structural, chemical, mechanical, and physiological analysis and the amounts of silicon ion released from the hybrid was quantified. Biocompatibility and bioactivity of PU-Si was evaluated through *in vitro* cellular tests in terms of the silica content. Also, the wound healing capability of PU-Si was demonstrated through *in vivo* experiments that included wound size assessments and histological analysis in conjunction with immunohistochemistry and performance compared to PU and gauze.

2.2 Experimental procedures

Preparation of PU and PU-Si foams

HYPOL 2002, a toluene diisocyanate (TDI)/hexamethylene diisocyanate (HDMI)-based

prepolymer of polyurethane (PU), was supplied by Dow Chemical Co Ltd. (UK branch). Other chemicals including glycerol and tetramethylorthosilane (TMOS) were purchased from Sigma-Aldrich USA. PU and PU-Si hybrid foams were synthesized by a sol-gel process and foaming reaction in one step. HYPOL 2002 (3 g) and glycerol (0.3 g) were mixed with distilled water (6 g) to produce a 5 g PU foam. For PU-Si, silica sol was prepared at a molar ratio of 1:10 of TMOS: distilled water in acidic conditions, according to our published protocol [40]. The prepared silica sol was mixed with HYPOL 2002, glycerol and distilled water simultaneously and according to predetermined weight ratios of 0 wt%, 5wt%, and 10 wt% of silica to PU. The mixtures were poured into a plastic mold with dimensions of 5 cm×5 cm×5 cm. After a 10 min foaming reaction, the PU and PU-Si foams were carefully washed with distilled water five times and were dried overnight at 37 °C in air. The final thickness of the PU and PU-Si foams was 4 to 5 mm.

Structural and chemical analysis of PU-Si hybrid foams

The surface morphology and micro-structure of pure PU and PU-Si composite foams were observed by scanning electron microscopy (normal SEM, JSM-5600, JEOL, Tokyo, Japan) and field emission transmission electron microscopy (FE-TEM, JEM-3000F, JEOL, Tokyo, Japan). The TEM specimens were prepared by pouring the 1:100,000 diluted PU-Si liquid mixture into a copper grid, and drying the grid at 37 °C overnight.

The infrared spectra of the PU and PU-Si hybrid foams were analyzed using a Fourier-transform infrared (FT-IR) spectrometer (Nicolet Magma 550 Series II Midac, USA) at wavelengths ranging from 400 to 4000 cm^{-1} with an average of 64 scans. The actual quantity of silica nanoparticles in the PU-Si foams was measured by thermogravimetric analysis (TGA) in nitrogen condition at up to 600 °C and at a heating rate of 20 °C/min rate.

Mechanical tests of PU and PU-Si foams

The mechanical properties of the PU and PU-Si foams were measured using a tensile testing instrument (Model 5565, Instron Corp., Danvers, MA, USA). Specimens with a thickness of 1 mm were prepared and were cut into a rectangular shape with dimensions of 5 mm×25 mm. Tensile load

was applied at an extension rate of 1 mm/min ($n = 5$). The tensile modulus, ultimate tensile strength and elongation at break were obtained from the stress-strain curves of each specimen group.

Water absorption tests of PU and PU-Si foams

Specimens (pure PU, PU-5wt% Si, PU-10wt% Si) with dimensions of 1 cm×1 cm×0.5 cm were immersed in 5 ml of phosphate-buffered saline (PBS) at 37 °C. The weight of the specimens was measured after being fully swollen for a day. Prior to weighing, any water remaining on the membrane surface was removed by filter papers. The water absorption ratios were calculated by the following:

$$\text{Water absorption per volume (g/cm}^3\text{)} = (W_s - W_d) / V_d$$

In the equation, W_d and V_d represent the weight and volume of dried membranes, respectively and W_s indicates the weight of the fully swollen membrane ($n = 5$).

Water vapor transmission rate (WVTR) of PU and PU-Si foams

For measuring the water vapor transmission rate (WVTR), all the specimens were prepared as a disc shape with a diameter of 4.5 cm and a thickness of 5 mm. The prepared samples were placed on the beaker containing 20 g of distilled water while the gap between the beaker and specimens was tightly sealed by a Teflon tape in an incubator at 37 °C. The WVTR was determined as follows:

$$\text{WVTR (g/m}^2\text{/day)} = (W_0 - W_t) / (S \times t) \times 24$$

For the above, W_0 and W_t are the weights of the whole system at the first and second hours respectively, S is the transmitting area of the sample, and t is the time interval.

Release profile of silicon ion of PU-Si foams

The amount of silicon ions released from PU-10 wt% Si was evaluated by an inductively coupled plasma mass spectrometer (ICP, Varian 820-MS, Varian, Australia). Each PU-10 wt% Si specimen with dimensions of 10 mm×10 mm×5 mm was immersed in the 10 ml PBS solution at 37 °C ($n = 3$). At each predetermined time (0, 3, 7 and 14 days), the aqueous solution was extracted for the measurement of released ions and then the solution was replaced.

***In vitro* tests**

To assess the biological property of PU and PU-Si, *in vitro* cell attachment and proliferation tests were carried out using fibroblast cells (L929). Cells at the density of 3×10^4 cells/ml were seeded on the samples in the alpha-minimum essential medium (Welgene Co., Ltd., Korea) with 10 % fetal bovine serum (FBS), and 1 % penicillin-streptomycin. Cell attachment evaluation was performed 1 day after culturing. For this, the cells were fixed with 4 % paraformaldehyde in PBS for 10 min, then rinsed with PBS and treated with 0.1 % Trion X-100 in PBS for 5 min. Cells were again rinsed with PBS and stained with phalloidin (Alexa Fluor® 55 phalloidin; Invitrogen, Carlsbad, CA, USA) for 20 min, followed by staining of the nuclei with 4, 6-diamidino-2-phenylindole (DAPI) (ProLong® Gold antifade reagent with DAPI; Invitrogen) for 5 min. The stained samples were observed by a confocal laser scanning microscope (CLSM, FluoView FV1000; Olympus, Japan). Cell viability was characterized by the MTS assay (CellTiter 96 Aqueous One Solution; Promega). After 5 and 7 days of culturing, the post-treatment for MTS was performed. Specimens were washed with PBS, transferred to 24 well tissue culture polystyrene plates. They were then immersed in the alpha-minimum essential medium excluding FBS, with the detection reagents and incubated at 37 °C for 2 hours. The absorbance of the formazan products by mitochondrial activity in viable cells was measured at 492 nm using a microreader (Model 550; Bio-Rad, USA).

***In vivo* animal tests**

The *in vivo* study was performed under approved protocol (no. 12-0226) by the Institutional Animal Care and Use Committee (IACUC) of Seoul National University. The use and handling of the animals abided by the Guide for the Care and Use of Laboratory Animals of Seoul National University. The *in vivo* experiments with PU-Si foams were performed using our previously developed rodent model with nine, 6-week-old male Sprague-Dawley rats for the validation of improved wound healing capabilities compared to gauze and PU foams [32]. All animals were pathogen free and were maintained using the same diet and environmental conditions. After a weeklong adaptation period, the healthy animals were selected for use in the experiments. After the

anesthesia and hair removal, two full-thickness square wounds with dimensions of 10 mm×10mm were created on the dorsum per animal in order to minimize the circular contractile force, which is known to retard contraction to some degree [41]. Each wound was covered with one of three dressing materials, (control), each with dimensions of 15 mm×15 mm squares. For the fixation of dressing materials, each wound was additionally covered with a thin film (transparent OPSITE film, Smith & Nephew, London, UK), and subsequently fixed with non-adhesive ACETM (3M, USA). Lastly, the animal body was wrapped with polyethylene cylindrical guards to prevent the peeling or fouling of the materials. The dressing materials were carefully changed every 3 days as not to interrupt the healing process. At days 14 after surgery, the animals were sacrificed using CO₂ asphyxiation in accordance with the American Veterinary Medical Association Guidelines for the Euthanasia of animals, and the tissues were subsequently harvested. In our previous study [32], we confirmed that 14 days were sufficient to prove this early stage wound healing behavior using a rodent model since.

Wound size assessment On 0, 3, 7, 14 days after surgery, the optical images of all wounds were taken to assess wound healing. The size of the defect area was quantified using the National Institutes of Health Image J 1.36b imaging software (National Institutes of Health, Bethesda, MD, USA). As compared to the original wound size at day 0, the ratio of remaining defect area (remaining defect area/original wound area at day 0) was calculated using Image J software for area measurements (National Institutes of Health) [32].

Histological analysis and Immunohistochemistry Rats were sacrificed after 14 days post surgery. The tissues from the wound area including the surrounding normal skin tissue were harvested *en bloc*, sectioned and fixed in 10 % formalin overnight, and stored in 70 % alcohol at 4 °C prior to being embedded in paraffin. After being washed carefully, the stored tissues were embedded in paraffin and sectioned into slices perpendicular to the wound surface. The tissue slices were stained according to three protocols; hematoxylin and eosin (H&E), Masson's trichrome (MT) and van Gieson protocols [42-44]. The optical images of each stained histological section were analyzed for three parameters: 1) regenerated dermis thickness of the wound region, normalized by the old dermis thickness of the intact surrounding tissue; 2) collagen density of the wound region, normalized by the

collagen density of the intact surrounding tissue; and 3) elastin fiber density of the wound region, normalized by the elastic fiber density of the intact surrounding tissue. For measurement of the stained collagen and elastic fiber density in the wound and the intact surrounding tissue areas, the total pixel intensity of optical images was determined using the Image J program

2.3 Results and discussion

Structural analysis of PU and PU-Si foams

The surface morphologies of PU and PU-Si foams were investigated by SEM, as shown in **Figure. 2.1**. The one-step polymerization and foaming reaction of PU prepolymers in water includes the reaction between the isocyanate groups of toluene diisocyanate (TDI) and water, which generates carbon dioxide (CO₂) gas as a by-product [45]. Generated CO₂ gas is attributed to the distinctive porous structure of PU foam with high porosity and outstanding pore interconnectivity. The apparent porosity of PU and PU-Si was measured by the image analysis. All PU and PU-Si foams were highly porous, having the porosity of > 85 %. The average pore diameter of PU and PU-Si was in the range of 450 - 500 μm (**Figure. 2.1(A) and (B)**). There were no significant differences in porosity and pore size between all the PU and PU-Si foams samples at up to 10 wt% Si, implying that the silica sol in the mixture didn't deter the foaming reaction. The high resolution images of PU and PU-10 wt% Si also showed similar surface morphologies as in **Figure. 2.1(C) and (D)**, where there is no prominent feature of PU-10 wt% Si related to the incorporated silica nanoparticles. Since most hybridized silica nanoparticles were embedded in the PU matrix, the surface morphologies of PU and PU-Si were almost identical [46]. The PU-Si foams with more than 10 wt% of silica were found to have low structural integrity due to their non-homogenous pore structures (data not shown), as the excessive amount of silica interrupted the foaming reaction of PU [39]. Thus, in this study, two PU-Si foams, PU-5wt% Si, and PU-10wt% Si were fabricated and evaluated compared to pure PU.

The incorporated silica nanoparticles were assessed using TEM in terms of their size and phase in addition to the distribution of nanoparticles embedded in the PU matrix for PU-10 wt% Si, as

seen in **Figure. 2.2**. The size of spherical silica nanoparticles varied from 5 nm to 60 nm while some parts were slightly agglomerated, forming bigger particles with a size of ~ 200 nm. The higher resolution image also shows a large portion of nanoparticles having a diameter of ~ 5 nm, which may undergo fast dissolution in water due to their small size [47].

In order to quantify the amount of silica nanoparticles in PU-5 wt% Si and PU-10 wt% Si, those hybrid foams were analyzed by TGA (**Figure. 2.3(A)**). The amount of silica was calculated by subtracting the remnant of pure PU from the residue contents of PU-Si at 600°C. The empirical values of the silica contents (3 wt% for PU-5 wt% Si and 8 wt% for PU-10 wt% Si) were found to be different from the theoretical values. This discrepancy might be due to the loss of silica nanoparticles exposed on the surface of the hybrid foams during the multiple cleaning processes. This could also explain why the silica nanoparticles were not observed on the surface of the PU-Si foams, as seen in **Figure. 2.1(D)**. Moreover, silica nanoparticles with a diameter of less than 5 nm were likely dissolved during the cleaning process due to too fast dissolution rates.

Figure. 2.3(B) shows the FT-IR spectra of pure PU and PU-10 wt% Si foams. Characteristic peaks of urethane bonding were detected in both PU and PU-Si samples, including peaks at 1600-1700 cm^{-1} , 3400 cm^{-1} and 750-1150 cm^{-1} , which are associated with C=O, N-H, and C-O stretching vibrations, respectively. On the other hand, characteristic peaks of silica were only observed for PU-Si: Si-O-Si stretching at 1072, and 792 cm^{-1} and Si-OH stretching at 930 cm^{-1} [48]. Besides the PU or silica-related characteristic peaks, no other significant peaks were observed. Therefore, it can be concluded that there was no undesirable chemical reactions, implying that PU and silica likely maintain their inherent properties in the hybrid system [49].

Mechanical behavior of PU-Si foams

It is desirable for dressing materials to possess comparable flexibility to human skin, and high durability, which accommodates various skin deformations [50]. To address the mechanical performance of PU and PU-Si foams, three material parameters—tensile modulus, tensile strength and elongation at break—were obtained from the tensile tests (**Figure. 2.4**). First, the tensile moduli of

three foam systems appeared in a range of 500 kPa to 1.3 MPa, where the increased silica contents enhanced the stiffness of the hybrid foam. It has been known that the stiffness of human skin is either 0.85 MPa or 0.42 MPa when being applied a strain or a twist, respectively [51]. Even though the stiffness of PU-Si foams was increased by a factor of 1.5-2 along with the addition of silica, the values still are comparable to those of skin, implying that the hybrid foams are sufficiently flexible as a dressing material. Second, regarding the durability, strength and elongation at break of the hybrid foams exhibited significant improvement compared to pure PU. Particularly, PU-10 wt% Si foams likely endure about 2 times higher loads and stretch 3 times longer than PU does. The unusual mechanical enhancement of PU-Si hybrids is related to the unique deformation mechanism of PU associated with its chemical structure. PU consists of hard and soft segment domains. Under external force, the hard segment endures the load, being tilted and aligned toward the stretching direction instead of being deformed, while the soft segment dissipates the energy, being stretched [39]. Therefore, PU has high tensile strength, simultaneously exhibiting outstanding extensibility. According to Bistracic et al. [52], the incorporated silica nanoparticles interact with PU through dipole-dipole intermolecular forces between the Si-O group of silica and hydrophilic functional groups of PU, which enables silica to provide additional hard segments to the PU matrix. Consequently, the increased number of effective hard domains enhances stiffness and tensile strength of hybrid systems, yet allowing larger deformation of the soft segment before failure. Tien and Wei also discussed that the increased extensibility of PU-Si was attributed to silica acting as a chain extender of PU, and generating longer polymer chains [53]. Interestingly, the large amount of silica (>10 wt%) was reported to make the PU chains too stiff, significantly decreasing durability [39]. The reasonable flexibility and significantly increased durability of PU-Si could broaden the applications of PU-based foams, particularly for the cases where higher mechanical durability is required.

Physiological properties of PU-Si foams

One of the major advantages of PU foams for the wound treatment is its capability to maintain a good moisture environment for the wound region through outstanding water absorption

and vapor permeability [54-56]. Water absorption capability and vapor permeability of PU, PU-5wt% Si, PU-10wt% Si were evaluated and are indicated in **Table 1**. The intrinsic hydrophilic nature of PU allows the highly porous PU forms to absorb large amounts of water. As silica content increased, the amount of water absorption per volume slightly appeared to decrease, but there was no statistical difference in water absorption capability. Similarly, all PU and PU-Si foams showed the water vapor transmission rate (WVTR) of 800 – 1200 g/cm²/day, and the values of WVTR for all foams were not significantly different. Therefore, regardless of the silica content, PU foams preserve their water absorption capability and vapor permeability. Particularly, all PU-based foams in this study exhibit identical vapor permeability to that of commercial PU foams (Medifoam ® N, Korea), having a WVTR of > 800 g/m²/day [57]. Since 10 wt% Si in PU appeared to promote the highest mechanical enhancement while maintaining water absorption and permeation capabilities of PU, PU-10wt% Si was investigated for *in vitro* biological behavior and *in vivo* wound healing compared to pure PU.

***In vitro* release behavior of PU-Si foams**

Prior to evaluation of the silica effect on the *in vitro* biological performance of hybrid foams, the release behavior of silica from PU-Si was investigated, as shown in **Figure. 2.5**. It is found that about 80 ppm of silicon ions was released per day from the hybrid foam up to the initial three days after the foams were fully immersed in PBS under physiological conditions. The amount of released silicon ions was consistent among the tested specimens, showing less than 5% standard deviation. Unlike most natural polymer-based dressing materials, PU-based dressing materials have been applied to wound regions and are typically replaced every two or three days [20]. Therefore, based on both the usage time of the typical PU foam and the release profile of PU-10wt% Si, the hybrid system appears to continuously provide ~80 ppm of silica ions per 3 days over the whole wound healing period.

***In vitro* cell behavior of PU-Si foams**

Cytocompatibility of PU and PU-Si was evaluated with cell attachment and proliferation assays using fibroblasts as shown in **Figure. 2.6**. The cell attachment images on PU and PU-Si foams

clearly show the improved affinity of the hybrid foams to cells (**Figure. 2.6(A)**). On the PU surface, very few cells were found after 1 day of culture. On the other hand, on the PU-10 wt% Si foams, a much higher number of cells were observed than those on PU, indicating that the cell-surface affinity of hybrid foams was significantly enhanced. In addition, the viability of fibroblast cells on the PU and PU-Si foams was tested on days 5 and 7 of culturing by the MTS assay (**Figure. 2.6(B)**). The quantitative MTS results also demonstrated that the PU-Si hybrid foams significantly promote cell proliferation compared to pure PU ($p < 0.05$). Since there were minimal structural differences between PU and PU-Si, it could be concluded that the incorporated silica enhanced cytocompatibility of PU, improving cell attachment and proliferation on the PU-based dressing forms, whereas PU itself clearly exhibited bioinertness, with low cell affinity. The enhanced cell affinity due to incorporated silica was also observed in our previous study, where chitosan-silica hybrid systems showed improved cell attachment and proliferation compared to pure chitosan [32].

***In vivo* responses of PU-Si composite membranes**

The wound healing capability of PU-Si foams was further evaluated with the *in vivo* excision wound model and analyzing for two parameters: wound size assessment and histological properties of the wound (**Figure. 2.7 and 2.8**). The full-thickness wound regions were treated with PU and PU-10 wt% Si foams, using gauze as a negative control.

First, any size changes of remaining defect areas over time were observed and quantified as shown in **Figure. 2.7**. The optical images of defects in 3 groups (gauze as negative control, PU as positive control, PU-10 wt% Si) were captured on 0, 3, 7, 14 days post wounding (**Figure. 2.7(A)**). In case of PU and PU-Si-treated groups, the wound regions appear almost closed after 14 days, whereas the gauze-treated group still exhibited considerable defect regions for the treatment period. In order to compare the PU and PU-Si treated groups more clearly, the remaining defect regions of each wound were also quantitatively measured as shown in **Figure. 2.7(B)**. In our previous study [32], we found that in case of gauze and PU dressing foams, wounds were fully recovered after three weeks. Thus, in this study, we performed the wound size assessment at those four pre-determined times for 14 days

since 14 days were sufficient to prove the accelerated wound healing behavior of dressing materials at early wound healing stage [58-60]. The PU-Si hybrid-treated group showed consistently faster recovery than the other two groups during 14 days. The wound region treated with PU foams exhibited almost similar healing rates to that treated with gauze for the initial 7 days. However, beyond 7 days, the healing rate of the PU-treated group was higher than that of the gauze-treated group. The large standard deviation of the gauze-treated group was attributed to the tissue adherence of gauze that likely caused damage to newly formed tissue around the defect region. In case of PU-based dressing foams, non-adhesiveness to the wound surface was observed with minimal damage during dressing removal. Moreover, after 14 days of treatment, the gauze-treated group shows the dehydration around the remaining defect region as seen in **Figure. 2.7(A)**. The reduced period for healing at the early stage improved the healing process, leading to faster recovery from wounds. PU-Si treated wounds showed constantly faster closure rates than the other two dressing options at later stages. Therefore, silica contributed to higher wound closure rates for the PU-Si hybrid-treated group compared to the pure PU-treated group, as also observed in the chitosan-silica system in our previous study [61]. It should be noted that the accelerated wound-healing rate by silica for PU-based systems was more prominent than that for chitosan due to the inherent bioinertness of PU compared to a relatively more bioactive chitosan.

The wound regions treated by the three types of wound dressing were also investigated through histologically coupled with immunochemistry. After 14 days post wounding, tissues from the wound regions of sacrificed animals were harvested and stained with hematoxylin & eosin (H&E) for the overall tissue features, masson's trichrome (MT) for collagen, and van Gieson staining for elastin fiber as shown in **Figure. 2.8**, where the borders between the wound and abutting normal tissue are indicated with dashed lines. Moreover, the quantitative data of the new dermis regions are also tabulated in terms of thickness, collagen density and elastic fiber density relative to the intact dermis of the surrounding tissue around the wound region in **Table 2**. H&E results of Gauze, PU, and PU-Si treated groups are shown in **Figure. 2.8(A)**.

From the H&E images, the thicknesses of newly formed dermis and epidermis around the

wound were carefully observed. In case of the gauze-treated group, newly formed dermis (N/D) of the wound region was thinner than old dermis (O/D) of the abutting intact tissue with the absence of the epithelial layer. On the other hand, both PU and PU-Si treated groups exhibit N/D with a similar thickness to that of O/D. The quantitative data of N/D thickness for the three groups was obtained in terms of the thickness ratio of N/D and O/D (**Table 2**). The thickness of N/D was $87 \pm 6.4 \%$ and $88.6 \pm 2.4 \%$ for PU and PU-Si treated groups respectively, whereas $74 \pm 7.2 \%$ of N/D appeared in gauze-treated groups. More importantly, only the PU-Si treated group had a complete epithelial layer covering the underlying N/D, as indicated with white arrows in **Figure. 2.8(A)**.

In order to evaluate the density of regenerated collagen and keratin in N/D, MT-stained images, where collagen and keratin were stained into blue and red, respectively, were obtained and quantitatively analyzed (**Figure. 2.8(B)** and **Table 2**). Low density of regenerated collagen in N/D decreases the elasticity of recovered wound regions, inducing mechanical mismatch between the new and old skin tissues [62]. For successful wound recovery, a comparable density of regenerated collagen to that of collagen in O/D should be achieved. Among the three groups, the PU-Si treated group showed an almost identical contrast between O/D and N/D with the full-covering epithelial top layer, with the relative N/D collagen density of $99.6 \pm 4.9 \%$. However, both PU and gauze-treated groups had significantly lower relative N/D collagen density of $79.2 \pm 5.4 \%$ and $76.2 \pm 3.0 \%$, respectively, compared to that of the PU-Si treated group.

Figure. 2.8(C) shows the van Gieson stained images for the regenerated elastin fiber. The remodeling stage, the last step in the healing cascade, includes the process for the reconstruction of randomly organized regenerated collagen fibers through cross-linking with structural proteins [63]. Elastin, in fiber form, has been known as one of the main structural proteins for skin, increasing the elasticity of dermis. Through the van Gieson staining method, the elastin fibers are stained in brown, as shown in **Figure. 8(C)**. The relative density of N/D elastin fiber is also indicated in **Table 2**. The elastin-fiber stained images were consistent with the collagen/keratin stained images in demonstrating the superiority of PU-Si healed wounds. The density of regenerated elastin fibers in N/D reached $92.0 \pm 0.4 \%$ of elastin fiber density in O/D for the PU-Si treated group, which was significantly different

from both the PU and gauze-treated groups. Relative elastin fiber density ($70.7 \pm 7.5 \%$ and $61.6 \pm 6.1 \%$) of the PU and gauze groups didn't show a significant difference.

PU-Si dressing foams clearly demonstrated their enhanced healing effects through the *in vivo* full thickness excision model. The hybrid foams accelerated the wound closure rate, exhibiting consistently smaller remaining defect areas for the PU-Si treated group than those of the PU-treated group during the whole wound healing period. Incorporated silica nanoparticles in PU-Si were released as silicon ions, which likely promoted the proliferation of epidermal keratinocytes and dermal fibroblasts. In particular, there are highly proliferated fibroblasts that synthesize and cross-link collagen, and secrete growth factors (e.g., IGF) that engage in re-epithelization and granulation tissue formation [63, 64].

As seen with the silica-containing PU foams, epidermis and dermis of the wound region were perfectly formed, being almost identical to those of the abutting intact skin tissue in terms of thickness and composition (e.g., collagen and elastin fiber density) [65]. On the other hand, the acceleration of wound healing by silica was also attributed to the innate hemostatic property of silica nanoparticles produced by the sol-gel process as the inherent polar surfaces of the nanoparticles acted as contact activators of the intrinsic blood coagulation cascade [66]. Faster blood coagulation associated with an earlier thrombin burst was observed with the existence of silica, resulting in a shortened period of the early wound healing phase [34, 63]. Even though the early-stage healing effects of PU-Si dressing foams were clearly observed through the rodent model, efficacy and complete healing mechanisms of the hybrid forms are not clear. Thus, the improved wound healing behavior of PU-Si needs further evaluation through porcine models which are more close to human skin.

2.4 Conclusions

In this study, PU-Si hybrid foams were successfully fabricated in a one-step foaming reaction coupled with the sol-gel process. The hybridization with silica didn't affect the intrinsic porous

microstructure of PU foams at up to 10 wt% silica content, where 5~60 nm silica nanoparticles were well dispersed in the PU matrix, yet forming slight agglomeration. The incorporated silica enhanced the mechanical performance of PU with better flexibility and durability, and maintained the good water absorption capability and WVTR characteristics of pure PU foam. Silica of PU-10wt% Si foams was gradually dissolved and released under physiological conditions during 14 days of immersion. The *in vitro* cell attachment and proliferation tests showed that the biocompatibility of PU-Si hybrid foams was significantly improved, demonstrating the silica effect on cell growth. More importantly, compared to PU-treated wounds, the healing capability of PU-Si as a wound dressing was verified through the *in vivo* animal tests. From the tests, the full-thickness wounds treated with PU-Si foams exhibited the faster wound closure rates along with an accelerated collagen and elastin fiber regeneration of newly formed dermis, which became completely covered with new epithelial layer. Therefore, PU-Si hybrid foams have considerable potential as a wound dressing material for accelerated and superior wound healing.

Tables

Table 1. Water absorption property and WVTR of PU and PU-Si

	PU	PU-5 wt% Si	PU-10 wt% Si
Water absorption property (g/cm³)	5048 ± 740.1	4550 ± 790.8	4202 ± 586.6
WVTR (g/cm²/day)	1238 ± 146.6	817 ± 78.1	895 ± 60.7

Table 2. Dermis Thickness, and relative density of collagen and elastin fiber in wound regions treated with gauze, PU and PU-10 wt% Si foams after 14 days, normalized by those in the intact skin regions

	Gauze	PU	PU-Si
Dermis thickness (%) *	74 ± 7.2	87 ± 6.4	88.6 ± 2.4
Relative collagen density (%) *	76.2 ± 3.0	79.2 ± 5.4	99.6 ± 4.9
Relative elastin fiber density (%) *	70.7 ± 7.5	61.6 ± 6.1	92.0 ± 0.4

***The three factors to determine the maturity of new skin formation was quantitatively calculated by Image J software**

Figures

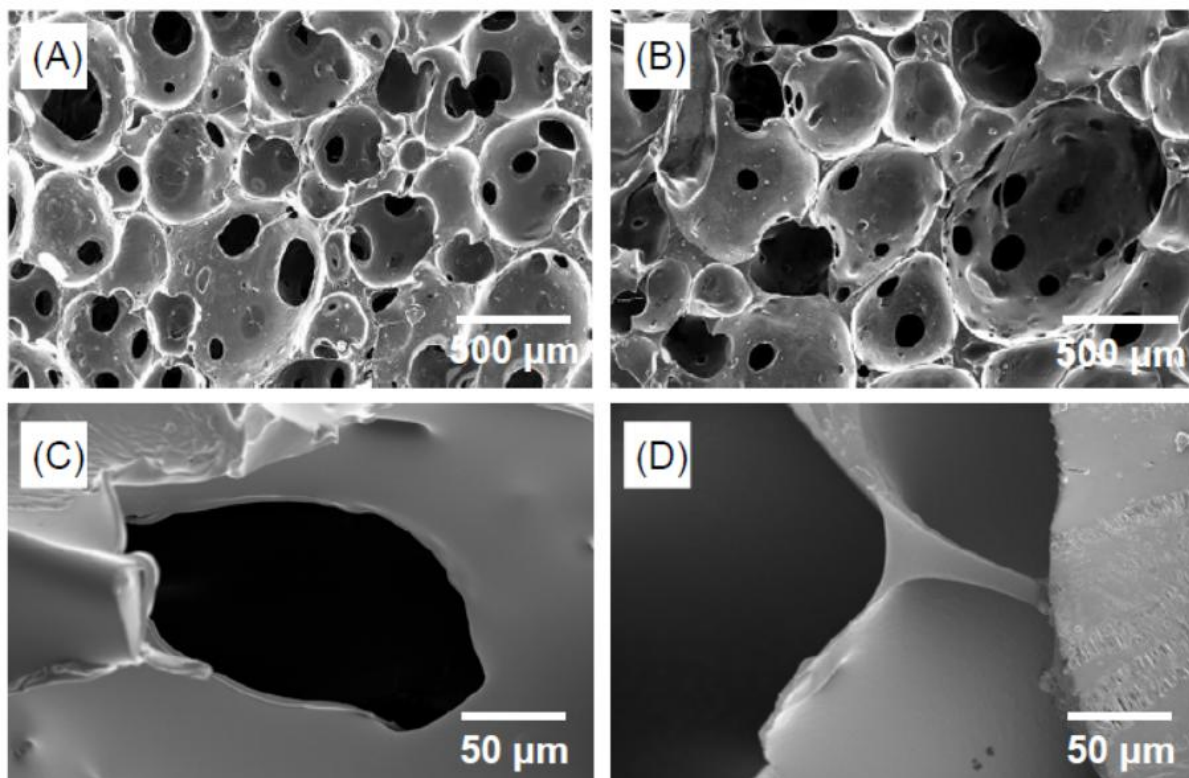


Figure 2.1. SEM images of PU and PU-Si foams: (A, B) Cross-section images of PU (A) and PU-Si (B), and (C, D) high resolution images of PU (C) and PU-Si (D).

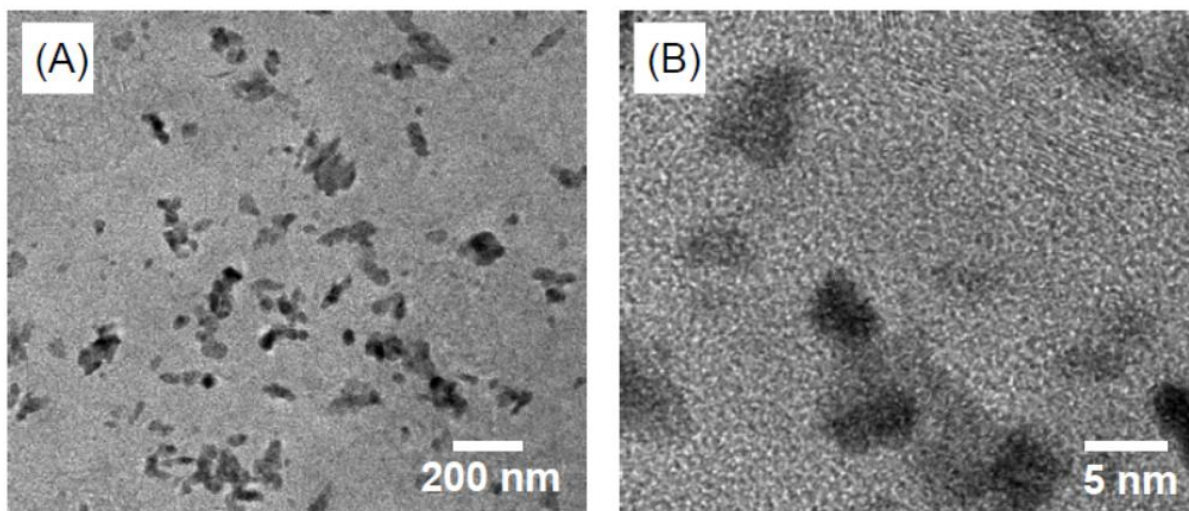


Figure 2.2. TEM images of silica nanoparticles dispersed in PU matrix at (A) low and (B) high magnification for PU-Si

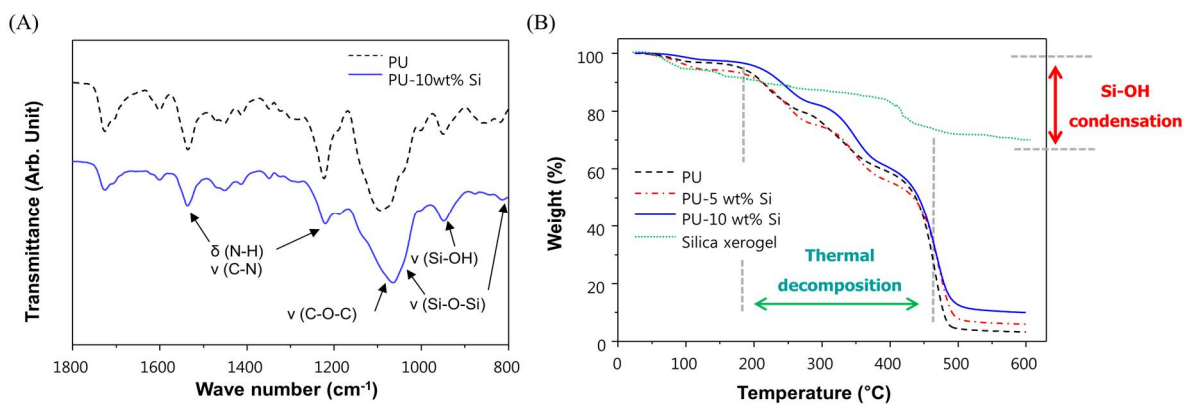


Figure. 2.3. (A) FT-IR transmission spectrum of PU and PU-Si membranes (ν : stretching, δ : bending), and (B) TGA curve

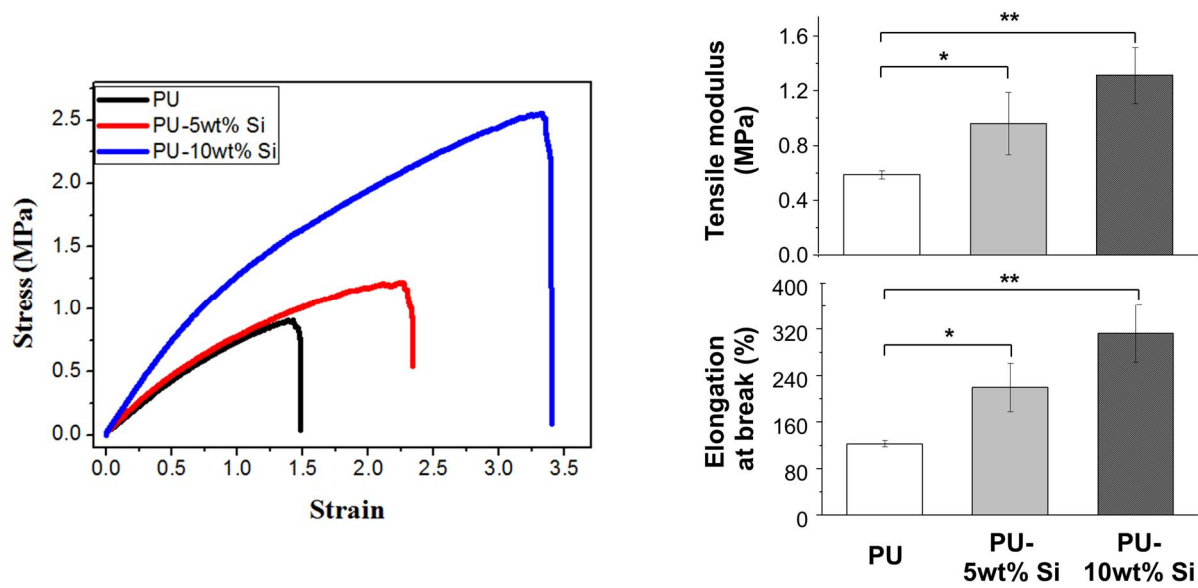


Figure. 2.4. Mechanical properties of PU and PU-Si (n=3, *p < 0.05 and **p < 0.005), (A) Representative stress-strain curve and (B) tensile modulus and elongation at break of PU and PU-Si

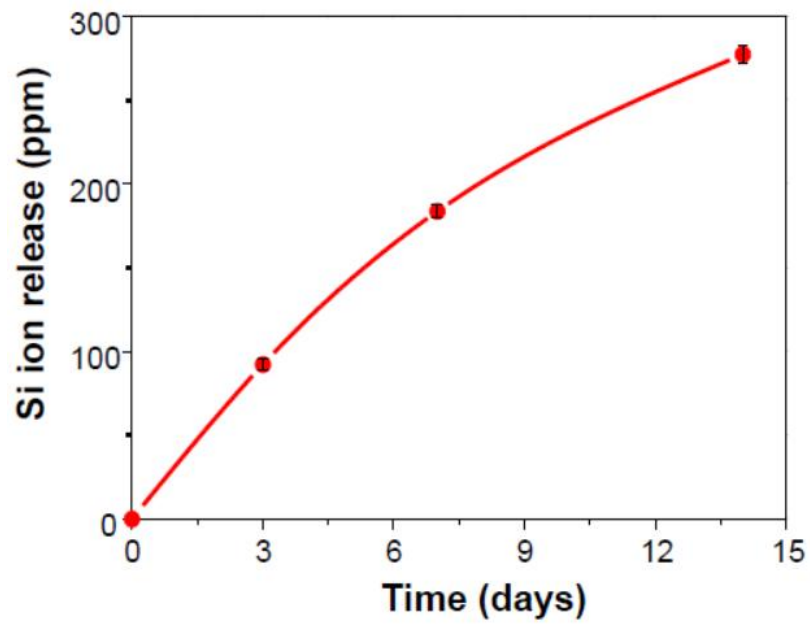


Figure. 2.5. Si ion release from PU-10 wt% Si after immersing in SBF solution at 37 °C for 14 days

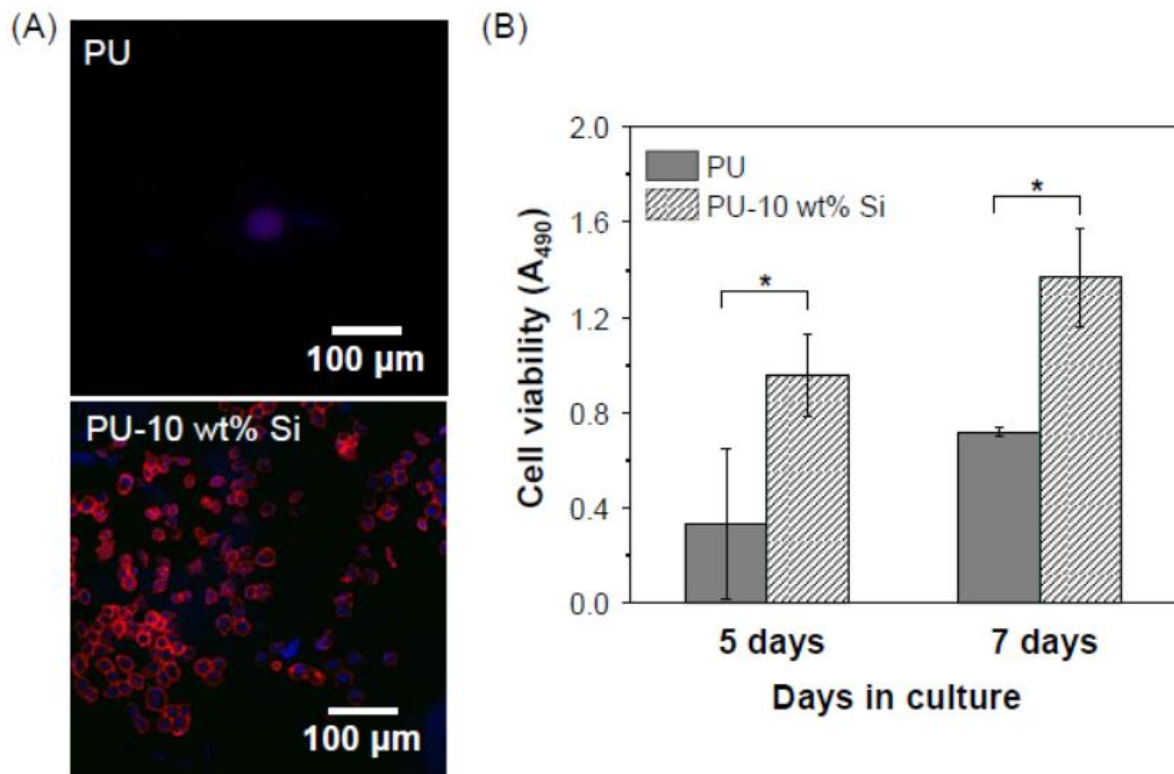


Figure. 2.6. (A) CLSM images of fibroblasts after 1d-cell attachment to the surface of PU, and PU-10 wt% Si membranes, and (B) cell proliferation of fibroblasts after culturing for 5 and 7 days (n=3, *p < 0.05)

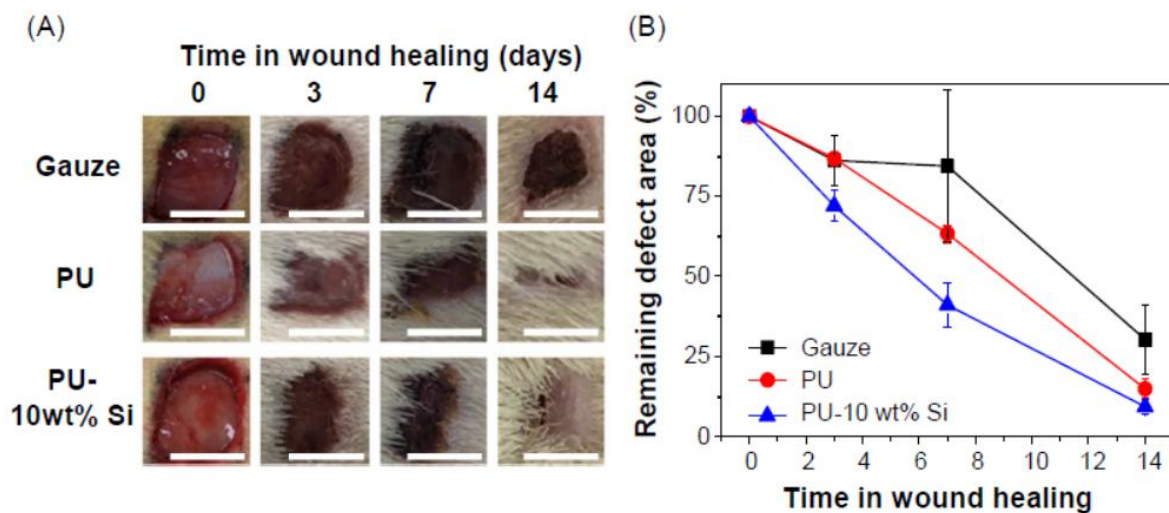


Figure. 2.7. Wound-healing rate of three dressing materials: (A) Macroscopic appearance of incised wounds in three wound dressing materials (gauze, PU and PU-Si) at different time points (scale bar = 10mm) and (B) remaining defect area after 3, 7 and 14 days treatment with gauze, PU and PU-Si membranes (n = 3, *p < 0.05).

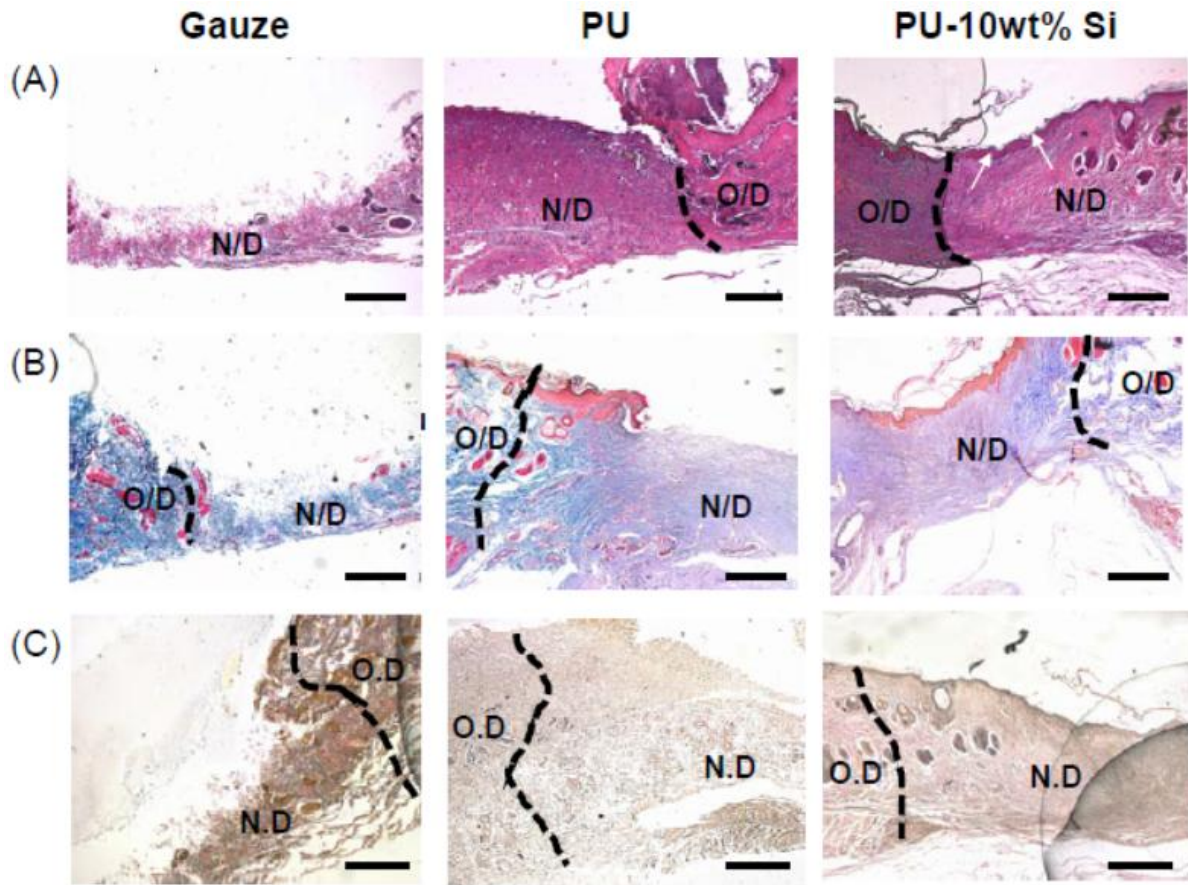


Figure. 2.8. Histological and immunohistochemistry examination of the wound regions treated with gauze, PU, and PU-Si dressings after 14 days: (A) representative H&E staining images of the wound regions, (B) Masson's trichrome (MT) staining images of the collagen matrix in the wound regions and (C) van Gieson staining images of the elastin fibers in the wound regions after the removal of the covered wound dressing. O/D: original dermis, N/D: newly formed dermis

Chapter 3.

**Phosphate conjugated polyurethane with induced mineralized
hydroxyapatite composite for elastic cartilaginous tissue
replacements**

3.1 Promoting the nucleation of hydroxyapatite on glycerol phosphate-conjugated polyurethane for the enhancement of bioactivity

3.1.1 Introduction

Elastomers have been widely adopted in long-term tissue engineering fields, such as breast implants, tissue expander, and cartilage replacements since most of these materials resist degradation in body fluids, maintaining their inherent viscoelastic mechanical properties.[67-69] One of the representative elastomers for biomedical applications is polyurethane (PU), which exhibits rubber-like elasticity and has an inherent porous structure.[70, 71] In addition, the molecular stability of PU is essential to permanent implants for non-regenerative tissues, including breast prosthesis surrounded by soft tissues, and the cartilage or bone of elderly individuals.[72-74] However, the only limitation of PU for use in permanent implants is its low biocompatibility, reflecting its hydrophobic polymer chain.[75] To enhance the biological property of PU, several bioactive coatings were performed using hydrogels or bioceramics.[76, 77]

HA is one of the most qualified biocompatible calcium phosphate minerals, and it has a high affinity with biopolymer and thermodynamic stability in body fluids.[78, 79] Thus, there have been numerous efforts to improve the biological property of polymers using various HA incorporating method, involving solvent-compression method, simple powder mixing, and mineralization.[80-82] Among these techniques, mineralization is favorable to improve coating stability and biological properties since HA nucleation is induced at specific functional groups (hydroxyl, carboxyl, and phosphate groups) with strong binding forces.[83, 84] However, since PU has no specific sites for interactions with hydrophilic coating layers, coating stability had not been achieved without any further processes. Thus, Yuk et al. attempted to generate a robust interface between elastomers and hydrogels through the application of chemical crosslinking processes.[85] Kim et al. provided nucleation sites on substrates for accelerating apatite growth.[86] Chemically bonded amorphous calcium phosphates grew into hydroxyapatite (HA), forming a stable and homogeneous coating layer.

In the present study, glycerol phosphate was introduced as a new conjugate to improve HA coating stability on PU to provide nucleation sites for calcium phosphate ions and accelerate HA mineralization. Glycerol phosphate is a derivative of glycerol, which is a chain extender of PU.[87] Thus, glycerol phosphate, which has a structure similar to that of glycerol, can be easily conjugated with PU through addition without any complex conditions. In addition, the exposed phosphate groups on the polymer chain act as a link between mineralized HA and PU, inducing stable coating systems. The present study addresses an efficient method to fabricate a structurally stable and biologically improved PU-HA composite incorporating glycerol phosphate. Surface morphology, chemical bonding, and crystalline phase were analyzed and the mechanical properties and biological properties were also investigated. Moreover, its potential uses, including cartilage or bone replacements, were introduced.

3.1.2 Experimental procedures

Preparation of PU-gp

Glycerol phosphate solutions were prepared after dissolving glycerol phosphate disodium salt hydrate ($C_3H_7Na_2O_6P \cdot xH_2O$, Sigma Aldrich, USA) in distilled water with a weight ratio of 1:80 and 1:20, respectively. The prepolymer of PU (HYPOL 2002, Dow Chemical Co., Ltd., UK) and glycerol phosphate solutions were mixed at a weight ratio of 1:2 at room temperature to adjust final compositions (weight ratio of PU:gp = 1:0.025 and 1:0.1). In addition, the pure PU was also fabricated as a comparison group through a reaction between distilled water and the prepolymer without glycerol phosphate.

HA mineralization on PU-gp

For accelerating HA mineralization, highly concentrated ionic solutions were prepared after sequentially dissolving sodium chloride (NaCl, Sigma Aldrich, USA), potassium chloride (KCl, Sigma Aldrich, USA), calcium chloride ($CaCl_2$, Sigma Aldrich, USA), magnesium chloride ($MgCl_2$,

Sigma Aldrich, USA), and sodium phosphate monobasic (NaH_2PO_4 , Sigma Aldrich, USA) in water to meet the concentration of 10-fold simulated body fluid (SBF)[88], PU-gp was immersed in solution for 4 and 12 h after adding sodium bicarbonate (NaHCO_3 , Sigma Aldrich, USA) to increase the pH to 6.5 at 37°C.

Characterization of PU, PU-gp and PU-gp-HA

The chemical structure of PU-gp was investigated using 500 MHz solid NMR (Bruker Advance II, USA) equipped with 4 mm MAS BB-1H. The specimens were prepared as fine particles with dimensions of 60-70 mesh and dried in a vacuum chamber. ^{31}P nuclear detecting channel was acquired at 202.46 MHz using exponential multiplication (EM) window functions. After confirmation of PU-gp synthesis, to verify the effects of glycerol phosphate on HA nucleation, surface morphology and crystalline structure of PU-gp-HA with different amounts of glycerol phosphate were detected using a field-emission scanning electron microscopy (FE-SEM, SUPRA 55 VP, Carl Zeiss, Germany) and X-ray diffraction with Cu sources (XRD, D8-advance, Bruker Co., Germany) at a scanning rate of 2°/min from 20° to 60°, respectively.

Mechanical properties of PU, PU-gp and PU-gp-HA

The mechanical properties of PU, PU-gp (weight ratio of PU:gp was 2.5 wt% and 10 wt% each) and PU-gp-HA (precipitation time was 12 h) were measured using Instron in tensile mode (Model 5565, Instron corp., Danvers, MA). The specimens were prepared as a rectangular shape with a dimension of 4 mm×5 mm×50 mm. The experiments were performed with a constant strain rate of 1 mm/min. Ultimate tensile strength (UTS), elongation at break, and stiffness of each group were determined from the stress-strain curves.

Stability test of PU-gp-HA

To demonstrate the effect of glycerol phosphate on the stability of HA, PU-HA (control) and PU-gp-HA were immersed in water and sonication was performed for 30 min. Specimens with and

without sonication were combusted under N₂ conditions up to 600 °C with a heating rate of 5 °C/min. The ratio of the remaining HA in PU-HA and PU-gp-HA was calculated using following the equation:

$$W_{HA,r}(\%) = W_{HA}/W_{comp} \times 100$$

, where $W_{HA,r}$: Weight ratio of HA in PU-HA and PU-gp-HA, W_{HA} : weights of HA after combustion, W_{comp} : initial weights of PU-gp and PU-gp-HA. Moreover, the surface morphology of PU-HA and PU-gp-HA after sonication was observed using SEM to determine the degree of HA detachments.

Biological properties of PU, PU-gp, and PU-gp-HA

The biological properties of PU, PU-gp, and PU-gp-HA were analyzed using a pre-osteoblast cell line (MC3T3-E1, ATCC, CRL-2593) and a fibroblast cell line (L929, derivative of strain L, *Mus musculus*, mouse). Prior to the cell tests, the specimens were washed with sterilized distilled water for 3 days in a clean bench. Pre-osteoblasts and fibroblasts were seeded onto each sample at a density of 2×10^4 and 5×10^4 cells/ml, respectively, for the attachment test. The cells were cultured in an alpha-minimum essential medium (α -MEM, Welgene, Korea) containing fetal bovine serum (FBS, 5% for pre-osteoblasts and 10% for fibroblasts) and 1% penicillin-streptomycin and incubated for 1 day under air conditions containing 5% CO₂ at 37 °C. After a day of culturing, the cells were fixed using 2.5% glutaraldehyde after rinsing with phosphate-buffered saline (PBS). Subsequently, the cells were sequentially dehydrated using 75%, 95%, and 100% ethanol. Finally, the cells were treated with 1, 1, 1, 3, 3, 3, hexamethyldisilazane for 10 min and dried in a fume hood. The post-treated specimens were observed using SEM. Cell viability was also verified by MTS assay (CellTiter 96 Aqueous One Solution; Promega, USA) using pre-osteoblasts and fibroblasts. After 3 and 5 days of culturing, post treatment was conducted after the following steps. The specimens were washed with PBS, transferred to new 24-well tissue culture plates, immersed in alpha-minimum essential medium with tetrazolium compound dye and incubated at 37 °C for 2 h. The quantity of formazan product as a result of mitochondrial activity in live cells was measured as the absorbance at 492 nm using a microreader (Model 550; Bio-Rad, USA).

Statistical analysis

All experimental data were expressed as the means \pm standard deviation (SD), using 3 specimens for each group (n=3). The statistical analysis was performed using one-way analysis of variance (ANOVA). A p-value of <0.05 was considered statistically significant (* $p < 0.05$, ** $p < 0.01$).

3.1.3 Results and discussion

Fabrication of PU-gp-HA

PU-gp-HA was synthesized through 2 steps, PU modification and HA mineralization, as schematically represented (**Figure 3.1.1(A)**). First, glycerol phosphate was conjugated to the PU chain during polymerization. Isocyanates in PU prepolymer reacted with hydroxyl groups of water (H-OH), forming a urea linkage, which is the main bonding of the polymer chain. Phosphate functional groups were also exposed on the surface of the polymer chains as a result of another reaction between the isocyanates and hydroxyl groups (R-OH) of glycerol phosphate. Through the competitive reaction between two hydroxyl groups, PU-gp was successfully fabricated and characterized using ^{31}P -NMR (**Figure 3.1.1(B)**). The peak was shifted from the zero point of standard phosphoric acid to 6.68 ppm, indicating the phosphate monoester (R-O-PO(OH)₂) of glycerol phosphates, while no peaks were detected in pure PU since this compound has no P source or linkage.[89]

Second, PU-gp-HA was fabricated through treatment in concentrated SBF solutions for 4 and 12 h. During precipitation, amorphous CaP nanoparticles reversibly formed in the solution. The phosphate groups in PU-gp provided nucleation sites for reversibly existing CaP nanoparticles and calcium and phosphorous ions. The nanoparticles were anchored onto nucleation sites and grown into microspheres with a diameter of 1 μm , which were homogeneously distributed during the 4 h treatment. After 12 h, spherical CaP particles were fully deposited onto the substrate, forming flat HA crystal films (**Figure 3.1.1(C)**).

XRD analysis was performed according to the precipitation time (4 and 12 h) and the amounts of glycerol phosphate (0 wt%, 2.5 wt% and 10 wt% to polymer) (**Figure 3.1.2**). Since pure

PU had no nucleation sites that gathered CaP nanoparticles, no specific peaks were detected after the 4 h precipitation. After 12 h, HA peaks were observed on pure PU, resulting from physically stacked HA sediments. However, as the amounts of glycerol phosphate increased, PU-gp accelerated CaP nucleation and HA crystal growth, which is thermodynamically more stable at the given pH and ion concentration than CaP.[88] Broad HA peaks were only observed for the 4 h treated PU-gp, reflecting the fast nucleation and crystallization process. After 12 h, highly crystalline HA was clearly obtained, showing a high and narrow peak.

Mechanically reinforcing effects of HA

The mechanical properties of PU, PU-gp, and PU-gp-HA were investigated to understand the effect of conjugated glycerol phosphates and HA on the mechanical properties of PU. A representative stress-strain curve was obtained from the tensile test (**Figure 3.1.3**). Failure occurred in the elastic deformation region for all groups. Ultimate tensile strength (UTS), elongation at break, and stiffness were summarized in **Table 3** to determine the glycerol phosphate effects on the mechanical properties of PU. Pure PU showed a highly elastic performance, deforming $100.82 \pm 8.98\%$. However, as the concentration of glycerol phosphate increased, the overall mechanical properties declined. A 2.5 wt% of glycerol phosphate did not deteriorate the innate property of pure PU, whereas a 10 wt% of glycerol phosphate negatively influenced the mechanical properties of PU. UTS decreased to 0.41 ± 0.04 MPa, and the elongation at break simultaneously decreased to $68.62 \pm 1.66\%$ in PU-10 wt% gp. The competitive reaction of water and glycerol phosphates primarily contributed to the attenuated mechanical properties. Too much glycerol phosphate hindered chain propagation compared with pure PU, leading to short polymer chain, and the final product lost its elastic property similar to PU-10 wt% gp, although 2.5 wt% conjugation did not unfavorably affect PU. However, incorporating the HA layer enhanced the strength of PU-gp. The stiffness of PU-2.5 wt% gp significantly increased from 0.69 ± 0.04 MPa (PU-2.5 wt% gp) to 0.80 ± 0.02 MPa (PU-2.5 wt% gp-HA), an even higher value than that of pure PU (0.69 ± 0.05 MPa), demonstrating that the sturdy HA layer partially dissipates the deformation energy. It has been suggested that the robust interface between elastomers and

bioceramics induced higher stiffness and strength. Thus, these materials were not just physically stacked, but electrically interacted with the phosphate groups of PU-gp. In addition, even in PU-10 wt% gp, the HA layer compensated the weakened strength and stiffness comparable to values of pure PU. In summary, 2.5 wt% of glycerol phosphate was optimum for improving mechanical properties without any undesirable effects.

HA coating stability

The coating technique is one of the most widely used methods to integrate two or more compounds for improvements in the biological properties of substrates.[90] However, fabricating a durable and long lasting coating layer is essential and also difficult, particularly in biomedical applications, reflecting frequent deformation under physiological conditions.[91] Thus, additional treatments, such as conjugating another biocompatible agent in the original polymer framework, have been adopted for high affinity with other bio-layers.[92] In effect, glycerol phosphate successfully enhanced coating stability, even in severe environments. To demonstrate the coating stability, the durability was assessed when exterior impacts were applied to PU-gp-HA and PU-HA. The initial amounts of HA were significantly different according to the existence of glycerol phosphate ($8.22 \pm 2.28\%$ of HA in PU-HA and $14.73 \pm 1.94\%$ of HA in PU-gp-HA) (**Figure 3.1.4(A)**). After sonication test, little HA debris was detected on the PU-HA surface, where 80% of HA was detached because the turbulence of sonication was sufficient to delaminate physically deposited HA from PU (**Figure 3.1.4(B)**). However, most HA ($12.13 \pm 0.02\%$ of HA) remained in PU-gp-HA, as the sonication energy was insufficient to disrupt the robust interface between PU-gp and HA. Thus, the coating stability and durability of this compound is advantageous for bio-implants, which should bear frequent movement or impacts, such as meniscal replacements.[93]

***In vitro* biological properties of PU, PU-gp, and PU-gp-HA**

To demonstrate the potential uses in tissue engineering applications, the *in vitro* biological property of PU, PU-gp, and PU-gp-HA were evaluated using L929 fibroblasts (**Figure 3.1.5(A-C)**)

and MC3T3-E1 pre-osteoblasts (**Figure 3.1.5(D-F)**). On pure PU, the cells were not spread and showed a spherical shape, reflecting the bioinert nature of PU (**Figure 3.1.5(A, D)**). However, the cells stretched their filopodia, forming focal adhesions with the phosphate groups in PU-gp (**Figure 3.1.5(B, E)**) and bioactive HA of PU-gp-HA (**Figure 3.1.5(C, F)**). The degree of proliferation was also indicated using an MTS assay in **Figure 3.1.5(G, H)**. On day 3, cell viability was not significantly different in all samples because the stage of proliferation was too early to show a clear difference in the number of viable cells. The cells on PU-gp-HA were significantly higher than those on PU-gp at day 5, suggesting that glycerol phosphate made hydrophilic and biocompatible surface for cells to attach with elongated or stellate shapes but was not bioactive to promote cell proliferation. However, HA not only provided suitable surfaces for cell adhesion but also remarkably enhanced cell viability. Thus, PU-gp-HA is promising for use in diverse tissue engineering applications, including both soft tissue and hard tissue from in vitro cell test.

3.1.4 Conclusion

The results of the present study demonstrated that elastomer modifying techniques using glycerol phosphate can induce homogeneous HA precipitation, enhance adhesion stability between PU and HA, and improve the inherent biological properties of PU. During precipitation, CaP nanoparticles were spontaneously gathered to phosphate functional groups, acting as nucleation sites for HA. Rapid HA formation and robust interface reinforced the mechanical properties of PU. The coating stability was also improved through interactions between covalently bonded functional groups and HA. Furthermore, outstanding in vitro biocompatibility indicated a great potential for use in tissue engineering applications, including auricular cartilage replacement and bone regeneration scaffolds.

Figures

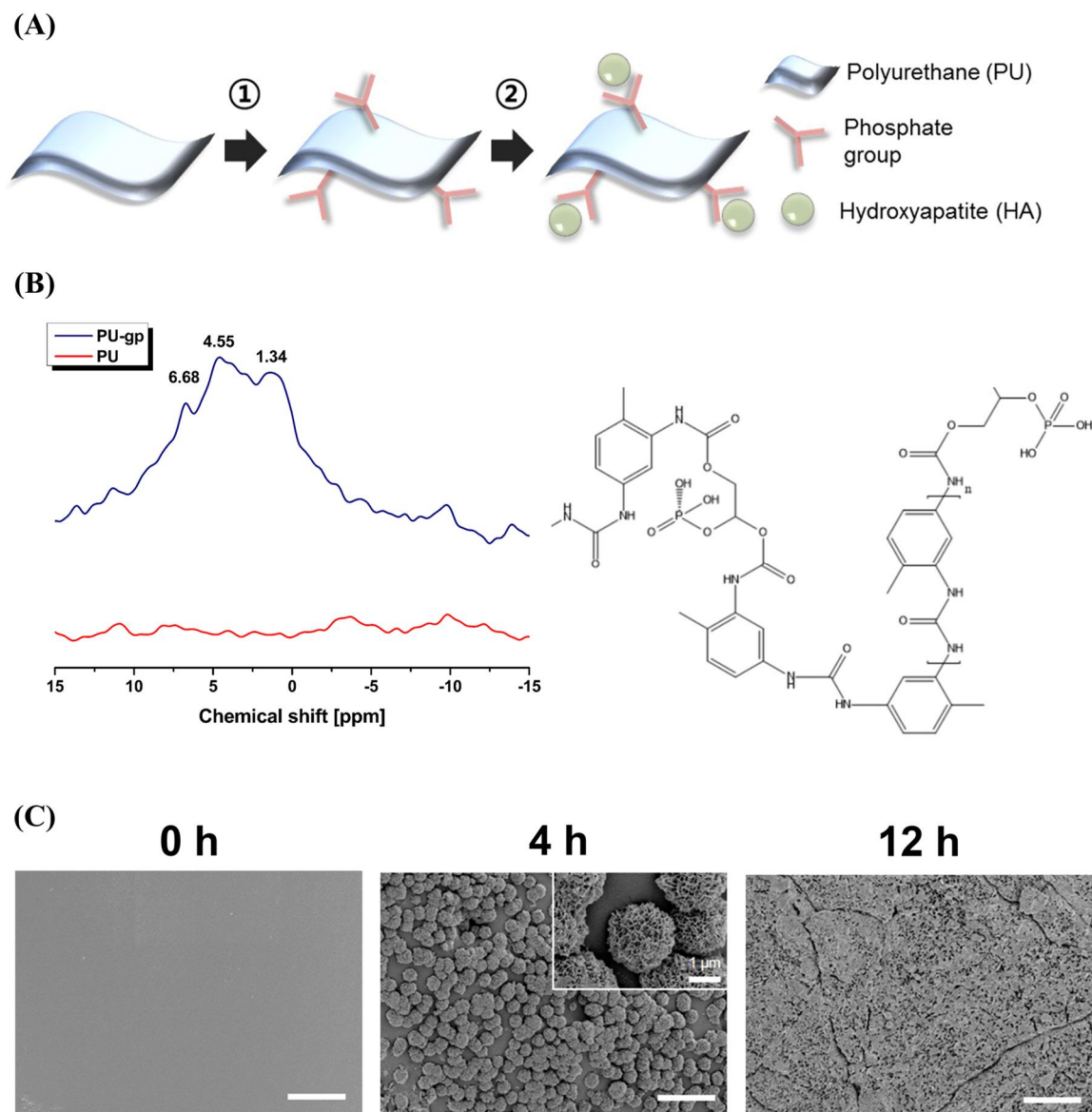


Figure 3.1.1. (A) Schemes of (1) PU-gp and (2) PU-gp-HA formation; (B) solid state P-NMR results according to existence of glycerol phosphate with chemical structure of designed PU-gp-HA and (C) SEM images of surfaces of PU-gp-HA at different precipitation time (0 , 4, and 12 h) (scale bar = 10 μ m)

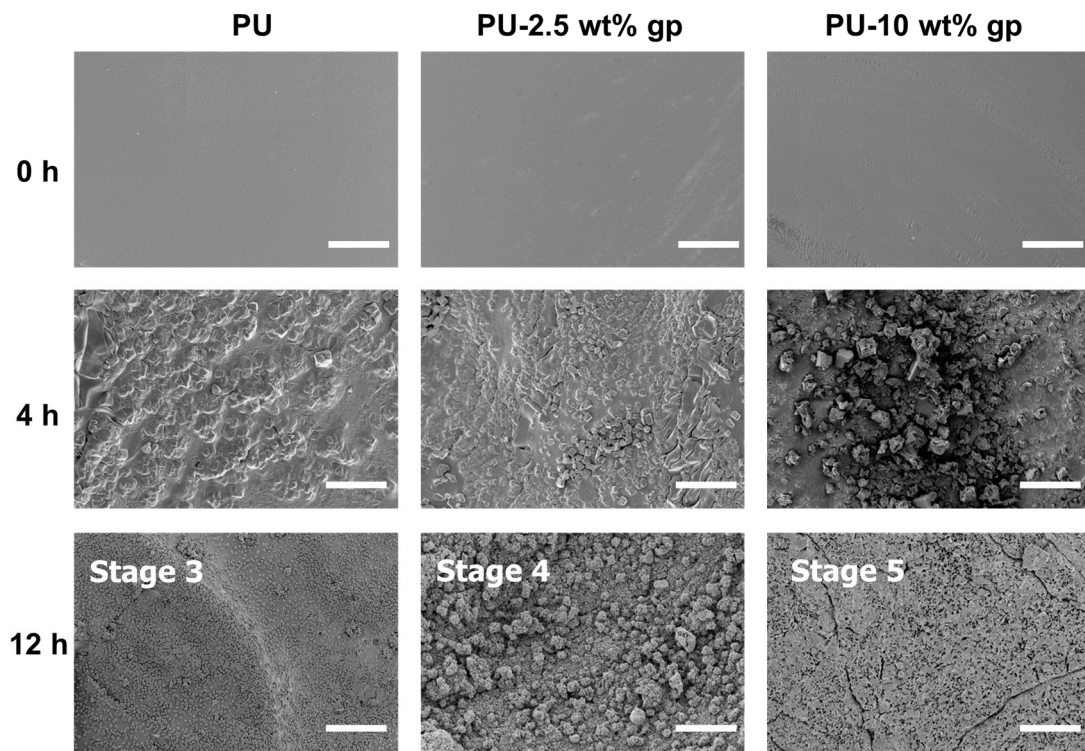


Figure 3.1.2. HA morphology images at different mineralization stage according to the glycerol phosphate composition and mineralization time (scale bar : 20 μ m)

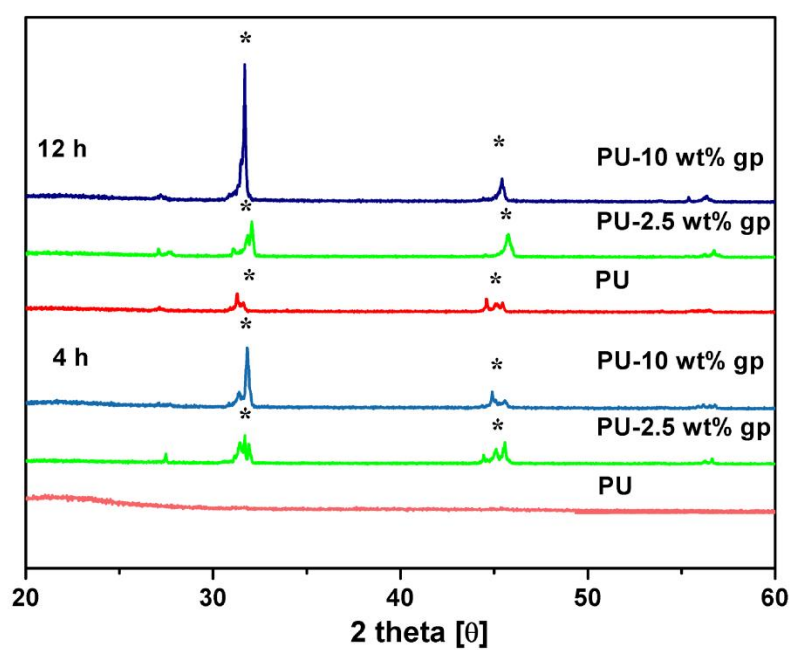


Figure 3.1.3. XRD peaks of PU-gp-HA (4 and 12 h treated specimens). The asterisk indicates the characteristic peaks of hydroxyapatite.

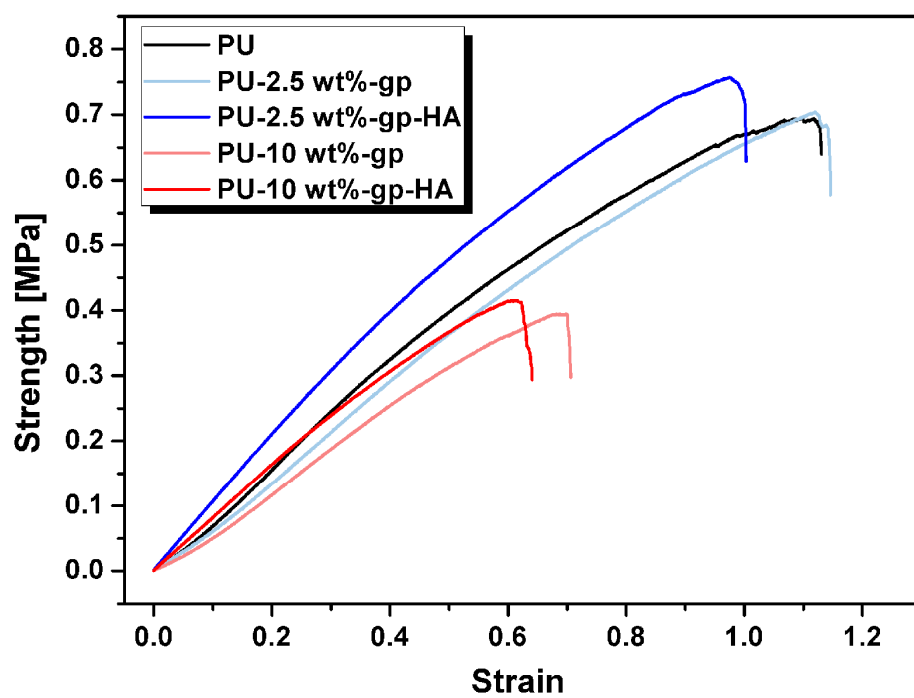
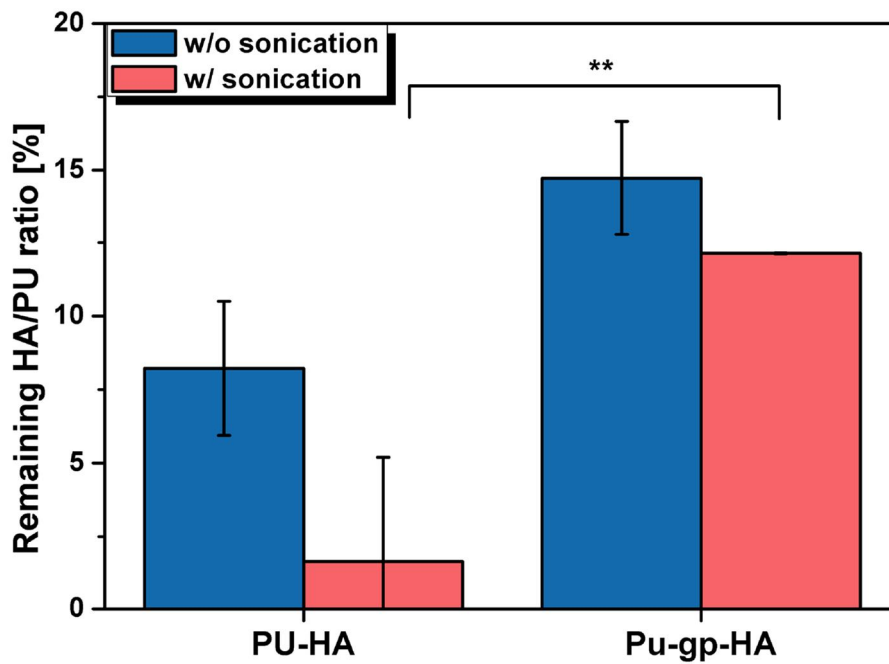


Figure 3.1.4. Stress-strain curve of PU, PU-x wt% gp, and PU-x wt% gp-HA (x=2.5 and 10) (n=3).

(A)



(B)

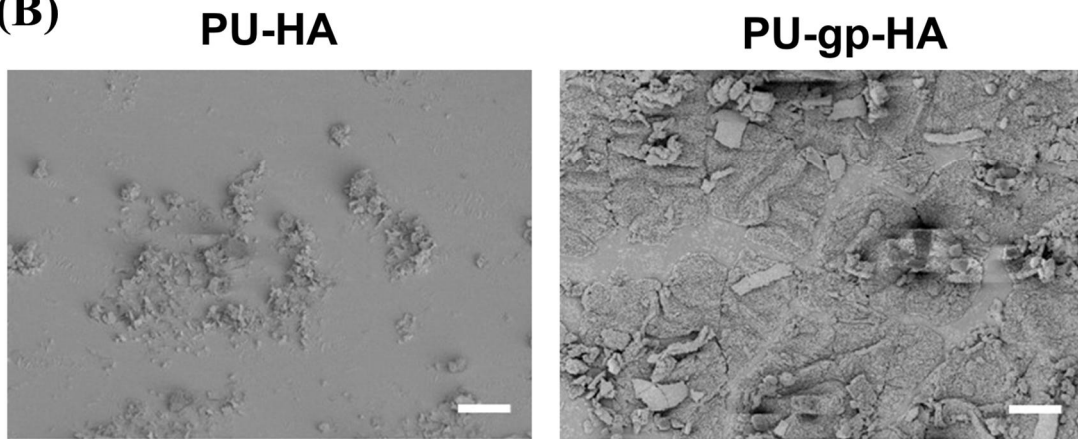


Figure 3.1.5. (A) Remaining HA amount of PU-HA and PU-gp-HA before and after sonication for 30 min, calculated based on TGA results. Surface morphology of (B) PU-HA and PU-gp-HA after sonication. The asterisk indicates statistically significant p-values of ** $p < 0.01$ with $n=3$ (scale bar = 10 μm)

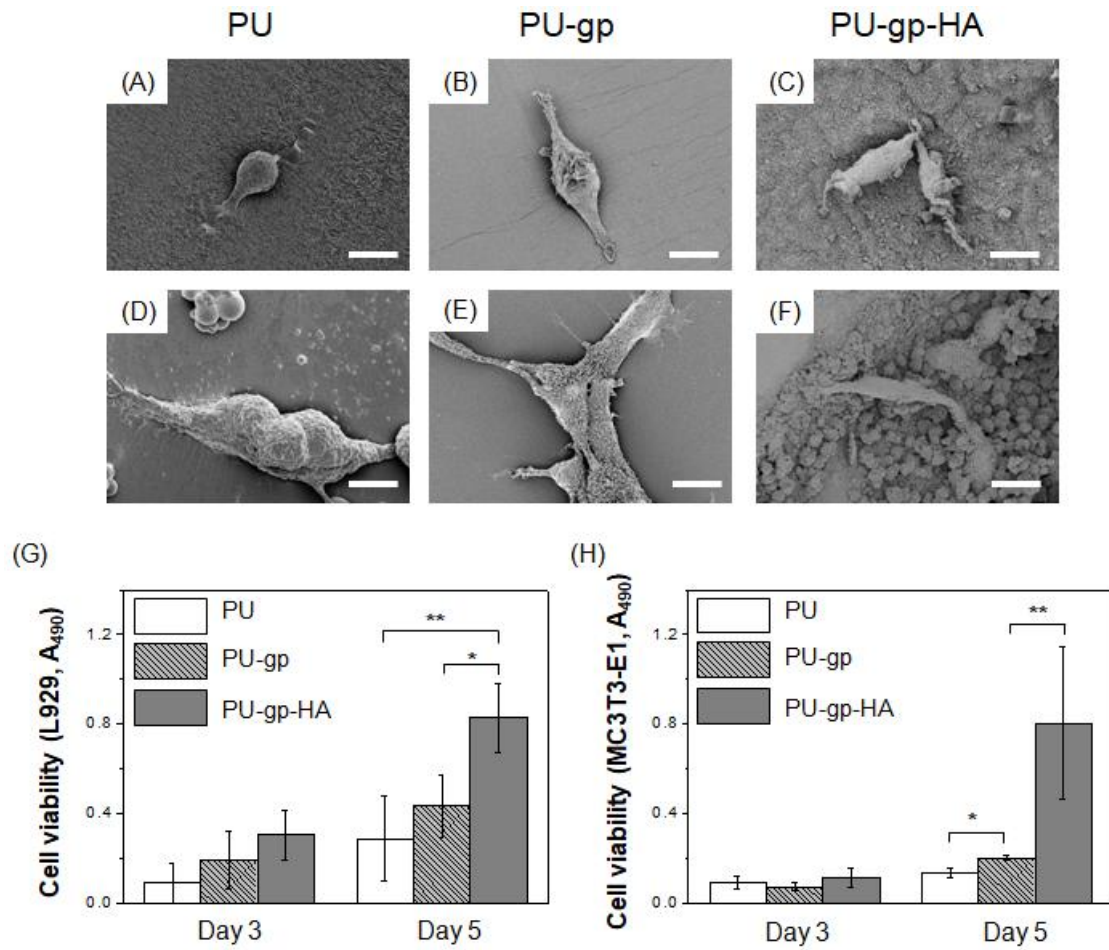


Figure 3.1.6. In vitro fibroblasts (A, B, and C) and osteoblasts (D, E, and F) attachment cultured for 1 day (scale bar = 10 μm) and MTS analysis for 3 and 5 days (G and H). The asterisk indicates statistically significant p-values of * p<0.05 and ** p<0.01 with n=3 (scale :10 μm)

3.2 Densified polyurethane/hydroxyapatite composite for cartilaginous applications

3.2.1 Introduction

Though the natural elastomeric property of polyurethane is highly beneficial to be used for cartilage scaffold, it has limitation as a permanent implant due to its low biological property. However, from PU-gp-HA system developed in our previous research, biological property was significantly improved for representative mammalian cells [94]. Thus, adopting our system to a cartilage replacement, it is expected to be impressive, representatively including both artificial auricles and menisci replacement.

Ears could be injured or born congenitally malformed, but is impossible to be reconstructed naturally without any supports [95]. The most well established surgical method to reconstruct the ear is harvesting and shaping the autogenous rib cartilage [96]. However the conventional method is not unsatisfactory due to its difficulty in shaping process particularly for unskilled physicians. Thus, prosthesis was highly attractive to reconstruct the auricles, implanting the biomaterials shaped like ear beneath the facial skin. Medpor®, which is made of high density polyethylene (HDPE), is the most widely used prosthesis clinically in ear reconstruction market [97]. It is easily shaped with carving and biologically stable. However, its brittleness induced breakdown during the lift-up surgery, resulting in severe failure. Recently, elastomeric polymer, silicon rubber or polyurethane showed potential for the cartilage replacement from this reason.

Foreign body reaction is another issue in auricular replacement applications [98]. Polymeric implants used beneath the soft tissue cannot avoid the capsule formation as a foreign body reaction [99]. If the cellularity is too vigorous, following the inflammation cascade negatively, capsular contracture could occur [100]. To prevent capsular formation, improving hydrophilicity of the implants or incorporating biocompatible materials are widely used [101]. Since PU-gp-HA system overcomes the bio-inert property of natural polyurethane and maintains composite system stably even

under deformation, it is very attractive to be used for auricular replacement.

PU-gp-HA system also could be utilized in meniscal replacement applications. The menisci of the knee are semilunar-shaped pieces of fibrocartilaginous tissue located in the knee joints. They provide structural integrity to the tibia and femur, absorb shock, disperse the weight of the body, and act as a lubricant during movement [102-104]. Unfortunately, meniscus injury is one of the most common knee problems as the structure is aged by daily life [105, 106]. Meniscectomy, the removal of all or part of the torn meniscus, is the most widely used technique to relieve the knee pain associated with severe degeneracy of a meniscus [107-109]. However, the structural deformation of the meniscus after meniscectomy can result in secondary impairment due to the uneven load distribution across the knee [110-112]. In severe cases, repetitive knee problems can result in chronic osteoarthritis [113, 114]. Thus, the use of an artificial replacement is an alternative method to treat a non-regenerative meniscus that offers a stable substitute for the mechanical function of the original meniscus [115-118].

The hierarchical structure of a meniscus, characterized by different moduli in each layer, was observed in a T2-weighted magnetic resonance imaging (MRI) image of bovine medial femoral condyle tissue, known as a natural chondrogenic extracellular matrix (ECM) [119]. Because the geometry of a natural meniscus is complex, a biomimetic design is necessary to fabricate a more desirable scaffold that exhibits the natural anisotropy of this structure. Various products have been commercially produced in the market. For example, Actifit® (Orteq, UK) is a meniscus substitute that can endure various biomechanical deformations [120]. It is composed of two materials, polyurethane (PU) and polycaprolactone (PCL), to mimic the natural properties of a meniscus. The rigid PU provides mechanical stability to the scaffolds to withstand external forces, whereas the soft PCL provides not only elasticity to absorb impact but also an adequate environment into which neighboring tissues can migrate upon degradation. Other groups have fabricated anisotropic scaffolds for menisci using aligned electrospun PCL fibers, mimicking the collagen fibers of a natural meniscus [121]. The one-directionally aligned fibers exhibited anisotropic mechanical properties according to the force applied; however, the modulus of electrospun fibers is not expected to reach the level of that

of natural menisci.

In addition, an ideal meniscus construct requires sufficient bioactivity as well as biomechanical properties. ECM components including collagen, hyaluronic acid, various synthetic polymers, and hydrogels are widely used in clinical applications of artificial menisci [122-127]. One representative commercial product is CMI[®], which is composed of collagen type I, the major constituent of natural menisci [128]. This product was considered safe for use as an artificial meniscus without any adverse effects or toxicity effects for neighboring tissues [129]. However, the size of the collagen scaffolds shrank after their implantation, and they lost their original semilunar shape too early during the follow-up [130]. Other synthetic scaffolds composed of elastomeric polymers, especially PU, were introduced to overcome the weakness of collagen scaffolds [131-133]. Their porous structures were beneficial for tissue ingrowth, and their structural stability provided safety for long-term implants [133]. However, existing commercial products cannot replicate the anisotropic mechanical properties of natural menisci, which is a crucial factor to achieve the desired load-bearing performance.

In this research, glycerol phosphate (gp)-conjugated PU with mineralized HA, abbreviated PUH, was used for auricular prosthesis and the multilayered scaffold that could achieve both anisotropic mechanical property and suitable biocompatibility for meniscus replacement [94]. The use of PUH was expected to enable the original elastomeric properties of PU to be maintained with improvement of the biological properties compared with those of pure PU because of the adoption of the HA precipitation method. In this system, PUH was densified using different pressures to produce different density to focus on the fabrication of elastic microtia and anisotropic scaffolds that mimic natural menisci, and their structure and porosity were characterized using scanning electron microscopy (SEM) and microcomputed tomography (μ -CT). The mechanical properties (tensile strength and stiffness) of the densified PUH structures were also analyzed. Its biological property was further discussed by in vivo capsular formation test, analyzing the capsule thickness and collagen density. Auricular replacements were successfully fabricated by metal mold designed by ear STL files. In addition, biomimetic multi-layered PUH was prepared for menisci substitutes. The structural

stability at the interface between dense and porous layers was also determined using tensile tests. Finally, the anisotropic mechanical properties of the multilayered PUH, which consisted of alternate stacking of densified PUH and porous PU, was investigated using tensile and compression tests along different directions.

3.2.2 Experimental procedures

Densification of PUH and fabrication of auricles and multilayered scaffold

Porous PUH was prepared following the procedure used in our previous study [94]. Briefly, gp was conjugated to PU during a foaming process by simply mixing it with a PU prepolymer (HYPOL 2002; Dow Chemical Co., Ltd., U.K.), and then, HA was precipitated on the surface using a mineralization process. The PUH samples were then compressed by applying various pressures (5, 1000, and 2000 kgf) at 140°C using a hand press. Pure PU was prepared as a foam phase as a comparison group.

3D metal mold was prepared by metal 3d printing technique with proper STL model for ear. PUH foam was inserted inside mold while heat and pressure was sufficiently applied in compression. Then, further shaping was performed, carving the contour of the ear more accurately.

Densified PUH with 10% porosity was used for the top and bottom layer of the multilayered scaffold. The PU prepolymer was poured on the bottom densified PUH layer, and distilled water was added to produce a foaming reaction (weight ratio of PU:water=1:2). The top dense layer was carefully placed on the porous PU layer at the end of the reaction. The amount of PU prepolymer was predetermined to achieve a final height ratio of dense/porous/dense layers of 1:1:1.

Porosity evaluation

The structures of the porous and densified PUH were investigated using μ -CT (Skyscan 1173, Belgium) with the following parameters: 1.0-mm Al filter, 180° rotation, 4-frames averaging, 0.4° rotation step, 40-kV voltage, and 200- μ A current. Images were reconstructed and visualized using the

commercial software NRecon (Bruker microCT, Belgium) and CTVOX (Bruker microCT, Belgium), respectively. The porosities of the samples were determined using the following equation:

$$\text{Porosity (\%)} = (1 - V_p/V_r) \times 100,$$

where V_p is the theoretical volume of PU without any pores, which was determined from the ratio of the mass and density (m/ρ , with $\rho = 1.2 \text{ g/ml}$), and V_r is the real volume of PU.

Characterization

The chemical structures of the porous and densified PUH were evaluated using Fourier-transform infrared (FT-IR) spectroscopy (Nicolet 6700, Thermo Scientific, USA) in the wavenumber range of $450\text{--}4000 \text{ cm}^{-1}$ with an average of 64 scans to verify whether denaturation of polymer occurred during the densification process. The outer surface and cross-sectional morphologies of the densified PUH were examined using energy-dispersive X-ray spectroscopy (EDS) coupled with field-emission scanning electron microscopy (FE-SEM; MERLIN Compact, ZEISS, Germany). The HA distribution was also investigated using EDS mapping.

Mechanical properties

Tensile tests were conducted to analyze the mechanical properties of the porous and densified PUH (90% (foam phase, control), 30%, 10%, and 7% porosity) using a universal testing machine (Model 5565, Instron Corp., Danver, MA) in constant-strain-rate mode (5 mm/min). Porous and densified PU without HA (90%, 30%, 10%, and 7% porosity) were also prepared under the same conditions as a comparison group. All the specimens were prepared into rectangular shapes with dimensions of $2 \text{ mm} \times 5 \text{ mm} \times 25 \text{ mm}$.

After evaluating the densified PUH with different porosities, multilayered PUH was prepared. First, the interface stability between the porous PU and densified PUH layers of the multilayered scaffold was evaluated using tensile tests in constant-strain-rate mode (1 mm/min). The specimens were prepared into rectangular shapes with dimensions of $5 \text{ mm} \times 10 \text{ mm} \times 10 \text{ mm}$. A stress–strain curve of the multilayered structure was obtained and compared with that of porous PUH. Then, two

types of mechanical tests were performed to investigate the anisotropic mechanical properties of the multilayered structure. First, disk-shaped specimens were prepared (diameter: 25 mm, height: 12 mm) for compression tests. The experiments were conducted under a constant strain rate of 1 mm/min. Second, the multilayered scaffold was processed into a rectangular shape with dimensions of 5 mm × 10 mm × 25 mm for constant-strain-rate (5 mm/min) tensile testing. The stiffness was analyzed based on the stress–strain curves.

***In vivo* capsular contracture test**

The *in vivo* experiments with dense PU and PUH were performed using dorsal implantation rodent model with 6-week-old male Sprague-Dawley rats for the validation of capsule formation and quality analysis. All animals were pathogen free and were maintained using the same diet and environmental conditions. After a weeklong adaptation period, the healthy animals were selected for use in the experiments. After the anesthesia and hair removal, two incisions were made symmetrically on the dorsum of the rat. PU and PUH were implanted inside the dorsum of the rat through the incised part. At days 14 and 42 after surgery, the animals were sacrificed using CO₂ asphyxiation in accordance with the American Veterinary Medical Association Guidelines for the Euthanasia of animals, and the tissues around the implants were subsequently harvested.

PUH auricular prosthesis was successfully fabricated by using 3d metal mold which was prepared to have a complex ear shape through STL designs. After printing the artificial ear, further carving was performed for a delicate structure. Then, it was inserted beneath a dorsum of nude mice (balb/c, 6 week old, male) after an excision. Pump line was additionally inserted to apply negative pressure for skins to be attached to the prosthesis tightly.

Histological analysis Rats were sacrificed after 14 and 42 days post surgery. The tissues from the implanted area including the surrounding normal skin tissue were harvested *en bloc*, sectioned and fixed in 10 % formalin overnight, and stored in 70 % alcohol at 4 °C prior to being embedded in paraffin. After being washed carefully, the stored tissues were embedded in paraffin and sectioned into slices perpendicular to the capsule. The tissue slices were stained according to three

protocols; hematoxylin and eosin (H&E). The optical images of each stained histological section were analyzed for three parameters: 1) capsule thickness; 2) collagen density of the capsule and 3) the number of inflammatory cells.

Statistical analysis

All the experimental data in this research are expressed as mean \pm standard deviation (SD) ($n = 3$). The statistical analysis was conducted using one-way analysis of variance (ANOVA). A p -value of <0.05 was considered statistically significant ($*p < 0.05$, $**p < 0.01$).

3.2.3 Results and discussion

Porosity control of densified PUH

The PUH composite foam was prepared using the optimized conditions determined in our previous study [94]. It had an open porous structure with approximately 90% porosity resulting from CO₂ gas generation during the PU polymerization. Despite the structural advantages of this porous structure for tissue engineering fields, the mechanical properties were not adequate for load-bearing applications, especially for meniscus replacements. Thus, the porosity of PUH was controlled by densification. With increasing compressive force, the porosity dramatically decreased from 90% to 30%, 10%, and 7%. Each group was named after its porosity: PUH 30, PUH 10, and PUH 7, respectively. The 3D frameworks of the structures are visible in the μ -CT images in **Figure 3.2.1(A)**. The large and spherical pores from the foam states shrunk (the average pore size decreased from 250–300 μm to approximately 10–20 μm). In addition, the specimens became homogeneously dense without any defects, as observed in the cross-sectional μ -CT images of the xy, yz, and zx planes in **Figure 3.2.1(B)**.

Characterization after densification process

The chemical structures of the densified and porous PUH were examined using FT-IR

analysis to determine whether structural decomposition occurred during the densification process; the results are presented in **Figure 3.2.2**. Representative peaks for PU were detected at 700–1200, 1600, and 2700 cm^{-1} , which were attributed to C–O stretching, the effects of urethane linkage (NHCO), and C–H stretching in both the porous and densified PUH [134]. In addition, characteristic peaks from P–O bonding were detected at 650 cm^{-1} , which provides evidence of the phosphorous groups of both gp and mineralized HA [135]. The identical peaks of the porous and densified PUH indicate that no chemical irritation occurred during the densification process.

The microstructures of the porous and densified PUH were compared using SEM. The porous PUH foam had a highly open porous structure, as depicted in **Figure 3.2.3(A)**. After densification, the microstructure of PUH changed significantly. Few pores remained on the top surface of the densified sample (**Figure 3.2.3(B)**), whereas some small pores with sizes of approximately $100\text{ }\mu\text{m}$ were formed, as observed in the cross-sectional images (**Figure 3.2.3(C)**). Microsized HA particles were also observed in the higher-magnification cross-sectional image (**Figure 3.2.3(D)**). The HA layers on the pore walls of the porous PUH became microfillers of the densified PUH as the pores shrunk. The HA distribution is clearly observed in the EDS mapping images. Ca and P were detected all over the polymer surface, indicating that HA was uniformly distributed in the PUH. Small amounts of other elements, including Mg, Na, and Cl, were also detected; these elements originated from the mineralized HA salts in the concentrated simulated body fluid solution.

Mechanical properties of densified PUH

Tensile tests of the PUH (30%, 10%, and 7% porosity) and densified PU (10% porosity) were performed within the elastic deformation region, and the results are presented in **Figure 3.2.4(A)**. Two factors affected the mechanical properties of the densified PUH: the overall porosity and HA distribution. With decreasing porosity, the tensile strength and modulus significantly increased. The modulus and ultimate tensile strength increased from $39.7 \pm 7.11\text{ MPa}$ and $61.7 \pm 0.32\text{ MPa}$, respectively, for PUH 10 to $59.4 \pm 5.98\text{ MPa}$ and $95.9 \pm 4.44\text{ MPa}$, respectively, for PUH 30. PUH 10

and PUH 7 had similar mechanical properties because the porosity was gradually saturated over 1000-kgf compressive pressure.

In addition, the mechanical properties of the densified PU and PUH at the same porosity clearly differed. The mineralized HA layers reinforced the stiffness and strength of the porous PU because of the effects of the gp on HA at the molecular level, as demonstrated in our previous study [94]. The stiffness slightly increased from 0.60 MPa for porous PUH to 0.80 MPa for porous PU because the porosity of PUH did not change after the HA mineralization process [94]. However, the mechanical properties of the densified PUH were highly enhanced as HA was incorporated, as depicted in **Figure 3.2.4(B)** and **3.2.4(C)**. The UTS of the densified PUH 10 increased from 40 to 60 MPa and its stiffness increased from 45 to 90 MPa as HA was incorporated. These results can be explained by the following factors: 1) the HA acted as microfillers in the PU matrix, 2) the grafted phosphate groups played an important role in providing interfacial stability between PU and HA, and 3) the volume ratio of HA increased. First, the HA coating layers on the pores became rod-shaped ceramic fillers as compressive stress was applied, resulting in a fiber-reinforced polymer (FRP) structure, which is considered the most common and efficient way to enhance the mechanical properties of polymers [136]. In particular, polymer/ceramic composite systems are one of the preferred systems to reinforce the mechanical properties of polymer matrices [137, 138]. The tensile modulus and tensile strength of composites are significantly and simultaneously reinforced without any damage to the ductility with the incorporation of ceramic nanoparticles, nanotubes, or microfibers into polymers [32, 139, 140]. For instance, when PU foam was reinforced by 10 wt% of silica (SiO_2) powders, the tensile modulus and strength slightly increased from 310 to 380 MPa and 9.2 to 10.7 MPa, respectively [141]. Our densified PUH system, which contained approximately 15 wt% HA exhibited much higher reinforcement of the mechanical properties, including a 2-fold increase in the modulus and 1.5-fold increase in the strength compared with only densified PU because gp acts as a coupling agent between PU and HA [94]. Second, the HA produced in our system (providing active nucleation sites for HA mineralization) was strongly bonded to the phosphate-grafted PU, maintaining a robust interface between the HA layers and PU substrates. The high affinity between these two

layers prevented the HA fillers from acting as defects that would deteriorate the mechanical properties and structural stability. Finally, the volume ratio of HA in the overall scaffolds increased by approximately 5 times as the porosity decreased from 90% to 7%. As shown in our previous study, HA was less effective in increasing the strength and modulus of porous PU foam because the scaffolds mostly consisted of empty space because of the large number of pores. However, as the pore volume decreased, the volume fraction of HA increased, and the HA reinforcing effects were enhanced as the densification process proceeded. Thus, the stiffness of the densified PUH composite system was more greatly affected by the stiffness of HA.

In vivo histology analysis

Capsule surrounding the PU and PUH was observed after stained with H&E protocols (**Figure 3.2.5**). The main constituents of the capsule were collagen stained with pink, and small inflammatory cells were stained with purple. At early stage (2 week after implantation), inflammation still was in progress and a number of inflammatory cells were observed inside a capsule in both PU and PUH treated samples. However the number of inflammatory cells was significantly large in PU than PUH since HA alleviated the foreign body reaction profoundly. Also, capsule thickness of PU treated one was quite thicker than that of PUH (**Figure 3.2.6**). It was related to the large number of inflammatory cells found in a capsule. The active macrophages and neutrophils promote the early stage of foreign body reaction and accelerate the capsule formation. At late stage (6 week) collagen was obviously seen as a wavy fiber. If the collagen density is high, in other words, fibrosis occurred, contracture force would be generated, resulting in severe capsular contracture. PUH treated capsule had a loose collagen capsule while PU treated one had highly dense collagen layer. Generally, HA effectively prohibited the foreign body reaction of polymeric materials by its bioactive property.

In addition, actual auricular prosthesis was fabricated through the metal 3d mold as depicted in **Figure 3.2.7 (A)**. Its contour (helix, and anti-helix structure) was clearly detected as a natural ear wherever seen at the top or side view. Also, elastomer prosthesis could maintain its shape stably after being inserted inside the tissue without deformation or contracture.

Anisotropic mechanical properties of multilayered PUH

A multilayered structure was successfully fabricated using PUH 10 for the top and bottom layers and porous PU foam for the core layer. From the cross-sectional SEM images of the multilayered PUH, each layer was well established and combined without any detachment (**Figure 3.2.8(A)**). To verify the interfacial integrity between the porous and dense layers, a tensile test was conducted along the vertical direction (**Figure 3.2.8(B)**). In the low-strain region, the multilayered PUH was stiffer than the porous PUH because the interfacial force was strong enough to endure the deformation. As the strain increased, the interface between the densified and porous PUH layers weakened; however, the scaffold maintained its structure until the fracture strain of porous PUH.

The load-bearing function of a meniscus is controlled by its distinctive anisotropic mechanical properties [142]. It has different stiffnesses in different directions; E_z (parallel to the z-axis) and E_{xy} (perpendicular to the z-axis) are 75–150 and 75–150 MPa, respectively [143]. The low E_z is advantageous for the meniscus to effectively absorb impact, whereas the high E_{xy} is essential to prevent deformation and to enable the meniscus to retain its shape. Compressive and tensile tests were performed to confirm the anisotropic mechanical properties of the multilayered structure as a function of the elongation direction (vertical compression and lateral tension). The representative compressive stress–strain curve in **Figure 3.2.9(A)** is concave up, with small strength because the forces were concentrated on the less stiff porous core layer rather than on the dense top and bottom layers. However, the representative tensile stress–strain curve in **Figure 3.2.9(B)** is concave down, indicating a much higher moduli and strength because the elongation force was focused on the stiff and strong dense layer. During elongated, crack occurred at the center part of the porous layer because of the concentrated stress on the interface. However, it didn't influence the mechanical property and structure of the scaffold much until the fracture stress since the layers remained adherent each other. The average stiffness was 116 ± 45 kPa (compressive modulus) and 68 ± 3 MPa (tensile modulus) (**Table 4**). The original functions of the meniscus (the cushioning effect, impact absorption property, and elasticity) can be achieved by these directional-dependent moduli.

Furthermore, densified PUH is a versatile material that can be easily modified into various

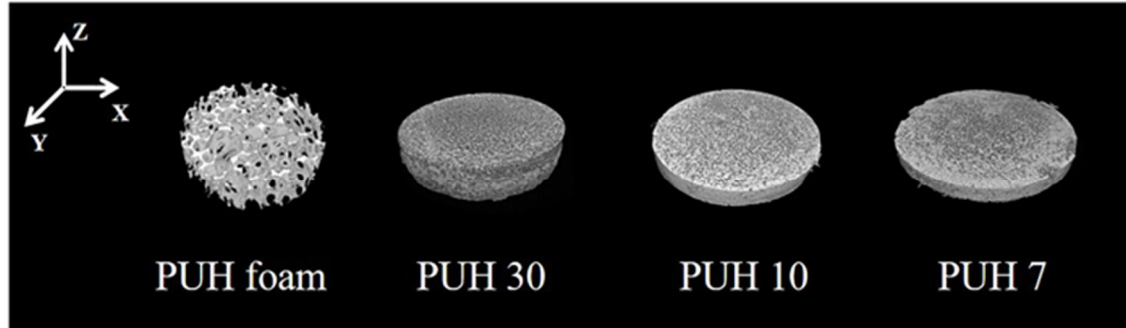
functional scaffolds. Two types of advanced scaffold designs are suggested for other purposes: a high-shear-resistant scaffold (pocket-shaped scaffold) and a reverse multilayered structure (porous/dense/porous structure). Because meniscus replacements are frequently placed under shear deformation, a pocket-shaped scaffold could provide strong resistance to shear forces. The dense barrier covering around the core would effectively protect the porous layer in the pocket from external shear forces to prevent the concentration of forces in the weak porous layer. Moreover, a reverse multilayered structure could be easily fabricated to guide neighboring tissue ingrowth and provide sufficient space for new tissue regeneration. This design would enhance the integrity between the scaffolds and surrounding tissues, resulting in stable implantation.

3.2.4. Conclusions

A multilayered PU-based scaffold with HA was successfully fabricated for efficient artificial meniscus replacement. In densified PUH, HA was homogeneously dispersed in the PU matrix and enhanced the mechanical properties of PU, especially the tensile strength and modulus. Using densified PUH 10 and porous PU in foam states, a dense/porous/dense multilayered structure was produced using a simple pressing method. In addition, high interfacial strength was achieved between the porous and dense layers, indicating the good structural stability of the framework. Its anisotropic mechanical properties were also adjusted to levels comparable to those of natural menisci, with similar E_z and E_{xy} . Finally, other designs such as a pocket-shaped scaffold and a reverse multilayered structure for more efficient artificial meniscus replacement can be achieved by simple densification and a layer-by-layer stacking process, producing excellent results.

Figures

(A)



(B)

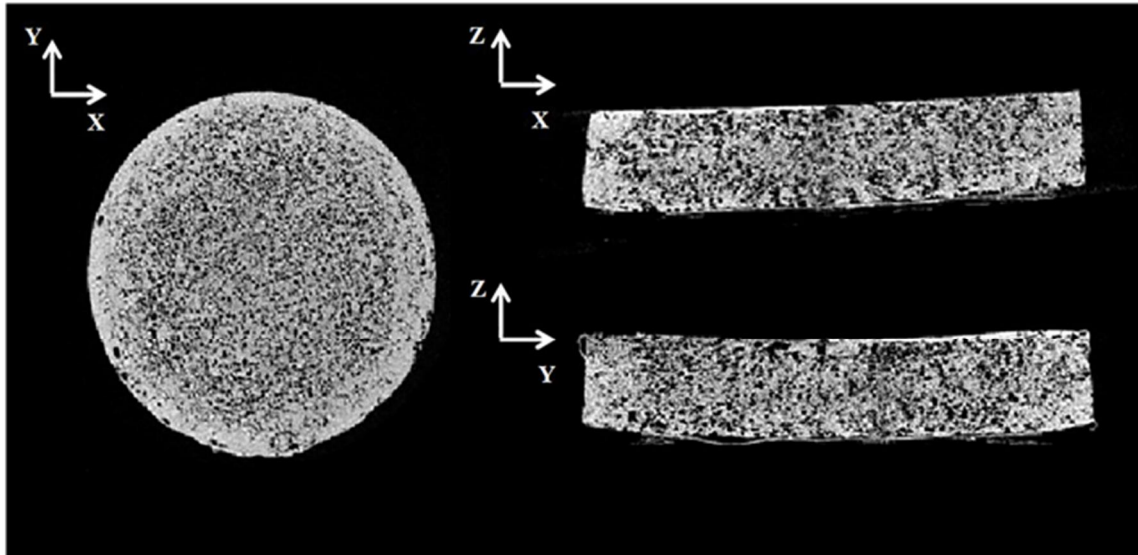


Figure 3.2.1. (A) μ -CT images of porous PUH foam and densified PUH 30, PUH 10, and PUH 7. The number indicates the porosity of each group. (B) 2D μ -CT images of XY, YZ, and ZX planes of PUH 10 sample.

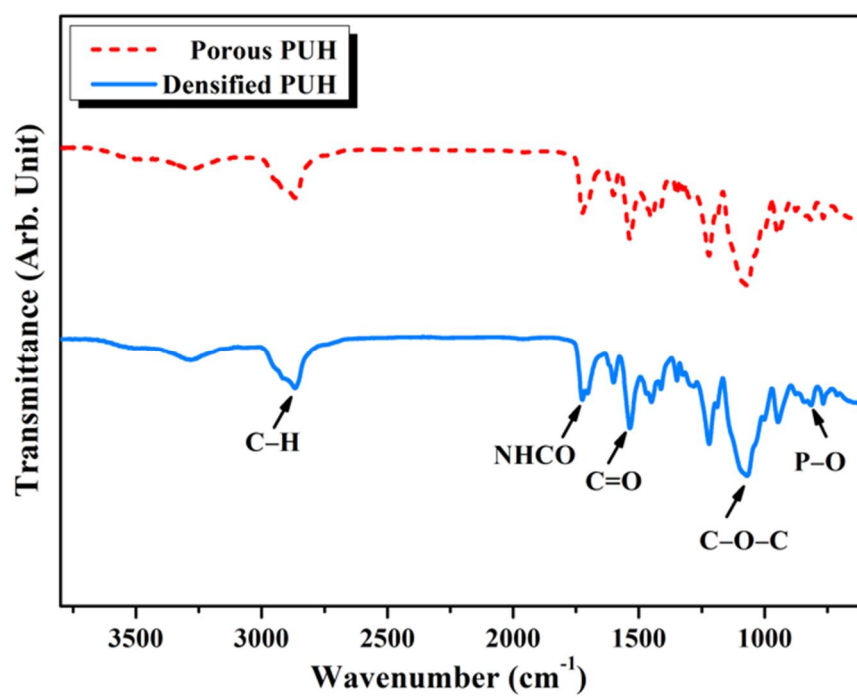


Figure 3.2.2. FT-IR spectra of porous PUH and densified PUH 10

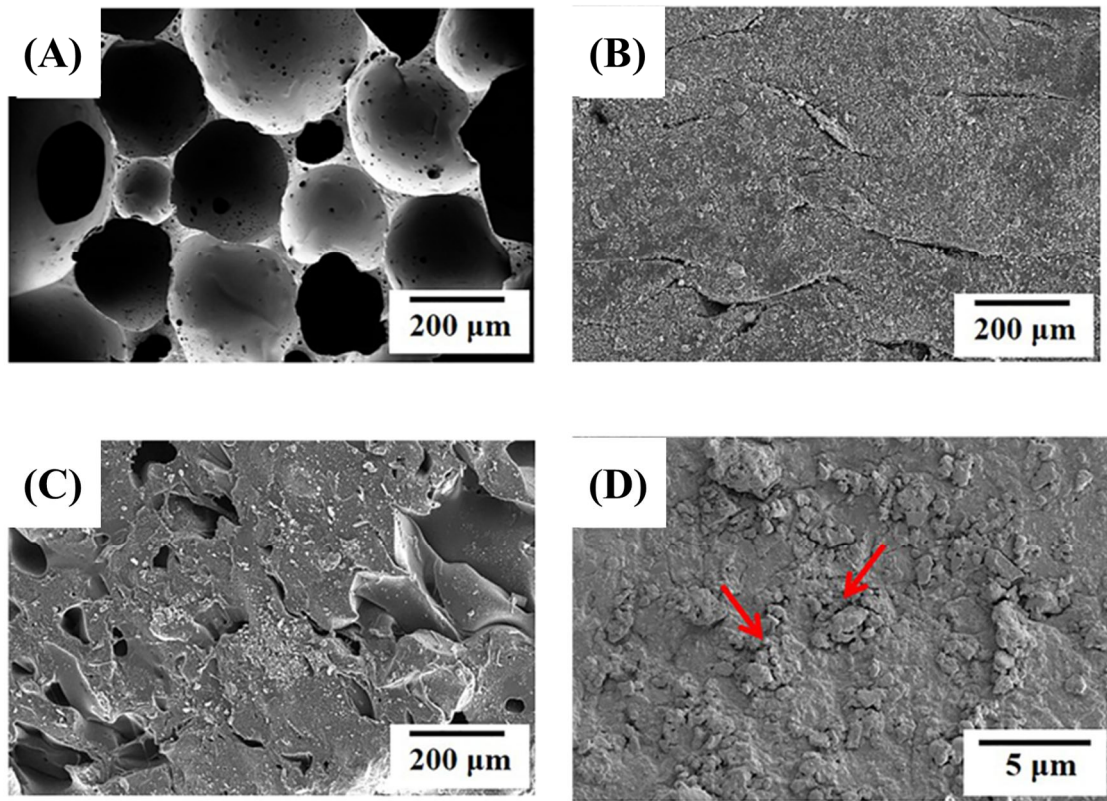


Figure 3.2.3. SEM images of (A) PUH foam and (B) outer surface and (C) cross-section of densified PUH 10. (D) High-magnification image of HA on PUH 10 surface (the arrows identify mineralized HA particles on the surface).

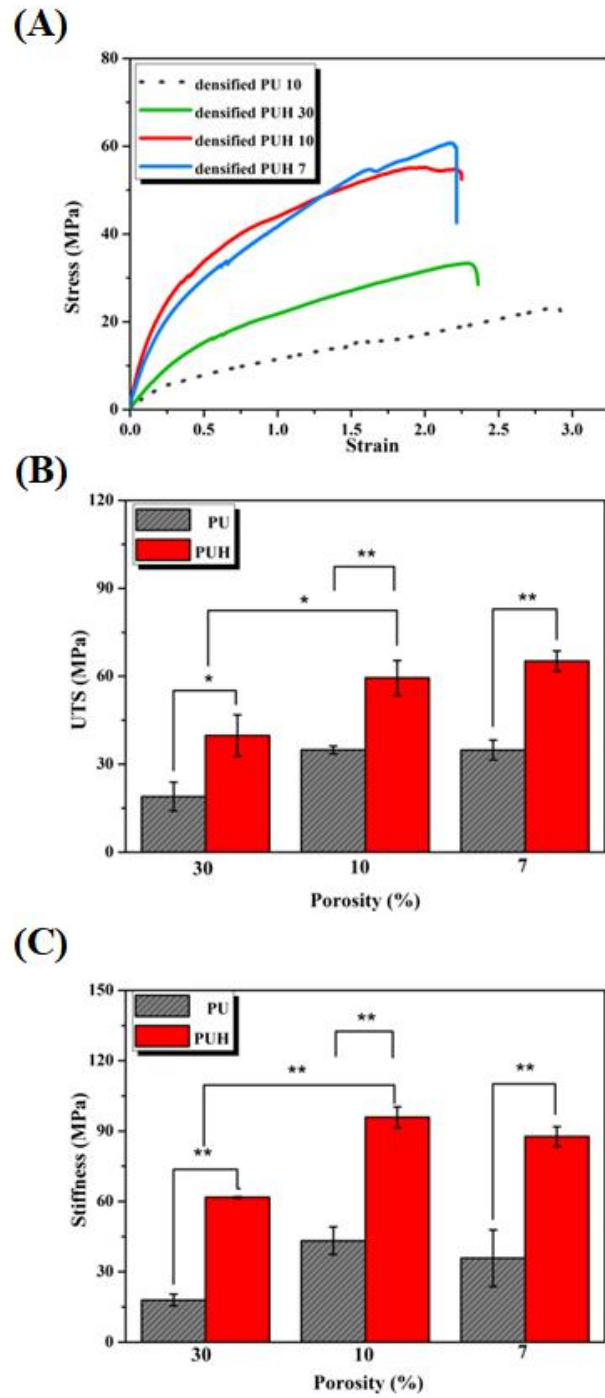


Figure 3.2.4. (A) Representative stress–strain curves of densified PU 10 and densified PUH (PUH 30, PUH 10, and PUH 7). (B) UTS and (C) stiffness change of densified PU and PUH (porosity: 30%, 10%, and 7%). (* $p < 0.05$, ** $p < 0.01$)

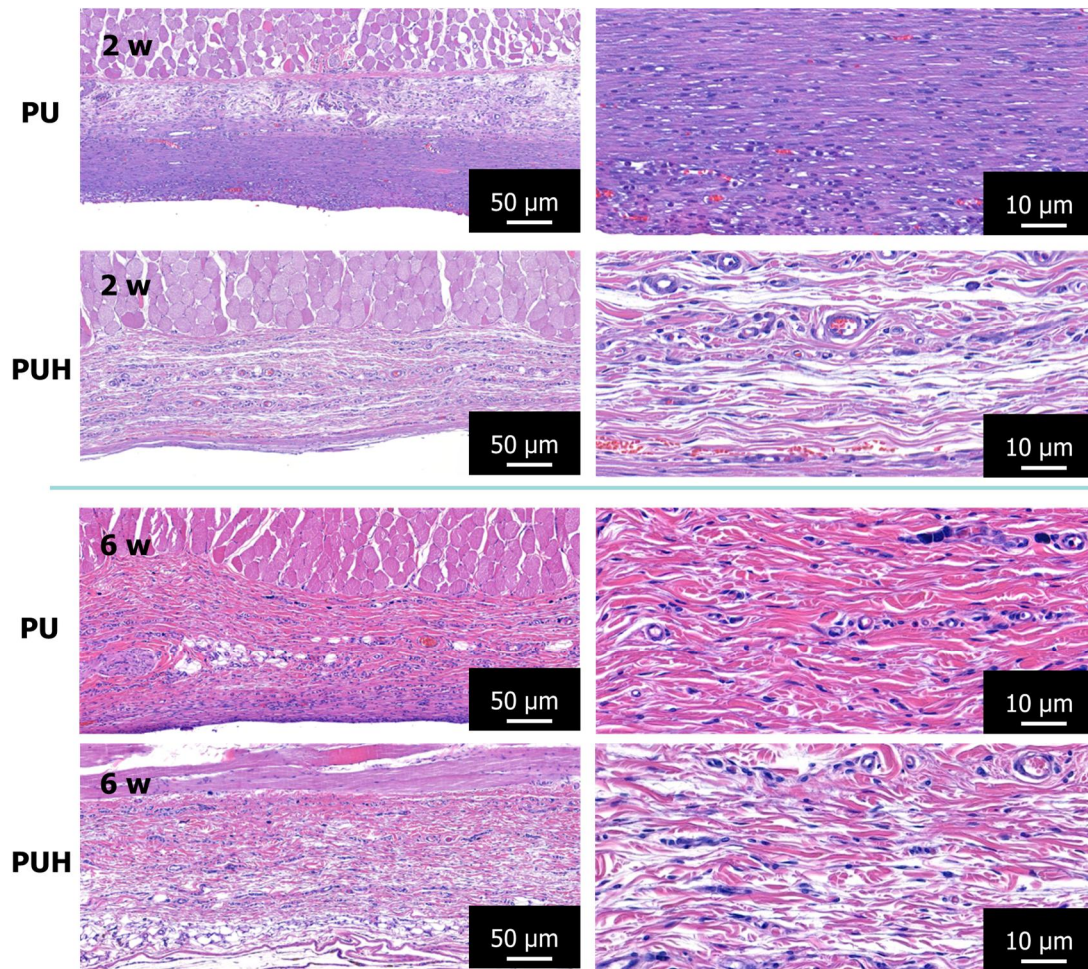


Figure 3.2.5 Histological evaluation of collagen capsule extracted from rat dorsal skin after 2 and 6 weeks of PU and PUH implantation

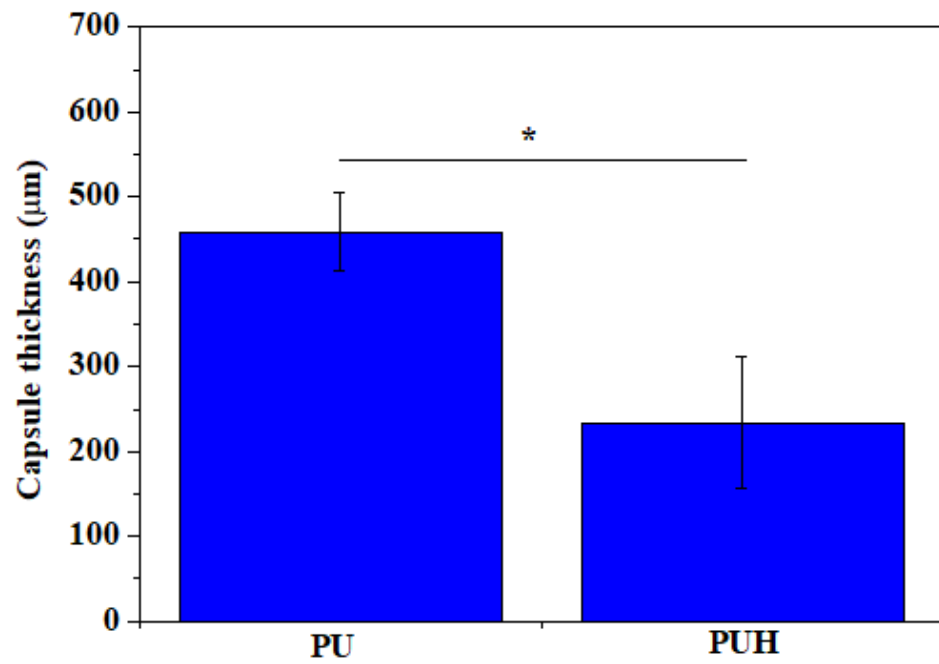


Figure 3.2.6 PU and PUH treated capsule thickness obtained from 2 week histology images

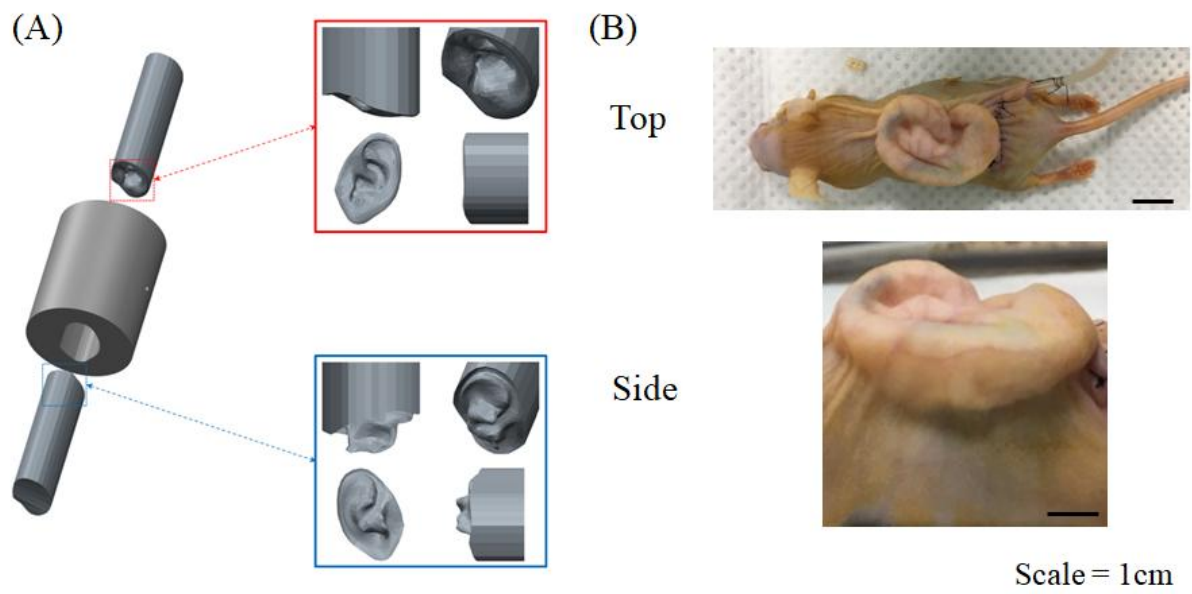


Figure 3.2.7 (A) metal mold designed from STL files to print auricle prosthesis and (B) PUH microtia after being inserted beneath the dorsal tissue of nude mice (balb/c, male)

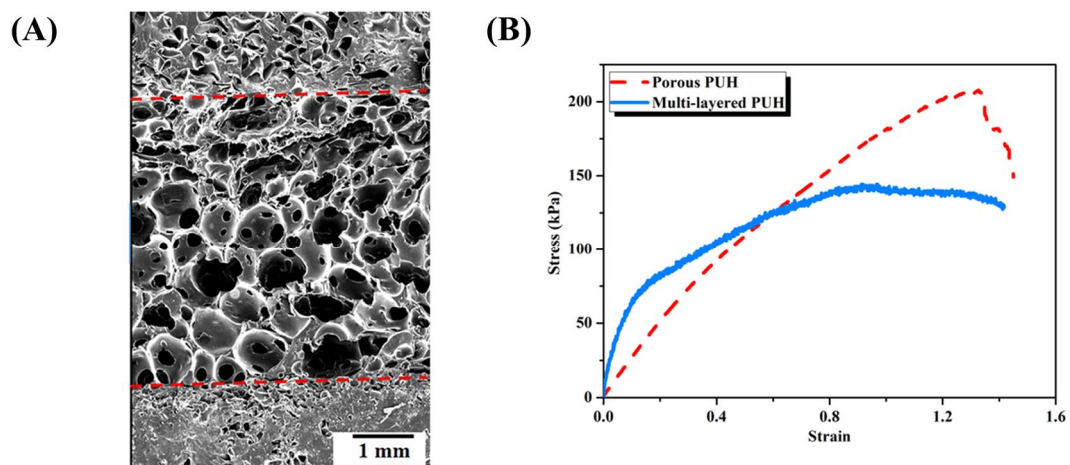


Figure 3.2.8 (A) Cross-sectional SEM image of multilayered PUH and (B) representative stress–strain curves of multilayered PUH and porous PUH.

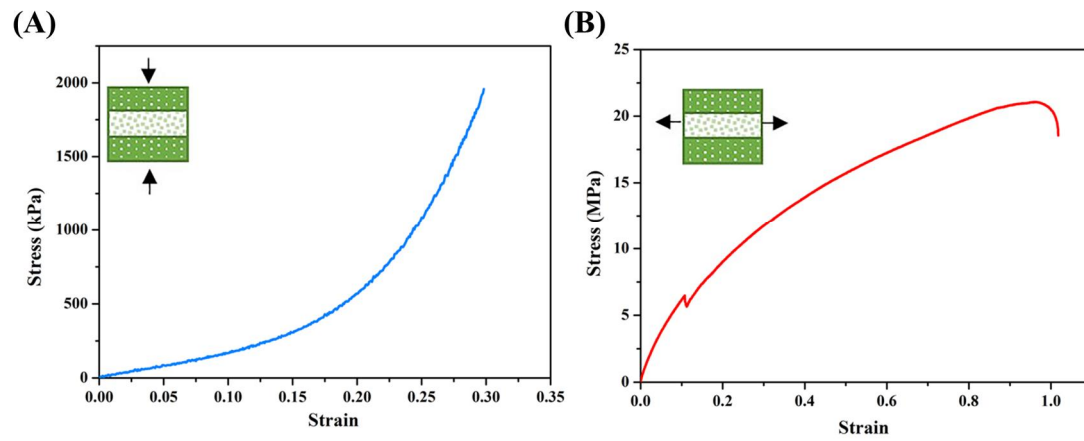


Figure 3.2.9 Representative stress–strain curves of multilayered structure: (A) compression test parallel to the stacking direction and (B) tensile test perpendicular to the stacking direction.

Chapter 4.

Use of Thioglycerol on Porous Polyurethane as an Effective Theranostic Capping Agent for Bone Tissue Engineering

4.1 Introduction

Polyurethane (PU) is a promising material for drug delivery supports because of its biocompatibility, stable chemical structure, and inherent porous structure, providing a large surface area for carrying drugs [144, 145]. However, despite its large surface area, its low affinity to biomolecules such as peptide, proteins, and therapeutic agents leads to burst release issues [146, 147]. The weak interaction between the synthetic elastomer and proteins generally originates from the relatively small number of functional groups to attract proteins in conventional synthetic polymers and difficulty in changing the chemical structure in the polymer chain unit [148]. However, PU can be easily tailored chemically for pharmaceutical and biomedical applications. The chemical modification of PU to enable the strong adherence of drugs to the polymeric substrate has been extensively achieved by employing a functionalized polyol or chain extender in the pre-polymer preparation steps [149].

The most effective method to increase the affinity of drugs to the polymeric scaffold is to adopt a protein–polymer conjugate system [150, 151]. For instance, an *in situ* one-pot peptide–polymer bioconjugate has been demonstrated to be effective in elevating the stability of the peptide, including oxytocin, which is vulnerable in aqueous solutions alone [152]. Dithiophenol maleimide functionalized polymer was used as a disulfide bridging agent for oxytocin, which is known to undergo *in situ* reversible conjugation to overcome the low solution stability and enhance the potential storage capacity/shelf life of the peptide before administration [152]. Amide formation resulting from coupling with amines (a reaction of an amine with N-succinimidyl activated ester, pentafluorophenyl activated ester, and a carboxyl acid with N,N'-dicyclohexyl carbodiimide) rich in biomolecules is also frequently adopted in protein–polymer conjugate systems [153]. In addition, the protein polymer conjugate can be linked via a reaction of thiol groups, forming a disulfide via a disulfide exchange between two molecules or thioether by a Michael addition [153].

For protein–polymer conjugates, a reversible conversion of the thiol and disulfide has been adopted in drug delivery systems to increase the drug carrying capacity, affinity, and chemical

stability in the solution [154]. Covalently linked bioconjugates between therapeutic agents and the polymeric scaffolds through disulfide bonds dictate a successful outcome [155]. The linkage can be formed by a reaction of two sulfhydryl groups of —SH-containing material, of which the most representative material is a cysteine [156]. The strategy to use a disulfide for a drug delivery system is to use a reductive cleavage of the disulfide via an endocytic pathway with redox enzymes, including glutathione (GSH) and thioredoxin reductase, which maintain a high free —SH level in the cytosolic space [157]. On the basis of the perspective of reversible cleavage inside the human body, disulfides were applied in targeted theranostic drug delivery, especially for anticancer agents, as GSH is abundant in tumors [158].

In this study, we used thioglycerol to synthesize thiol conjugated biodegradable PU, which not only provides thiol groups but also participates in a foaming reaction as a chain extender to improve both the peptide affinity and chemical stability. Thioglycerol is a derivative of glycerol, a widely used and highly reactive chain extender, with one hydroxyl group converted to the thiol. Thus, thioglycerol can be easily conjugated with PU using a one-pot synthesis because of the similarities in the molecular structures. After being conjugated, free thiols exhibited a strong attraction with the growth factors by forming reversible disulfide bonds. The chemical structure of the modified PU during each synthesis step was monitored. In addition, the degradation property and drug delivery mechanics of the modified PU were evaluated. Moreover, its feasibility as a BMP-2 carrier was studied using *in vitro* differentiation tests and *in vivo* animal tests for accelerated bone tissue regeneration.

4.2 Experimental procedure

Thioglycerol conjugated biodegradable polyurethane preparation

TG-DPU was synthesized in two steps: 1) DPU formation, which consisted of the addition of a representative biodegradable polyol, polycaprolactone diol (PCL-diol, Mw~530, Sigma Aldrich, USA), and 2) TG-DPU formation, which consisted of thiol conjugation to DPU using thioglycerol

(Sigma Aldrich, USA). A pre-polymer (Hypol 2002, Dow chemical, USA) was used as a fundamental urethane chain that could be transformed into a hydrophilic porous scaffold via a fast foaming reaction with water. Predetermined amounts of PCL-diol (0, 12.5, and 25 wt% compared with the amounts of monomer) were added to the pre-polymer after an activation process at 80 °C under N₂ conditions for 3 h with 0.03% Sn(Oct)₂ (tin(II) 2-ethylhexanoate, Sigma Aldrich, USA) as a catalyst, to form DPU. TG-DPU was fabricated by adding thioglycerol (0, 0.05, 0.1, and 0.2 wt%) to DPU at room temperature (25 °C) for 1 h. Finally, distilled water was added with vigorous stirring until porous foams were generated. Then, the foams were poured into the mold and dried in air.

Chemical structure characterization

Nuclear magnetic resonance (NMR) spectroscopy (JeolJNM-LA400 with LFG, JEOL, Japan) was performed at the ¹H resonance at 23°C using an internal standard to analyze the chemical structure of DPU and TG-DPU. Before forming the foam, the samples were prepared by dissolution in dimethyl sulfoxide-d₆ (DMSO-d₆, Sigma Aldrich, USA).

Degradation test

The degradation property of DPU with different PCL compositions in the soft segment of polyurethane (0, 12.5, and 25 wt%) was characterized by measuring the weight change of the DPU foam after 35 days of being immersed in phosphate buffered saline (PBS). In addition, the microstructure of DPU after degradation for 2 months was examined using field-emission scanning electron microscopy (FE-SEM; SUPRA 55VP, Carl Zeiss, Germany).

Growth factor loading on TG-DPU

To visualize the remnant amounts of proteins on TG-DPU under physiological conditions, green fluorescent protein (GFP, produced using *E. coli*) was loaded onto both DPU and TG-DPU by immersing them in the GFP solution. The GFP-loaded samples were then dipped inside PBS for 0, 1, 4, and 7 days; the media was changed every day with the light blocked. Each sample was examined

using confocal laser scanning microscopy (CLSM; SP8 X, Leica, Germany).

BMP-2 (rhBMP-2 produced using *Escherichia coli* (*E. coli*) 26 kDa, Homodimer, GEB2-10, Genoss, Korea) was selected to demonstrate the release behavior and bone regeneration effects after delivery using our scaffold in *in vitro* and *in vivo* experiments. The BMP-2 solution was prepared by dissolving BMP-2 powder in sterilized PBS at a concentration of 20 µg/ml. BMP-2-loaded TG-DPU (TG-DPU-B) was prepared by immersing TG-DPU in the drug solution for 1 h in a 37 °C incubator with 0.05% hydrogen peroxide to bridge free thiols between TG-DPU and BMP-2 and was dried under sterilized conditions. After the drug-loading process, the release mechanics were studied. BMP-2 was released in PBS solution for 42 days in the 37 °C incubator. Its turbidity was measured at a wavelength of 220 nm using ultraviolet/visible (UV/Vis) spectroscopy (V-770, JASCO, USA) and was converted into quantitative amounts using the standard curve.

The elemental composition at the surface of TG-DPU-B was investigated using electron spectroscopy for chemical analysis (ESCA, Sigma probe, VG, UK). Monochromatic Al-K α was selected as the X-ray source (15 kV, and 375 W). The analysis was conducted using both a wide scan with a pass energy of 80 eV and a narrow scan with a pass energy of 20 eV. The results were analyzed using ESCape software to find a fitting curve for each peak.

***In vitro* cell tests**

The biocompatibility and bioactivity in the cell differentiation of TG-DPU-B was evaluated using an *in vitro* cell methoxyphenyl tetrazolium salt (MTS) assay and alkaline phosphatase (ALP) experiments, using a pre-osteoblast cell line (MC3T3-E1; ATCC, CRL-2593, Rockville, MD, USA). Cells with a density of 2×10^4 cells/ml for the MTS assay were seeded on the specimens prepared in a square with dimensions of 1 cm \times 1 cm. For the ALP activity assay, cells with a density of 0.5×10^4 cells/ml were seeded on a square specimen with dimensions of 4 cm \times 4 cm. The specimens were cultured in 10% FBS medium at 37°C in an incubator under 5 % CO₂. For comparison, DPU, TG-DPU, and DPU-B were prepared in the same way.

For the MTS assay, the cells were cultured for 3 and 5 days. After being rinsed with PBS,

they were immersed in FBS-absent medium mixed with a 10% cell proliferation assay kit solution (CellTiter 96 Aqueous One Solution Cell Proliferation Assay, Promega, USA) for 2 h in the 37 °C incubator, blocked from any light. The absorbance of the solution was detected at 490 nm using a microplate reader (Model 550; Biorad, USA). Differentiation of the pre-osteoblasts was assessed using ALP analysis after 14 days of culturing. During the culturing period, the medium was replaced with a new medium containing 10 mM of beta-glycerolphosphate and ascorbic acid at a density of 50 mg/ml after 24 h of seeding. ALP activity was evaluated by quantifying the p-nitrophenol phosphate (pNP) converted from p-nitrophenyl phosphate via the reaction of ALP. The quantitative level of pNP was measured using a microplate reader (Model 550; Biorad, USA) at 405 nm.

***In vivo* animal test**

Four types of specimens (DPU, TG-DPU, DPU-B, and TG-DPU-B) were prepared in disk shapes with a diameter of 8 mm and depth of 2 mm. DPU-B and TG-DPU-B were especially immersed in the PBS-based BMP-2 solution (the concentration of the solution was 50 µg/ml). All the samples were autoclaved after being rinsed for 5 days in PBS. The *in vivo* study using a rabbit calvarial model was performed under the approved protocol (GEN-IACUC-1801-01) of the Institutional Animal Care and Use Committee (IACUC) of Genoss. Male New Zealand white rabbits (2.5–3 kg) were obtained from a commercial vendor, which addresses the specific-pathogen-free (SPF) grade of animals (KOSA Bio Inc., Seongnam, Korea). After 1 week of adjustment, surgery was conducted. All the rabbits were anesthetized through intramuscular injection of a combination of 0.5 mL of 2% xylazine HCl (Rompun, Bayer Korea, Korea), 1 mL of tiletamine HCl (Zoletil, Vicbac Laboratories, France), and lidocaine (Yuhan Corporation, Korea). Four defects with the same dimensions as the specimens were made symmetrically in the rabbit skull at 1.5-cm intervals using a stainless-steel biopsy punch. Four different specimens were inserted into the defects, and the defects were closed with sutures. For 3 days after surgery, gentamicin (Dongkwang Pharmaceutical Co., Seoul, Korea) was administered intramuscularly at 4×10^5 U each day. After 4 weeks of implantation, the rabbits were sacrificed, and the samples and surrounding tissues were extracted and immediately

fixed in 10% formalin.

Micro-CT analysis

Newly formed bone in the defect was evaluated using micro-CT (Skyscan, 1172 microtomography System; Skyscan, Kontich, Belgium) with a 0.5-mm aluminum filter at a resolution of 24.86 μm , voltage of a 100-kV X-ray source, and current of 80 μA to clearly visualize the regenerated bone. Images were reconstructed using the commercial software NRecon (Bruker microCT, Kontich, Belgium). Top-view and cross-sectional images of the defects were obtained using Data Viewer (Bruker microCT, Kontich, Belgium), and the recovered bone volume was calculated using CTAn programs (Bruker microCT, Kontich, Belgium).

Histological observation

After being decalcified in 4% ethylenediamine tetraacetic acid for 10 days, the bone samples were washed, dehydrated with ethanol, and embedded in paraffin. Paraffin blocks were made such that the cross-sectional view of the bones was exposed and cut into sections with 3- μm thickness. The slices were stained using Goldner's trichrome to visualize new bone formation clearly. The mature bone and immature new bone matrix were stained deep blue and light cyan blue, respectively. Microscopic images of the stained slices were obtained using a digital slide scanner (Panoramic 250 Flash III, 3DHISTECH Ltd., Hungary).

Statistical analysis

All the quantitative variables were presented as means \pm standard deviations (SDs) with a minimum number of $n=3$. The validity of the data, especially the one-way analysis of variance, was evaluated using the Statistical Package for the Social Sciences (IBM, New York City, USA), a statistical software program. The statistical significance was set at $*p < 0.05$ and $**p < 0.01$.

4.3 Results and discussion

Material characterization

DPU and TG-DPU were fabricated using the two-step synthesis method shown in **Figure 4.1**. The soft segments of DPU are composed of PCL, which can be bio-degraded under physiological conditions, and thiols would be exposed at TG-DPU after the second step in which thioglycerol was added to DPU. Then, the chemical structures of DPU and TG-DPU were characterized using ¹H-NMR analysis stepwise. The NMR results analyzing the molecular structure of PU (TDI), DPU, and TG-DPU are presented in **Figure 4.2**. Because PCL was incorporated in DPU and TG-DPU, its characteristic peaks were clearly observed in both groups and are labeled as a–e. [159, 160]. In addition, because of the conjugation of thioglycerol, new peaks assigned to the methyl protons (a') next to the thiol ($\text{CH}_2\text{-SH}$) and the protons of thiol (b') appeared as a doublet of multiplets in the range of 2.4 to 2.6 ppm and 1.8 ppm, respectively, in TG-DPU [161]. It is evident that thioglycerol was successfully reacted with DPU, as designed, as shown in **Figure 4.1**. The reaction was successfully achieved by simply mixing the chemicals because thioglycerol is a simple derivative of glycerol in which one hydroxyl group is substituted by a thiol with two hydroxyl groups retained that can easily form urethane bonds with free isocyanates of DPU, as shown in the molecular structure of TG-DPU.

Degradation behavior

The degradation property of DPU (PCL contents: 12.5% and 25%) was evaluated during 35 days of immersion (**Figure 4.3(A)**). Degradation slowly occurred in PU, the comparison group; 2 wt% PU was disintegrated because of the slow hydrolytic degradation at urethane linkages. To control the degradation rate of PU, PCL, which has numerous ether and ester groups with fast degradation mechanics under wet conditions was incorporated into PU as a soft segment. The degradation rate was greatly accelerated in DPU; 5 wt% from DPU 12.5% and 10 wt% from DPU 25% was degraded compared with PU (35 days). After 14 days of the degradation test, wrinkles and micropores with

diameters of 1–2 μm were observed on the surfaces, providing evidence of degradation (**Figure 4.3(B)**). The number of micropores and wrinkles greatly increased with increasing PCL content.

Drug-release mechanics

The drug-carrying capability was visualized using GFP release tests and CLSM (**Figure 4.4(A)**). Directly after the GFP was loaded on DPU and TG-DPU, green signals were detected on both groups. However, the signals did not last after Day 4 in DPU, whereas they remained in TG-DPU even after 7 days of the release test. Proteins could not be stably carried in DPU because GFP was only physically attached on PU without any chemical interaction and was rapidly released during the early stage of immersion in PBS. However, green lights were homogeneously distributed over the entire surface for 7 days in TG-DPU. Chemically linked GFP was not easily detached from the surface, maintaining its fluorescence without any deterioration. This finding indicates that the affinity of TG-DPU to proteins was greatly improved, indicating its great potential to be utilized in various protein-based drug-delivery systems.

Quantitative evaluation of the effects of the thiol on the drug-release mechanics was performed using another growth factor, BMP-2. The drug-delivery capabilities of DPU and TG-DPU (PCL content: 25 wt%; thioglycerol contents: 0.05 wt%, 0.1 wt%, and 0.2 wt%) were compared for 42 days (**Figure 4.4(B)**). Over 50% BMP-2 was released within 3 days in all the groups and was physically stacked on the scaffold. The BMP-2 was fully released in a very short time in DPU, and no additional BMP-2 was released after day 3. In addition, the total amount of BMP-2 released from DPU was 340 ± 35 ng. However, a relatively large amount of BMP-2 remained on TG-DPU after the initial burst release and was gradually released for 42 days, undergoing a chemical interaction with thiol groups of TG-DPU, including hydrogen bonds and covalent disulfide. Because of these strong bonds between BMP-2 and TG-DPU, the total amounts of drugs greatly increased to 502 ± 16 (TG-DPU 0.05%), 540 ± 11 (TG-DPU 0.1%), and 594 ± 4 ng (TG-DPU 0.2%) compared with that for DPU (comparison group). In addition, the total amounts of drugs increased with increasing thiol content because of the improved affinity between the proteins and scaffold.

The surfaces of DPU, TG-DPU, DPU-B, and TG-DPU-B were investigated using XPS to confirm the interaction at the interface between BMP-2 and the scaffold (**Figure 4.5(A)**). S2p signals were selectively detected only in TG-DPU, DPU-B, and TG-DPU-B at 163 eV in addition to C-, O-, and N-related peaks. The S2p signals of TG-DPU originated from the thiols conjugated in the urethane chain, and the signals detected at near 163 eV were assigned to disulfide or thiols of BMP-2 of DPU-B. The sulfur spectra were composed of S2p_{1/2} and S2p_{3/2} at 164.1 and 162.9 eV, respectively, with an area ratio of 2:1 from the fitting curve, which are mostly attributed to disulfide or thiol among various thiolates [162, 163]. The intensity of the peak was the strongest for TG-DPU-B because of the strong interaction between BMP-2 and the thiols of the scaffold. The interaction between BMP-2 and TG-DPU was interpreted, as shown in **Figure 4.5(B)**, by considering the *in vitro* release mechanics and XPS spectra. The growth factor could be bound on TG-DPU through 1) physically coupling, 2) a hydrogen bond, or 3) a disulfide bond (covalent bond). Physically coupled drugs are unstable; thus, most were washed out or released abruptly during the early stage. Drugs loaded through hydrogen bonds between the hydroxyl groups of the drug and thiols of TG-DPU have a strong interaction with the polymer chain and could be released more gradually for a longer period. The most efficiently loaded drugs formed disulfide bonds with TG-DPU and could only be decomposed in the targeting area by a cellular redox enzyme, such as protein disulfide isomerase (PDI) and an endosome/lysosome redox enzyme [157].

***In vitro* biological property**

The MTS assay, which indicates the degree of proliferation of cells, was used to determine the biocompatibility of DPU, DPU-B, TG-DPU, and TG-DPU-B as drug-delivering carriers (**Figure 4.6(A)**). The cell viability was constant among the four groups, as BMP-2 and the thiol groups did not affect the biocompatibility of the material. However, cells were well proliferated from Day 3 to Day 5 in all the groups, showing good viability. In addition, ALP tests were performed to determine the drug effects to promote cell differentiation delivered from DPU and TG-DPU (**Figure 4.6(B)**). The drugs were quite effective in inducing differentiation of the pre-osteoblasts; the ALP activity was higher in

DPU-B and TG-DPU-B than in DPU and TG-DPU. Notably, TG-DPU-B exhibited much higher ALP activity than DPU-B because BMP-2 was not delivered steadily for 14 days, whereas sustained release was achieved in TG-DPU-B for a prolonged period, shown in **Figure 4.5 (A)**.

***In vivo* bone regeneration**

Rabbit calvarial defects treated by DPU, DPU-B, TG-DPU, and TG-DPU-B for 4 weeks were examined using μ -CT (**Figure 4.7(A)**). Although the polymers were not detected under the analysis conditions (voltage and current) as an empty space, new bones were clearly visualized. The round defects shrunk with the formation of new bone because they were regenerated from below and from the sides. The effect of BMP-2 in inducing bone formation was clearly observed in DPU-B and TG-DPU-B. Compared with DPU and TG-DPU, the area covered by new bones was larger for the DPU-B- and TG-DPU-B-treated sites. The recovery level was quantitatively analyzed, indicating the percentage of new bone formation except for the area covered by the scaffolds (**Figure 4.7(B)**). New bone was formed by $13.5 \pm 4.1\%$ and $12.7 \pm 1.5\%$ of defects in DPU and TG-DPU, respectively. However, as drugs were delivered through the scaffolds, bone recovery was accelerated. In total, $22.1 \pm 4.7\%$ of the defects were filled with new bone in the DPU-B-treated groups, whereas regeneration was much vigorously performed in TG-DPU-B with $27.7 \pm 5.7\%$ of defects recovered with new bone. The bone-regenerative capacity of TG-DPU-B was quite promising, considering that the defects treated with porous calcium silicate, which is known to be a bioactive material that is superior to conventional tri-calcium phosphate, were covered with 28% of new bone at week 16 [164]. The ALP results (**Figure 4.6**) indicate that the sustained release of BMP-2 caused the pre-osteoblasts to be differentiated into mature osteoblast cells. These mature cells became components of the bone and accelerated the regeneration of new bone.

The defects treated by DPU, DPU-B, TG-DPU, and TG-DPU-B were stained using Goldner's trichrome method, as shown in **Figure 4.8**, to demonstrate the maturity of new bones formed four weeks after surgery. An overall view of the histologic transversal sections ($\times 2$ magnification) is presented on the left, and high-magnification images ($\times 15$ magnification) of

representative newly formed tissues are shown on the right side of **Figure 4.8**. Newly formed bones were mostly observed at the margin of the defects in DPU and TG-DPU, and connective tissues were mostly detected at the center. However, in the BMP-2-treated groups (DPU-B and TG-DPU-B), new bones progressed in the maturation stage, and fully mature bones were observed even in the center of the defect with osteocytes, which consisted of mature bones and indicated the presence of healthy bones [165].

4.4 Conclusion

TG-DPU was successfully fabricated via urethane linkage between thioglycerol and DPU, with exposed thiols, as demonstrated by H-NMR results. The thiols were designed to have drug-capping efficiency through two types of strong chemical interactions with proteins: hydrogen bonds and di-sulfide bonds. XPS analysis revealed both carbon–sulfur (C–S) and sulfur–sulfur (S–S) linkages, providing evidence of the formation of a polymer/growth factor conjugate system. These interactions led to sustained release of proteins, especially of BMP-2, and ensured the stable drug-carrying capability of the scaffold. TG-DPU delivered 1.5-times-higher amounts of drugs for an 8-times-longer period than DPU, which promoted differentiation of pre-osteoblasts, as demonstrated in *in vitro* ALP tests. Moreover, its efficacy as a drug-delivery system was confirmed in an *in vivo* animal model and resulted from the reversible disulfide bonds between the growth factors and TG-DPU, which could stably deliver drugs with a sustained release profile.

Figures

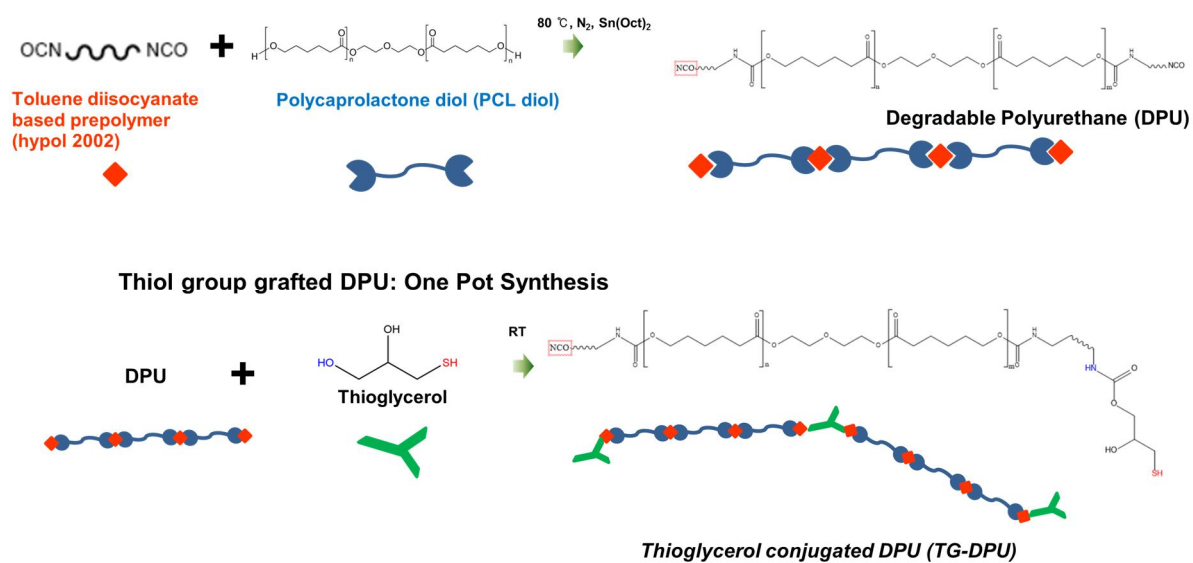


Figure 4.1. Schemes of synthesis of biodegradable polyurethane and thioglycerol conjugation

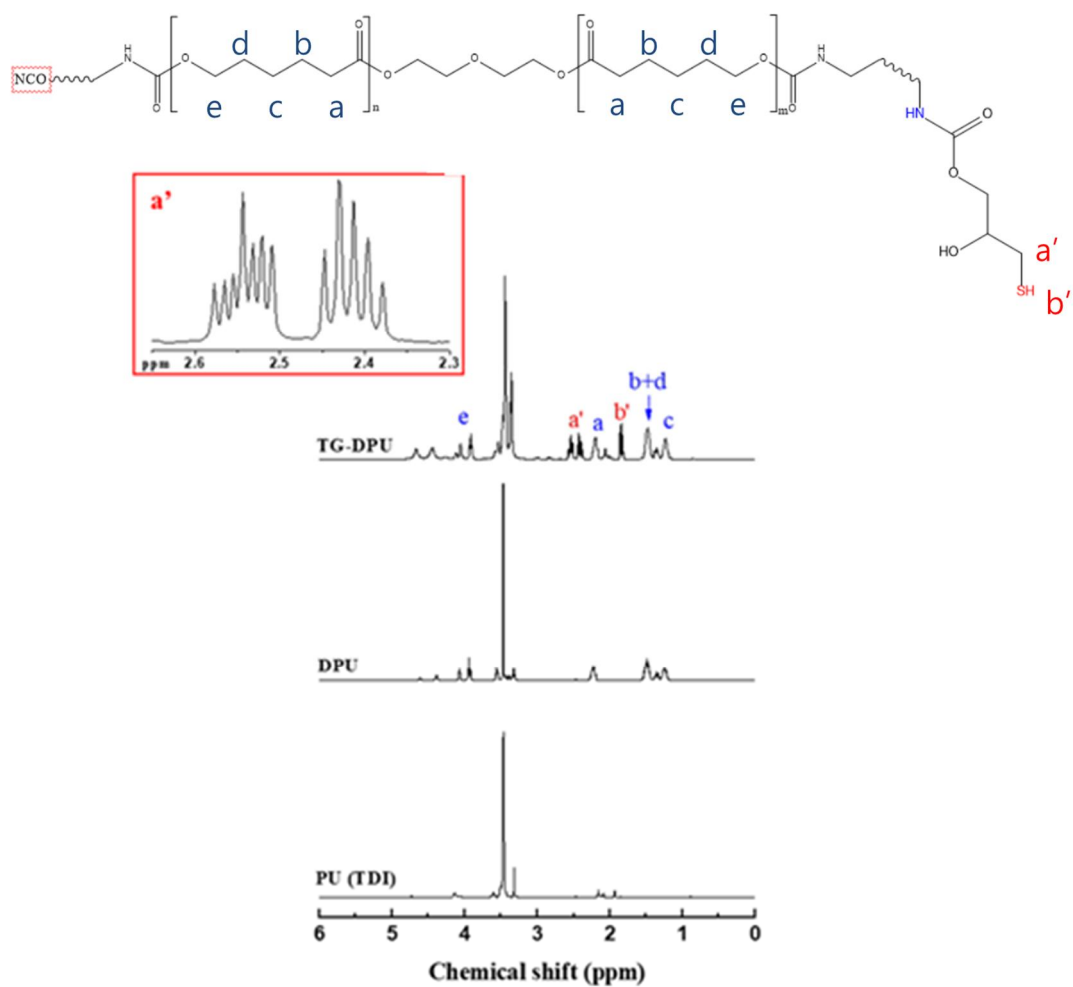


Figure 4.2. ¹H-NMR results of PU (TDI), DPU, and TG-DPU in the range of 0–6 ppm of chemical shift. Representative peaks corresponding to the PCL segment and conjugated thiols are denoted by the letters.

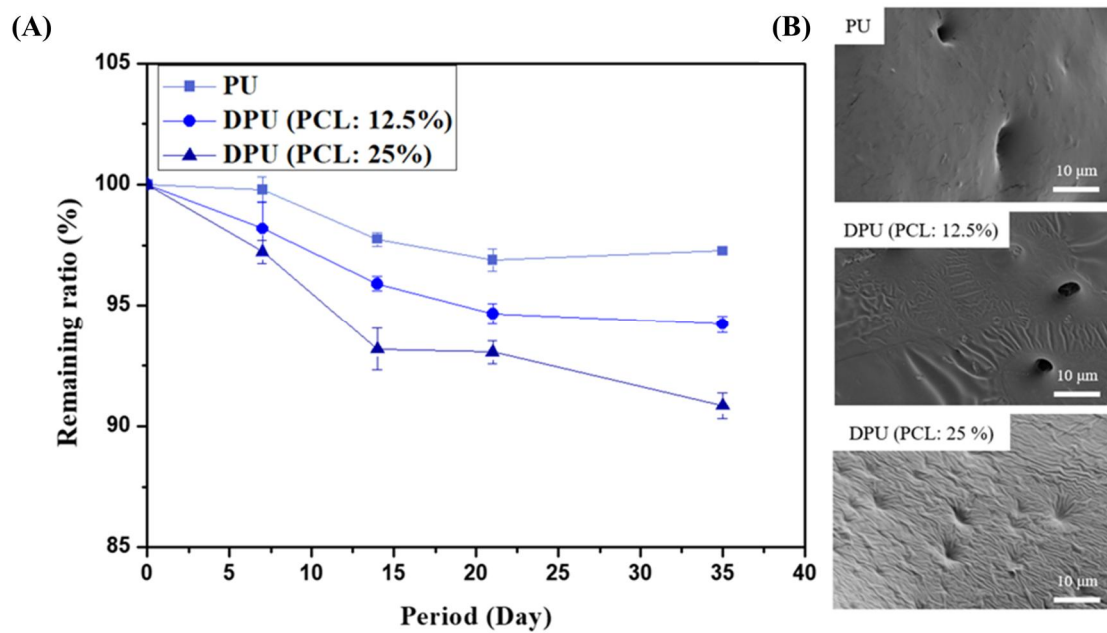


Figure 4.3. (A) Degradation profile for different PCL diol contents of DPU and (B) surface morphology after being immersed for 14 days

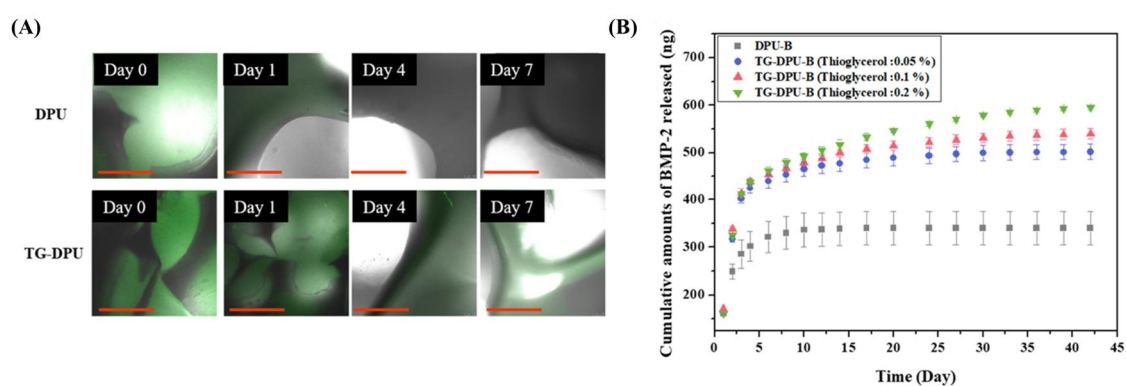


Figure 4.4. (A) CLSM images of DPU and TG-DPU loaded with GFP after release for 0, 1, 4, and 7 days (scale = 500 μ m), (B) BMP-2 release profile of DPU-B (control group, PCL diol: 25 wt%) and TG-DPU-B (thioglycerol contents; 0.05 wt%, 0.1 wt%, and 0.2 wt%, and PCL diol: 25 wt%)

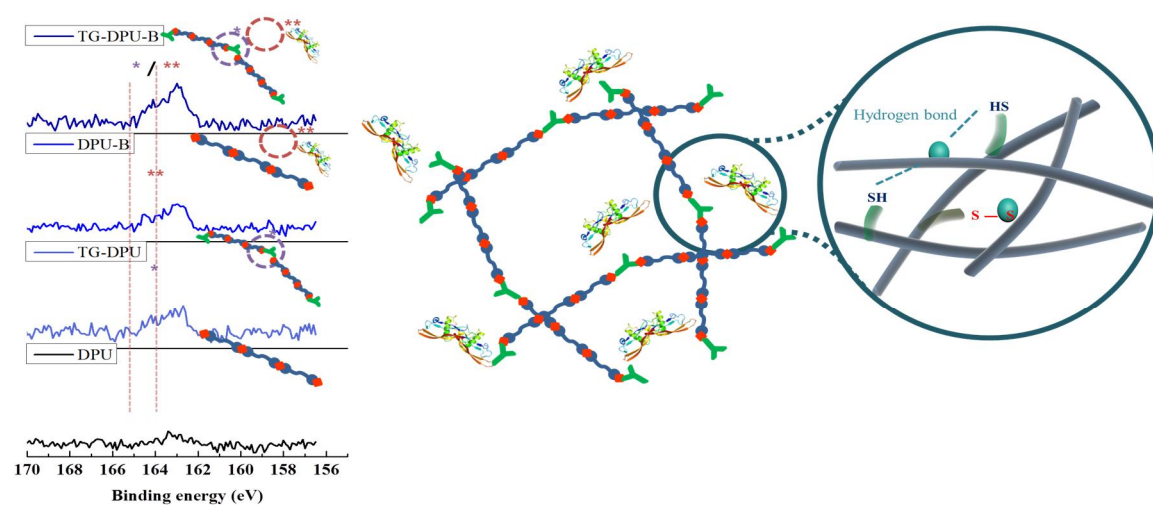


Figure 4.5. XPS spectra for TG-DPU, DPU-B, and TG-DPU-B, showing analysis of the interaction at the interface of BMP-2 and the scaffolds: (A) characteristic peak assigned to sulfur in 163-eV region and (B) schemes of TG-DPU-B forming covalent (-S-S-) and hydrogen bonds at the molecular level

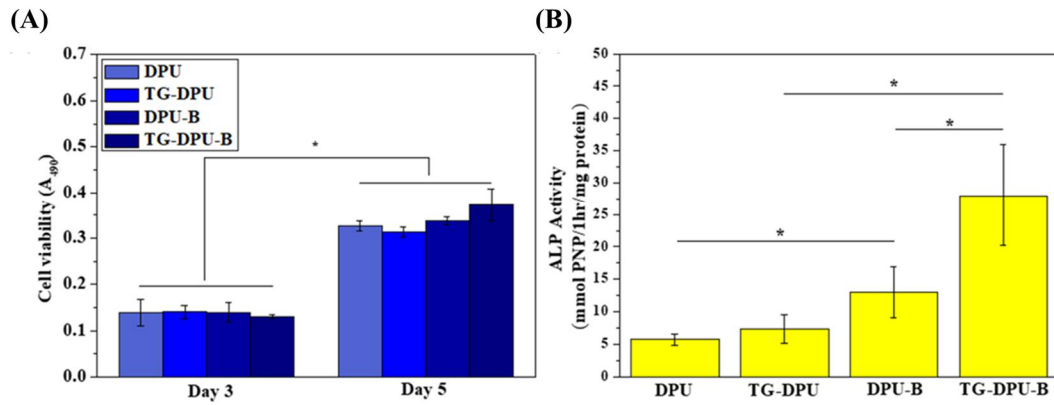


Figure 4.6. (A) MTS results of DPU, TG-DPU, DPU-B, and TG-DPU-B (cell density: 3×10^4) after 3 and 5 days of culturing. (B) ALP activity (cell density: 0.5×10^4) after 14 days of culturing on DPU, TG-DPU, DPU-B, and TG-DPU-B, using ATCC pre-osteoblasts (* $p < 0.05$)

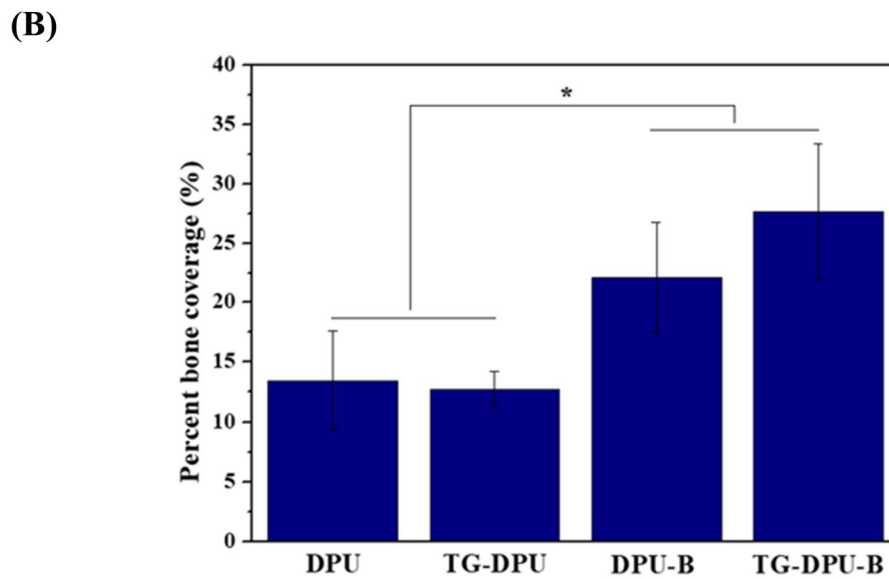
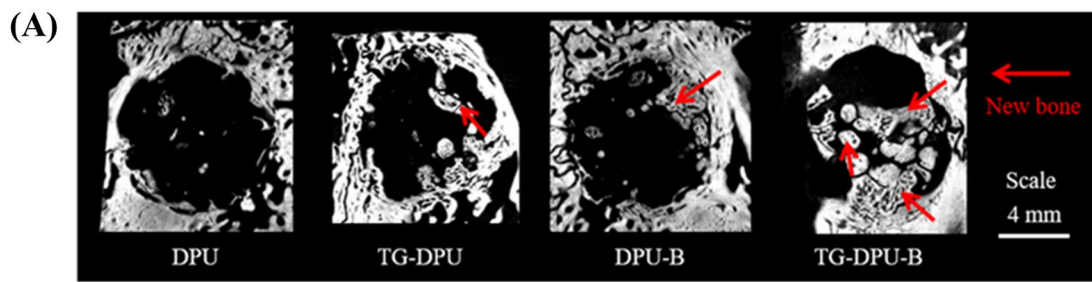


Figure 4.7 (A). CT images of rabbit calvaria treated with DPU, TG-DPU, DPU-B, and TG-DPU-B after 4 weeks of monitoring. The arrows indicate new bone regeneration inside the defects. **(B)** Quantitative analysis of bone coverage calculated using CTan software. (*p < 0.05)

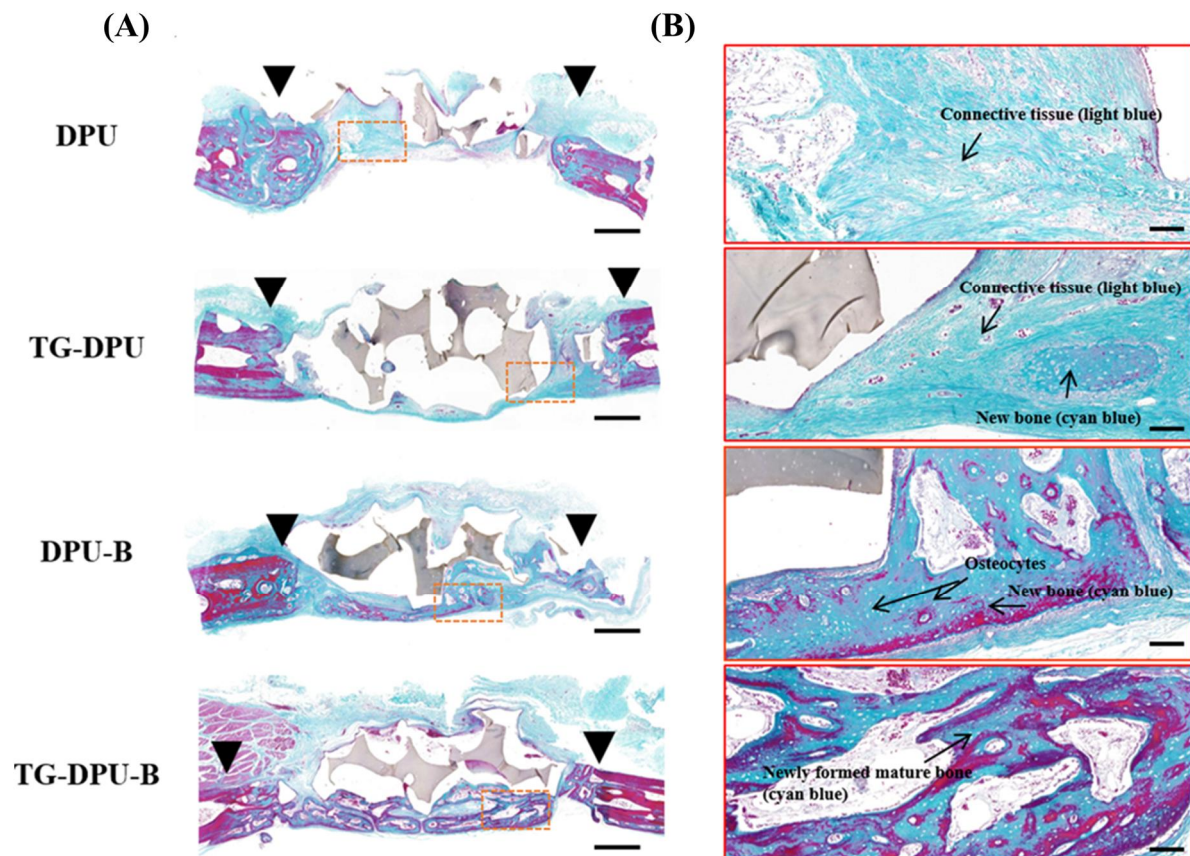


Figure 4.8 . Histology images ((A) ×2 and (B) ×15 magnification) of DPU, TG-DPU, DPU-B, and TG-DPU-B stained by Goldner's trichrome. (A) Overall view of defects recovered after 4 weeks (scale: 1 mm). (B) Newly generated tissues were investigated at higher magnification, as sectioned with red boxes (scale: 100 μ m). The connective tissues were loose and light blue and were not transformed into bones. The new bones were stained cyan blue and became darker as the tissues matured. Osteocytes were embedded in the new bones as white round shapes.

Chapter 5. Conclusion

5.1 Conclusion

In this work, we successfully developed polyurethane based bioactive composite system, adopting various kinds of advanced technique. First, polyurethane was incorporated with silica nano particles produced by sol-gel process during the foaming reaction at the same time. Silica nanoparticles were homogeneously dispersed on polyurethane, improves mechanical property, and biological property. Silica nanoparticles were gradually released from the membrane and release Si ions activated fibroblasts' proliferation and promoted wound healing cascade significantly. Second, polyurethane molecular structure was designed to have free phosphates to gather calcium, carbonate, phosphorous ions, inducing to form CaP particles. CaP particles were stacked on polyurethane surface, especially on the phosphates, and became hydroxyapatite film. PU-gp-HA system was highly bioactive to fibroblasts and osteoblasts to be utilized for tissue engineering scaffolds. Actually, its potential was demonstrated as a cartilage replacement after densification process to meet the mechanical property of natural tissues. Porosity was successfully controlled and mechanical property was significantly improved. Using the molding technique, auricle shaped scaffold was fabricated and its biocompatibility was proven through *in vivo* capsule formation test. Anisotropic meniscus replacement was also successfully fabricated by stacking porous and dense PUH alternately. Lastly, thiolated polyurethane was synthesized using an advanced chain extender which has not only hydroxyl groups but also, thiol groups. Free thiols introduced on polyurethane chains enhanced affinity with growth factor, especially BMP-2 by forming hydrogen bonds and covalent bonds. The covalent bond was di-sulfide which could be reversibly cleaved inside our body. Its drug delivering capability was systematically understood by prolonged release mechanics and its efficacy on bone regeneration test.

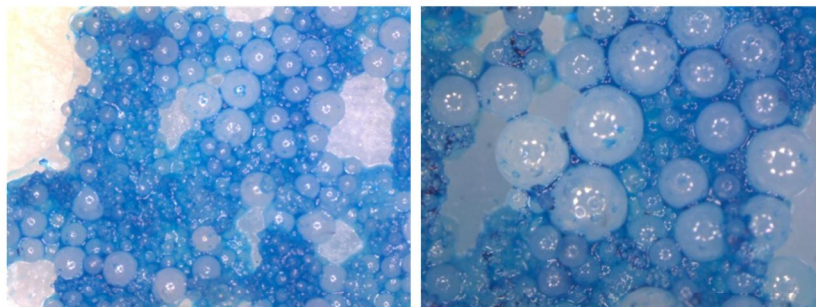
5.2 Further works

The scope of polyurethane can be extended to various biomedical applications through various type of fabrication process. For instance, polyurethane microsphere was fabricated via oil

immersion technique which is usually used method for making hydrogel microsphere. Polyurethane microsphere could be used as filling agents for irregular shape of defects with stably delivering biomolecules, growth factors, or peptides. Polyurethane was also utilized in 3d printing technique. Complex organs or tissues could be reproduced by 3d printing technique, possessing elastic performance with great biological property.

Figure

Microsphere



3D printing (filament)

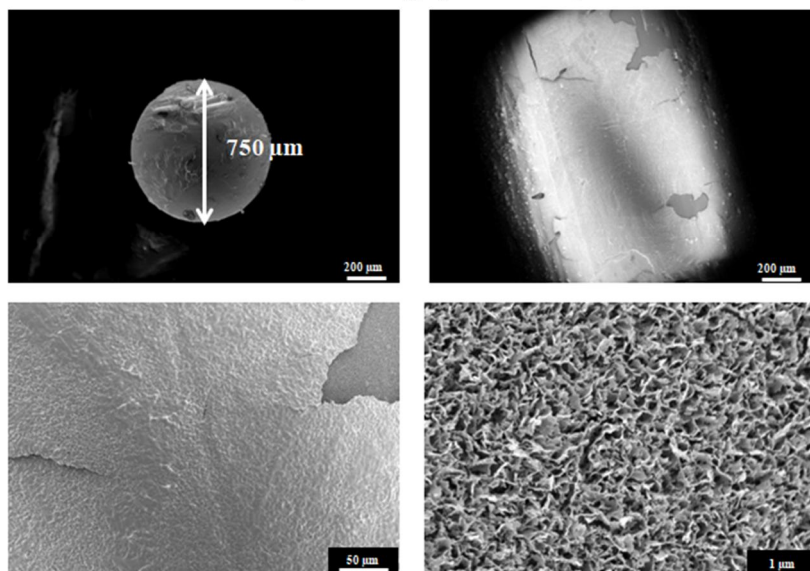


Figure 5. Various applications of PU based material for further works

References

- [1] S.J. Hollister, Porous scaffold design for tissue engineering, *Nature Materials* 4 (2005) 518.
- [2] J.L. Drury, D.J. Mooney, Hydrogels for tissue engineering: scaffold design variables and applications, *Biomaterials* 24(24) (2003) 4337-4351.
- [3] D.W. Hutmacher, Scaffolds in tissue engineering bone and cartilage, in: D.F. Williams (Ed.), *The Biomaterials: Silver Jubilee Compendium*, Elsevier Science, Oxford, 2000, pp. 175-189.
- [4] T.A. Khan, K.K. Peh, H.S. Ch'ng, Mechanical, bioadhesive strength and biological evaluations of chitosan films for wound dressing, *J Pharm Pharm Sci* 3(3) (2000) 303-311.
- [5] H. Bodugoz-Senturk, C.E. Macias, J.H. Kung, O.K. Muratoglu, Poly(vinyl alcohol)-acrylamide hydrogels as load-bearing cartilage substitute, *Biomaterials* 30(4) (2009) 589-596.
- [6] J.Y. Cherng, T.Y. Hou, M.F. Shih, H. Talsma, W.E. Hennink, Polyurethane-based drug delivery systems, *International Journal of Pharmaceutics* 450(1) (2013) 145-162.
- [7] M.W. Laschke, T.E. Schank, C. Scheuer, S. Kleer, S. Schuler, W. Metzger, D. Eglin, M. Alini, M.D. Menger, Three-dimensional spheroids of adipose-derived mesenchymal stem cells are potent initiators of blood vessel formation in porous polyurethane scaffolds, *Acta Biomaterialia* 9(6) (2013) 6876-6884.
- [8] N. Handel, Long-Term Safety and Efficacy of Polyurethane Foam-Covered Breast Implants, *Aesthetic Surgery Journal* 26(3) (2006) 265-274.
- [9] S. Desai, I.M. Thakore, B.D. Sarawade, S. Devi, Effect of polyols and diisocyanates on thermo-mechanical and morphological properties of polyurethanes, *European Polymer Journal* 36(4) (2000) 711-725.
- [10] J.J. Hutchinson, M. McGuckin, Occlusive dressings: A microbiologic and clinical review, *American Journal of Infection Control* 18(4) (1990) 257-268.
- [11] J.R. Hanna, J.A. Giacomelli, A review of wound healing and wound dressing products, *The Journal of Foot and Ankle Surgery* 36(1) (1997) 2-14.
- [12] M.U. Ozkaynak, C. Atalay-Oral, S.B. Tanteekin-Ersolmaz, F.S. Güner, Polyurethane Films for Wound Dressing Applications, *Macromolecular Symposia* 228(1) (2005) 177-184.
- [13] J.E. McBane, S. Sharifpoor, K. Cai, R.S. Labow, J.P. Santerre, Biodegradation and in vivo biocompatibility of a degradable, polar/hydrophobic/ionic polyurethane for tissue engineering applications, *Biomaterials* 32(26) (2011) 6034-6044.
- [14] L.R. Lakshman, K.T. Shalumon, S.V. Nair, R. Jayakumar, S.V. Nair, Preparation of Silver Nanoparticles Incorporated Electrospun Polyurethane Nano-fibrous Mat for Wound Dressing, *Journal of Macromolecular Science, Part A* 47(10) (2010) 1012-1018.
- [15] M. Soto, R.M. Sebastián, J. Marquet, Photochemical Activation of Extremely Weak Nucleophiles: Highly Fluorinated Urethanes and Polyurethanes from Polyfluoro Alcohols, *The Journal of organic chemistry* 79(11) (2014) 5019-5027.
- [16] Y.C. Jung, N.G. Sahoo, J.W. Cho, Polymeric nanocomposites of polyurethane block copolymers and functionalized multi-walled carbon nanotubes as crosslinkers, *Macromolecular Rapid*

Communications 27(2) (2006) 126-131.

[17] R. Srivastava, D. Srinivas, P. Ratnasamy, Syntheses of polycarbonate and polyurethane precursors utilizing CO₂ over highly efficient, solid as-synthesized MCM-41 catalyst, *Tetrahedron letters* 47(25) (2006) 4213-4217.

[18] K.H. Choe, D.S. Lee, W.J. Seo, W.N. Kim, Properties of rigid polyurethane foams with blowing agents and catalysts, *Polymer journal* 36(5) (2004) 368-373.

[19] D.G. Pyun, H.J. Choi, H.S. Yoon, T. Thambi, D.S. Lee, Polyurethane foam containing rhEGF as a dressing material for healing diabetic wounds: Synthesis, characterization, in vitro and in vivo studies, *Colloids and Surfaces B: Biointerfaces* 135 (2015) 699-706.

[20] E.Y. Kim, J.H. Lee, D.J. Lee, Y.H. Lee, J.H. Lee, H.D. Kim, Synthesis and properties of highly hydrophilic waterborne polyurethane-ureas containing various hardener content for waterproof breathable fabrics, *Journal of Applied Polymer Science* 129(4) (2013) 1745-1751.

[21] L. Li, X. Liu, Y. Niu, J. Ye, S. Huang, C. Liu, K. Xu, Synthesis and wound healing of alternating block polyurethanes based on poly (lactic acid)(PLA) and poly (ethylene glycol)(PEG), *Journal of Biomedical Materials Research Part B: Applied Biomaterials* (2016).

[22] W.L.J. Hinrichs, E.J.C.M.P. Lommen, C.R.H. Wildevuur, J. Feijen, Fabrication and characterization of an asymmetric polyurethane membrane for use as a wound dressing, *Journal of Applied Biomaterials* 3(4) (1992) 287-303.

[23] F.-L. Mi, S.-S. Shyu, Y.-B. Wu, S.-T. Lee, J.-Y. Shyong, R.-N. Huang, Fabrication and characterization of a sponge-like asymmetric chitosan membrane as a wound dressing, *Biomaterials* 22(2) (2001) 165-173.

[24] H. Niiyama, Y. Kuroyanagi, Development of novel wound dressing composed of hyaluronic acid and collagen sponge containing epidermal growth factor and vitamin C derivative, *Journal of Artificial Organs* 17(1) (2013) 81-87.

[25] S.E. Noorjahan, T.P. Sastry, An in vivo study of hydrogels based on physiologically clotted fibrin–gelatin composites as wound-dressing materials, *Journal of Biomedical Materials Research Part B: Applied Biomaterials* 71B(2) (2004) 305-312.

[26] Q.-H. Zhao, In vivo cell/polymer interactions and polyurethane biostability, Case Western Reserve University, 1992.

[27] B. Balakrishnan, M. Mohanty, P.R. Umashankar, A. Jayakrishnan, Evaluation of an in situ forming hydrogel wound dressing based on oxidized alginate and gelatin, *Biomaterials* 26(32) (2005) 6335-6342.

[28] K. HaeYong, Y. Joo-hong, L. Kwang-gill, L. Hyun Chul, N. Hee Sam, W. Young Ho, C. Chong Su, Semi-interpenetrating polymer networks composed of silk fibroin and poly(ethylene glycol) for wound dressing, *Biomedical Materials* 3(3) (2008) 034115.

[29] K.A. Wright, K.B. Nadire, P. Busto, R. Tubo, J.M. McPherson, B.M. Wentworth, Alternative delivery of keratinocytes using a polyurethane membrane and the implications for its use in the treatment of full-thickness burn injury, *Burns* 24(1) (1998) 7-17.

- [30] A.R. Unnithan, N.A.M. Barakat, P.B. Tirupathi Pichiah, G. Gnanasekaran, R. Nirmala, Y.-S. Cha, C.-H. Jung, M. El-Newehy, H.Y. Kim, Wound-dressing materials with antibacterial activity from electrospun polyurethane–dextran nanofiber mats containing ciprofloxacin HCl, *Carbohydrate Polymers* 90(4) (2012) 1786-1793.
- [31] Y. Huang, K. He, X. Wang, Rapid prototyping of a hybrid hierarchical polyurethane-cell/hydrogel construct for regenerative medicine, *Materials Science and Engineering: C* 33(6) (2013) 3220-3229.
- [32] J.U. Park, H.D. Jung, E.H. Song, T.H. Choi, H.E. Kim, J. Song, S. Kim, The accelerating effect of chitosan-silica hybrid dressing materials on the early phase of wound healing, *J Biomed Mater Res B Appl Biomater* (2016).
- [33] G. Arcangeli, V. Cupelli, G. Giuliano, Effects of silica on human lung fibroblast in culture, *Science of the total environment* 270(1) (2001) 135-139.
- [34] D. Kudela, S.A. Smith, A. May-Masnou, G.B. Braun, A. Pallaoro, C.K. Nguyen, T.T. Chuong, S. Nownes, R. Allen, N.R. Parker, H.H. Rashidi, J.H. Morrissey, G.D. Stucky, Clotting activity of polyphosphate-functionalized silica nanoparticles, *Angewandte Chemie* 54(13) (2015) 4018-22.
- [35] Y.-C. Ou, Z.-Z. Yu, A. Vidal, J. Donnet, Effects of alkylation of silica filler on rubber reinforcement, *Rubber chemistry and technology* 67(5) (1994) 834-844.
- [36] Z. Pu, J.E. Mark, J.M. Jethmalani, W.T. Ford, Effects of dispersion and aggregation of silica in the reinforcement of poly (methyl acrylate) elastomers, *Chemistry of Materials* 9(11) (1997) 2442-2447.
- [37] S. Sarkawi, W. Kaewsakul, K. Sahakaro, W. Dierkes, J. Noordermeer, A Review on Reinforcement of Natural Rubber by Silica Fillers for Use in Low-Rolling Resistance Tires, *Journal of rubber research* 18 (2016) 203-233.
- [38] Y. Duan, S.C. Jana, B. Lama, M.P. Espe, Reinforcement of silica aerogels using silane-end-capped polyurethanes, *Langmuir* 29(20) (2013) 6156-6165.
- [39] J.W. Cho, S.H. Lee, Influence of silica on shape memory effect and mechanical properties of polyurethane–silica hybrids, *European Polymer Journal* 40(7) (2004) 1343-1348.
- [40] T.S. Jang, E.J. Lee, J.H. Jo, J.M. Jeon, M.Y. Kim, H.E. Kim, Y.H. Koh, Fibrous membrane of nano-hybrid poly-L-lactic acid/silica xerogel for guided bone regeneration, *Journal of Biomedical Materials Research Part B: Applied Biomaterials* 100(2) (2012) 321-330.
- [41] D.H. Keast, C.K. Bowering, A.W. Evans, G.L. Mackean, C. Burrows, L. D'Souza, Contents, *Wound Repair and Regeneration* 12 (2004) s1-s17.
- [42] A.H. Fischer, K.A. Jacobson, J. Rose, R. Zeller, Hematoxylin and eosin staining of tissue and cell sections, *Cold Spring Harbor Protocols* 2008(5) (2008) pdb. prot4986.
- [43] W.N. O'connor, S. Valle, A combination Verhoeffs elastic and Masson's trichrome stain for routine histology, *Stain Technology* (2009).
- [44] P. Prentø, Van Gieson's picrofuchsin. The staining mechanisms for collagen and cytoplasm, and an examination of the dye diffusion rate model of differential staining, *Histochemistry* 99(2) (1993)

163-174.

- [45] M. Thirumal, D. Khastgir, N.K. Singha, B. Manjunath, Y. Naik, Effect of foam density on the properties of water blown rigid polyurethane foam, *Journal of applied polymer science* 108(3) (2008) 1810-1817.
- [46] Y. Xia, R.C. Larock, Preparation and properties of aqueous castor oil-based polyurethane-silica nanocomposite dispersions through a sol-gel process, *Macromol Rapid Commun* 32(17) (2011) 1331-7.
- [47] M. Kobayashi, F. Juillerat, P. Galletto, P. Bowen, M. Borkovec, Aggregation and charging of colloidal silica particles: effect of particle size, *Langmuir* 21(13) (2005) 5761-5769.
- [48] S.H. Jun, E.J. Lee, S.W. Yook, H.E. Kim, H.W. Kim, Y.H. Koh, A bioactive coating of a silica xerogel/chitosan hybrid on titanium by a room temperature sol-gel process, *Acta Biomater* 6(1) (2010) 302-7.
- [49] M.-H. Kang, T.-S. Jang, H.-D. Jung, S.-M. Kim, H.-E. Kim, Y.-H. Koh, J. Song, Poly (ether imide)-silica hybrid coatings for tunable corrosion behavior and improved biocompatibility of magnesium implants, *Biomedical Materials* 11(3) (2016) 035003.
- [50] T.A. Khan, K.K. Peh, H.S. Ch'ng, Mechanical, bioadhesive strength and biological evaluations of chitosan films for wound dressing, *J. Pharm. Pharmaceut. Sci* 3(3) (2000) 303-311.
- [51] P. Agache, C. Monneur, J. Leveque, J. De Rigal, Mechanical properties and Young's modulus of human skin in vivo, *Archives of dermatological research* 269(3) (1980) 221-232.
- [52] L. Bistričić, G. Baranović, M. Leskovac, E.G. Bajsić, Hydrogen Bonding in Polyurethane-Silica Nanocomposites, *Macromolecular Symposia*, Wiley Online Library, 2011, pp. 126-131.
- [53] Y. Tien, K. Wei, High-tensile-property layered silicates/polyurethane nanocomposites by using reactive silicates as pseudo chain extenders, *Macromolecules* 34(26) (2001) 9045-9052.
- [54] M. Kokabi, M. Sirousazar, Z.M. Hassan, PVA-clay nanocomposite hydrogels for wound dressing, *European Polymer Journal* 43(3) (2007) 773-781.
- [55] L. Wang, E. Khor, A. Wee, L.Y. Lim, Chitosan-alginate PEC membrane as a wound dressing: Assessment of incisional wound healing, *J Biomed Mater Res* 63(5) (2002) 610-8.
- [56] J.H. Sung, M.R. Hwang, J.O. Kim, J.H. Lee, Y.I. Kim, J.H. Kim, S.W. Chang, S.G. Jin, J.A. Kim, W.S. Lyoo, S.S. Han, S.K. Ku, C.S. Yong, H.G. Choi, Gel characterisation and in vivo evaluation of minocycline-loaded wound dressing with enhanced wound healing using polyvinyl alcohol and chitosan, *Int J Pharm* 392(1-2) (2010) 232-40.
- [57] S.M. Lee, I.K. Park, Y.S. Kim, H.J. Kim, H. Moon, S. Mueller, Y.-I. Jeong, Physical, morphological, and wound healing properties of a polyurethane foam-film dressing, *Biomaterials Research* 20(1) (2016) 1.
- [58] Y. Takemoto, T.-S. Li, M. Kubo, M. Ohshima, H. Kurazumi, K. Ueda, T. Enoki, T. Murata, K. Hamano, The mobilization and recruitment of c-kit⁺ cells contribute to wound healing after surgery, *PloS one* 7(11) (2012) e48052.
- [59] L. Hu, J. Wang, X. Zhou, Z. Xiong, J. Zhao, R. Yu, F. Huang, H. Zhang, L. Chen, Exosomes

derived from human adipose mesenchymal stem cells accelerates cutaneous wound healing via optimizing the characteristics of fibroblasts, *Scientific Reports* 6 (2016).

[60] L.I. Moura, A.M. Dias, E. Suesca, S. Casadiegos, E.C. Leal, M.R. Fontanilla, L. Carvalho, H.C. de Sousa, E. Carvalho, Neurotensin-loaded collagen dressings reduce inflammation and improve wound healing in diabetic mice, *Biochimica et Biophysica Acta (BBA)-Molecular Basis of Disease* 1842(1) (2014) 32-43.

[61] L. van Rijswijk, J. Beitz, The traditions and terminology of wound dressings: food for thought, *Journal of Wound Ostomy & Continence Nursing* 25(3) (1998) 116-122.

[62] J. Uitto, Connective tissue biochemistry of the aging dermis. Age-related alterations in collagen and elastin, *Dermatologic clinics* 4(3) (1986) 433-446.

[63] S.R. Beanes, C. Dang, C. Soo, K. Ting, Skin repair and scar formation: the central role of TGF- β , *Expert Reviews in Molecular Medicine* 5(08) (2003) 1-22.

[64] L.L. Hench, I.D. Xynos, J.M. Polak, Bioactive glasses for in situ tissue regeneration, *Journal of Biomaterials Science, Polymer Edition* 15(4) (2004) 543-562.

[65] L. Cuttle, M. Kempf, G.E. Phillips, J. Mill, M.T. Hayes, J.F. Fraser, X.-Q. Wang, R.M. Kimble, A porcine deep dermal partial thickness burn model with hypertrophic scarring, *Burns* 32(7) (2006) 806-820.

[66] W. Xiaohui, W. Jie, L. Xun, L. Yang, C. Fangping, Z. Yanglan, L. Changsheng, Chemical characteristics and hemostatic performances of ordered mesoporous calcium-doped silica xerogels, *Biomedical Materials* 5(3) (2010) 035006.

[67] N. Handel, T. Cordray, J. Gutierrez, J.A. Jensen, A long-term study of outcomes, complications, and patient satisfaction with breast implants, *Plastic and reconstructive surgery* 117(3) (2006) 757-767.

[68] A.M. Zollner, A. Buganza Tepole, A.K. Gosain, E. Kuhl, Growing skin: tissue expansion in pediatric forehead reconstruction, *Biomech Model Mechanobiol* 11(6) (2012) 855-67.

[69] Y. Kang, J. Yang, S. Khan, L. Anissian, G.A. Ameer, A new biodegradable polyester elastomer for cartilage tissue engineering, *J Biomed Mater Res A* 77(2) (2006) 331-9.

[70] J.W. Boretos, W.S. Pierce, Segmented polyurethane: a new elastomer for biomedical applications, *Science* 158(3807) (1967) 1481-1482.

[71] K. Benhamou, H. Kaddami, A. Magnin, A. Dufresne, A. Ahmad, Bio-based polyurethane reinforced with cellulose nanofibers: a comprehensive investigation on the effect of interface, *Carbohydr Polym* 122 (2015) 202-11.

[72] J. Frame, D. Kamel, M. Olivan, H. Cintra, The In Vivo Pericapsular Tissue Response to Modern Polyurethane Breast Implants, *Aesthetic plastic surgery* 39(5) (2015) 713-723.

[73] K.C. Hung, C.S. Tseng, L.G. Dai, S.H. Hsu, Water-based polyurethane 3D printed scaffolds with controlled release function for customized cartilage tissue engineering, *Biomaterials* 83 (2016) 156-68.

[74] G.J. Ritfeld, B.M. Rauck, T.L. Novosat, D. Park, P. Patel, R.A. Roos, Y. Wang, M. Oudega, The

effect of a polyurethane-based reverse thermal gel on bone marrow stromal cell transplant survival and spinal cord repair, *Biomaterials* 35(6) (2014) 1924-31.

[75] K. Sariibrahimoglu, W. Yang, S.C. Leeuwenburgh, F. Yang, J.G. Wolke, Y. Zuo, Y. Li, J.A. Jansen, Development of porous polyurethane/strontium-substituted hydroxyapatite composites for bone regeneration, *J Biomed Mater Res A* 103(6) (2015) 1930-9.

[76] G. Ciobanu, S. Ilisei, C. Luca, Hydroxyapatite-silver nanoparticles coatings on porous polyurethane scaffold, *Mater Sci Eng C Mater Biol Appl* 35 (2014) 36-42.

[77] S. Zhang, K. Xu, L. Ge, M.A. Darabi, F. Xie, S. Derakhshanfar, Y. Liu, M.M.Q. Xing, H. Wei, A novel nano-silver coated and hydrogel-impregnated polyurethane nanofibrous mesh for ventral hernia repair, *RSC Adv.* 6(93) (2016) 90571-90578.

[78] D. Chen, C. Tang, K. Chan, C. Tsui, P. Yu, M. Leung, P. Uskokovic, Dynamic mechanical properties and in vitro bioactivity of PHBHV/HA nanocomposite, *Composites Science and Technology* 67(7-8) (2007) 1617-1626.

[79] M. Sadat-Shojai, M.T. Khorasani, E. Dinpanah-Khoshdargi, A. Jamshidi, Synthesis methods for nanosized hydroxyapatite with diverse structures, *Acta Biomater* 9(8) (2013) 7591-621.

[80] A. Chetty, T. Steynberg, S. Moolman, R. Nilen, A. Joubert, W. Richter, Hydroxyapatite-coated polyurethane for auricular cartilage replacement: an in vitro study, *J Biomed Mater Res A* 84(2) (2008) 475-82.

[81] Z. Dong, Y. Li, Q. Zou, Degradation and biocompatibility of porous nano-hydroxyapatite/polyurethane composite scaffold for bone tissue engineering, *Applied Surface Science* 255(12) (2009) 6087-6091.

[82] J. Li, B.A. Baker, X. Mou, N. Ren, J. Qiu, R.I. Boughton, H. Liu, Biopolymer/Calcium phosphate scaffolds for bone tissue engineering, *Adv Healthc Mater* 3(4) (2014) 469-84.

[83] R.J. Kane, H.E. Weiss-Bilka, M.J. Meagher, Y. Liu, J.A. Gargac, G.L. Niebur, D.R. Wagner, R.K. Roeder, Hydroxyapatite reinforced collagen scaffolds with improved architecture and mechanical properties, *Acta Biomater* 17 (2015) 16-25.

[84] J. Ryu, S.H. Ku, H. Lee, C.B. Park, Mussel-Inspired Polydopamine Coating as a Universal Route to Hydroxyapatite Crystallization, *Advanced Functional Materials* 20(13) (2010) 2132-2139.

[85] H. Yuk, T. Zhang, G.A. Parada, X. Liu, X. Zhao, Skin-inspired hydrogel-elastomer hybrids with robust interfaces and functional microstructures, *Nat Commun* 7 (2016) 12028.

[86] H.J. Kim, U.J. Kim, H.S. Kim, C. Li, M. Wada, G.G. Leisk, D.L. Kaplan, Bone tissue engineering with premineralized silk scaffolds, *Bone* 42(6) (2008) 1226-34.

[87] W. Li, A.J. Ryan, I.K. Meier, Effect of chain extenders on the morphology development in flexible polyurethane foam, *Macromolecules* 35(16) (2002) 6306-6312.

[88] A.C. Tas, S.B. Bhaduri, Rapid coating of Ti6Al4V at room temperature with a calcium phosphate solution similar to 10× simulated body fluid, *Journal of Materials Research* 19(09) (2011) 2742-2749.

[89] B.L. Phillips, Z. Zhang, L. Kubista, S. Frisia, A. Borsato, NMR spectroscopic study of organic

- phosphate esters coprecipitated with calcite, *Geochimica et Cosmochimica Acta* 183 (2016) 46-62.
- [90] M.E. Lynge, R. van der Westen, A. Postma, B. Städler, Polydopamine—a nature-inspired polymer coating for biomedical science, *Nanoscale* 3(12) (2011) 4916-4928.
- [91] H. Deka, N. Karak, Bio-based hyperbranched polyurethanes for surface coating applications, *Progress in Organic Coatings* 66(3) (2009) 192-198.
- [92] H. Lee, J. Rho, P.B. Messersmith, Facile Conjugation of Biomolecules onto Surfaces via Mussel Adhesive Protein Inspired Coatings, *Adv Mater* 21(4) (2009) 431-434.
- [93] S.R. Paital, N.B. Dahotre, Calcium phosphate coatings for bio-implant applications: Materials, performance factors, and methodologies, *Materials Science and Engineering: R: Reports* 66(1-3) (2009) 1-70.
- [94] E.-H. Song, K.-I. Cho, H.-E. Kim, S.-H. Jeong, Biomimetic Coating of Hydroxyapatite on Glycerol Phosphate-Conjugated Polyurethane via Mineralization, *ACS Omega* 2(3) (2017) 981-987.
- [95] D.V. Luquetti, C.L. Heike, A.V. Hing, M.L. Cunningham, T.C. Cox, Microtia: epidemiology and genetics, *American Journal of Medical Genetics Part A* 158(1) (2012) 124-139.
- [96] B. Brent, Technical advances in ear reconstruction with autogenous rib cartilage grafts, *Personal experience with 1200 cases* 1999 (1999) 104.
- [97] T. Wellisz, Reconstruction of the burned external ear using a Medpor porous polyethylene pivoting helix framework, *Plastic and reconstructive surgery* 91(5) (1993) 811-818.
- [98] T. Wellisz, Clinical experience with the Medpor porous polyethylene implant, *Aesthetic plastic surgery* 17(4) (1993) 339-344.
- [99] L. Prantl, S. Schreml, S. Fichtner-Feigl, N. Pöppl, M. Eisenmann-Klein, H. Schwarze, B. Führtmeier, Clinical and morphological conditions in capsular contracture formed around silicone breast implants, *Plastic and reconstructive surgery* 120(1) (2007) 275-284.
- [100] S. Barr, E. Hill, A. Bayat, Current implant surface technology: an examination of their nanostructure and their influence on fibroblast alignment and biocompatibility, *Eplasty* 9 (2009).
- [101] N.-x. Cheng, Y.-l. Wang, J.-h. Wang, X.-m. Zhang, H. Zhong, Complications of breast augmentation with injected hydrophilic polyacrylamide gel, *Aesthetic plastic surgery* 26(5) (2002) 375-382.
- [102] A.J. Fox, A. Bedi, S.A. Rodeo, The basic science of human knee menisci: structure, composition, and function, *Sports Health* 4(4) (2012) 340-51.
- [103] K. Messner, J. Gao, The menisci of the knee joint. Anatomical and functional characteristics, and a rationale for clinical treatment, *Journal of anatomy* 193(2) (1998) 161-178.
- [104] E. Pena, B. Calvo, M.A. Martinez, M. Doblare, A three-dimensional finite element analysis of the combined behavior of ligaments and menisci in the healthy human knee joint, *J Biomech* 39(9) (2006) 1686-701.
- [105] J.G. Kim, Y.S. Lee, T.S. Bae, J.K. Ha, D.H. Lee, Y.J. Kim, H.J. Ra, Tibiofemoral contact mechanics following posterior root of medial meniscus tear, repair, meniscectomy, and allograft transplantation, *Knee Surg Sports Traumatol Arthrosc* 21(9) (2013) 2121-5.

- [106] M. Kobayashi, J. Toguchida, M. Oka, Preliminary study of polyvinyl alcohol-hydrogel (PVA-H) artificial meniscus, *Biomaterials* 24(4) (2003) 639-647.
- [107] M.E. Baratz, F.H. Fu, R. Mengato, Meniscal tears: The effect of meniscectomy and of repair on intraarticular contact areas and stress in the human knee A preliminary report, *The American Journal of Sports Medicine* 14(4) (1986) 270-275.
- [108] K.B. Hare, L.S. Lohmander, R. Christensen, E.M. Roos, Arthroscopic partial meniscectomy in middle-aged patients with mild or no knee osteoarthritis: a protocol for a double-blind, randomized sham-controlled multi-centre trial, *BMC musculoskeletal disorders* 14(1) (2013) 71.
- [109] W. Maletius, K. Messner, The effect of partial meniscectomy on the long-term prognosis of knees with localized, severe chondral damage: A twelve-to fifteen-year followup, *The American journal of sports medicine* 24(3) (1996) 258-262.
- [110] R. Sihvonen, M. Englund, A. Turkiewicz, T.L. Jarvinen, G. Finnish Degenerative Meniscal Lesion Study, Mechanical Symptoms and Arthroscopic Partial Meniscectomy in Patients With Degenerative Meniscus Tear: A Secondary Analysis of a Randomized Trial, *Ann Intern Med* 164(7) (2016) 449-55.
- [111] B. Bai, H. Shun, Z.X. Yin, Z.W. Liao, N. Chen, Changes of contact pressure and area in patellofemoral joint after different meniscectomies, *Int Orthop* 36(5) (2012) 987-91.
- [112] A. Heijink, A.H. Gomoll, H. Madry, M. Drobnic, G. Filardo, J. Espregueira-Mendes, C.N. Van Dijk, Biomechanical considerations in the pathogenesis of osteoarthritis of the knee, *Knee Surg Sports Traumatol Arthrosc* 20(3) (2012) 423-35.
- [113] J.Y. Bae, K.S. Park, J.K. Seon, D.S. Kwak, I. Jeon, E.K. Song, Biomechanical analysis of the effects of medial meniscectomy on degenerative osteoarthritis, *Med Biol Eng Comput* 50(1) (2012) 53-60.
- [114] M. Englund, F.W. Roemer, D. Hayashi, M.D. Crema, A. Guermazi, Meniscus pathology, osteoarthritis and the treatment controversy, *Nat Rev Rheumatol* 8(7) (2012) 412-9.
- [115] T.G. Tienen, R.G. Heijkants, J.H. de Groot, A.J. Pennings, A.J. Schouten, R.P. Veth, P. Buma, Replacement of the knee meniscus by a porous polymer implant: a study in dogs, *Am J Sports Med* 34(1) (2006) 64-71.
- [116] A.C. Vrancken, P. Buma, T.G. van Tienen, Synthetic meniscus replacement: a review, *Int Orthop* 37(2) (2013) 291-9.
- [117] M.W. Beatty, A.K. Ojha, J.L. Cook, L.R. Alberts, G.K. Mahanna, L.R. Iwasaki, J.C. Nickel, Small intestinal submucosa versus salt-extracted polyglycolic acid-poly-L-lactic acid: a comparison of neocartilage formed in two scaffold materials, *Tissue engineering* 8(6) (2002) 955-968.
- [118] R.G. Heijkants, R. Van Calck, J. De Groot, A. Pennings, A. Schouten, T. Van Tienen, N. Ramrattan, P. Buma, R.P. Veth, Design, synthesis and properties of a degradable polyurethane scaffold for meniscus regeneration, *Journal of Materials Science: Materials in Medicine* 15(4) (2004) 423-427.
- [119] S. Ravindran, M. Kotecha, C.-C. Huang, A. Ye, P. Pothirajan, Z. Yin, R. Magin, A. George,

Biological and MRI Characterization of Biomimetic ECM Scaffolds for Cartilage Tissue Regeneration, *Biomaterials* 71 (2015) 58-70.

[120] B.D. Smith, D.A. Grande, The current state of scaffolds for musculoskeletal regenerative applications, *Nat Rev Rheumatol* 11(4) (2015) 213-222.

[121] B.M. Baker, R.L. Mauck, The effect of nanofiber alignment on the maturation of engineered meniscus constructs, *Biomaterials* 28(11) (2007) 1967-1977.

[122] K.R. Stone, W.G. Rodkey, R. Webber, L. McKinney, J.R. Steadman, Meniscal regeneration with copolymeric collagen scaffolds: In vitro and in vivo studies evaluated clinically, histologically, and biochemically, *The American journal of sports medicine* 20(2) (1992) 104-111.

[123] E. Linder-Ganz, J.J. Elsner, A. Danino, F. Guilak, A. Shterling, A novel quantitative approach for evaluating contact mechanics of meniscal replacements, *J Biomech Eng* 132(2) (2010) 024501.

[124] M. Shemesh, R. Asher, E. Zylberberg, F. Guilak, E. Linder-Ganz, J.J. Elsner, Viscoelastic properties of a synthetic meniscus implant, *J Mech Behav Biomed Mater* 29 (2014) 42-55.

[125] K. Messner, L.S. Lohmander, J. Gillquist, Cartilage mechanics and morphology, synovitis and proteoglycan fragments in rabbit joint fluid after prosthetic meniscal substitution, *Biomaterials* 14(3) (1993) 163-168.

[126] P. Buma, N. Ramrattan, T.G. van Tienen, R.P. Veth, Tissue engineering of the meniscus, *Biomaterials* 25(9) (2004) 1523-1532.

[127] R.H. Brophy, J. Cottrell, S.A. Rodeo, T.M. Wright, R.F. Warren, S.A. Maher, Implantation of a synthetic meniscal scaffold improves joint contact mechanics in a partial meniscectomy cadaver model, *Journal of Biomedical Materials Research Part A* 92(3) (2010) 1154-1161.

[128] J.C. Monllau, P.E. Gelber, F. Abat, X. Pelfort, R. Abad, P. Hinarejos, M. Tey, Outcome after partial medial meniscus substitution with the collagen meniscal implant at a minimum of 10 years' follow-up, *Arthroscopy: The Journal of Arthroscopic & Related Surgery* 27(7) (2011) 933-943.

[129] S. Zaffagnini, G. Giordano, A. Vascellari, D. Bruni, M.P. Neri, F. Iacono, E. Kon, M.L. Presti, M. Marcacci, Arthroscopic collagen meniscus implant results at 6 to 8 years follow up, *Knee Surg Sports Traumatol Arthrosc* 15(2) (2007) 175-83.

[130] B.-S. Lee, J.-W. Chung, J.-M. Kim, W.-J. Cho, K.-A. Kim, S.-I. Bin, Morphologic changes in fresh-frozen meniscus allografts over 1 year a prospective magnetic resonance imaging study on the width and thickness of transplants, *The American journal of sports medicine* 40(6) (2012) 1384-1391.

[131] R. Verdonk, P. Verdonk, E. Heinrichs, Polyurethane meniscus implant: technique, *The meniscus*, Springer2010, pp. 389-394.

[132] R. Verdonk, P. Verdonk, W. Huysse, R. Forsyth, E.-L. Heinrichs, Tissue ingrowth after implantation of a novel, biodegradable polyurethane scaffold for treatment of partial meniscal lesions, *The American journal of sports medicine* 39(4) (2011) 774-782.

[133] J. De Groot, R. De Vrijer, A. Pennings, J. Klompmaker, R. Veth, H. Jansen, Use of porous polyurethanes for meniscal reconstruction and meniscal prostheses, *Biomaterials* 17(2) (1996) 163-

173.

- [134] V. Chiono, P. Mozetic, M. Boffito, S. Sartori, E. Gioffredi, A. Silvestri, A. Rainer, S.M. Giannitelli, M. Trombetta, D. Nurzynska, F. Di Meglio, C. Castaldo, R. Miraglia, S. Montagnani, G. Ciardelli, Polyurethane-based scaffolds for myocardial tissue engineering, *Interface Focus* 4(1) (2014).
- [135] E.M. Rivera-Muñoz, Hydroxyapatite-Based Materials: Synthesis and Characterization, in: R. Fazel-Rezai (Ed.), *Biomedical Engineering - Frontiers and Challenges*, InTech, Rijeka, 2011, p. Ch. 04.
- [136] S. Mortazavian, A. Fatemi, Effects of fiber orientation and anisotropy on tensile strength and elastic modulus of short fiber reinforced polymer composites, *Composites Part B: Engineering* 72(Supplement C) (2015) 116-129.
- [137] W. Han, G. Zhao, X. Zhang, S. Zhou, P. Wang, Y. An, B. Xu, Graphene oxide grafted carbon fiber reinforced siliconborocarbonitride ceramics with enhanced thermal stability, *Carbon* 95(Supplement C) (2015) 157-165.
- [138] P.K. Vallittu, High-aspect ratio fillers: Fiber-reinforced composites and their anisotropic properties, *Dental Materials* 31(1) (2015) 1-7.
- [139] W. Hufenbach, M. Gude, S. Geller, Cellular Fiber-Reinforced Polyurethane Composites with Sensory Properties, *Advanced Engineering Materials* 16(3) (2014) 272-275.
- [140] B. Arash, H.S. Park, T. Rabczuk, Mechanical properties of carbon nanotube reinforced polymer nanocomposites: A coarse-grained model, *Composites Part B: Engineering* 80(Supplement C) (2015) 92-100.
- [141] Z.-G. Yang, B. Zhao, S.-L. Qin, Z.-F. Hu, Z.-K. Jin, J.-H. Wang, Study on the mechanical properties of hybrid reinforced rigid polyurethane composite foam, *Journal of Applied Polymer Science* 92(3) (2004) 1493-1500.
- [142] F.M. Orr, L.E. Scriven, A.P. Rivas, Pendular rings between solids: meniscus properties and capillary force, *Journal of Fluid Mechanics* 67(4) (2006) 723-742.
- [143] J.J. Rongen, T.G. van Tienen, B. van Bochove, D.W. Grijpma, P. Buma, Biomaterials in search of a meniscus substitute, *Biomaterials* 35(11) (2014) 3527-3540.
- [144] B. Li, T. Yoshii, A.E. Hafeman, J.S. Nyman, J.C. Wenke, S.A. Guelcher, The effects of rhBMP-2 released from biodegradable polyurethane/microsphere composite scaffolds on new bone formation in rat femora, *Biomaterials* 30(35) (2009) 6768-6779.
- [145] W.N. Sivak, I.F. Pollack, S. Petoud, W.C. Zamboni, J. Zhang, E.J. Beckman, Catalyst-dependent drug loading of LDI-glycerol polyurethane foams leads to differing controlled release profiles, *Acta Biomaterialia* 4(5) (2008) 1263-1274.
- [146] K. Sreenivasan, Surface-Imprinted Polyurethane Having Affinity Sites for Ampicillin, *Macromolecular bioscience* 5(3) (2005) 187-191.
- [147] L. Hou, Y. Peck, X. Wang, D. Wang, Surface patterning and modification of polyurethane biomaterials using silsesquioxane-gelatin additives for improved endothelial affinity, *Science China Chemistry* 57(4) (2014) 596-604.
- [148] H.S. Yoo, T.G. Kim, T.G. Park, Surface-functionalized electrospun nanofibers for tissue

engineering and drug delivery, *Advanced Drug Delivery Reviews* 61(12) (2009) 1033-1042.

[149] J. Fang, S.-H. Ye, J. Wang, T. Zhao, X. Mo, W.R. Wagner, Thiol click modification of cyclic disulfide containing biodegradable polyurethane urea elastomers, *Biomacromolecules* 16(5) (2015) 1622-1633.

[150] B.S. Lele, H. Murata, K. Matyjaszewski, A.J. Russell, Synthesis of uniform protein– polymer conjugates, *Biomacromolecules* 6(6) (2005) 3380-3387.

[151] M.A. Gauthier, H.-A. Klok, Peptide/protein–polymer conjugates: synthetic strategies and design concepts, *Chemical Communications* (23) (2008) 2591-2611.

[152] J. Collins, J. Tanaka, P. Wilson, K. Kempe, T.P. Davis, M.P. McIntosh, M.R. Whittaker, D.M. Haddleton, In situ conjugation of dithiophenol maleimide polymers and oxytocin for stable and reversible polymer–peptide conjugates, *Bioconjugate chemistry* 26(4) (2015) 633-638.

[153] I. Cobo, M. Li, B.S. Sumerlin, S. Perrier, Smart hybrid materials by conjugation of responsive polymers to biomacromolecules, *Nature materials* 14(2) (2015) 143.

[154] P. Wilson, Synthesis and Applications of Protein/Peptide-Polymer Conjugates, *Macromolecular Chemistry and Physics* 218(9) (2017).

[155] M.H. Lee, J.L. Sessler, J.S. Kim, Disulfide-based multifunctional conjugates for targeted theranostic drug delivery, *Accounts of chemical research* 48(11) (2015) 2935-2946.

[156] G. Saito, J.A. Swanson, K.-D. Lee, Drug delivery strategy utilizing conjugation via reversible disulfide linkages: role and site of cellular reducing activities, *Advanced drug delivery reviews* 55(2) (2003) 199-215.

[157] N.J. Darby, R.B. Freedman, T.E. Creighton, Dissecting the mechanism of protein disulfide isomerase: catalysis of disulfide bond formation in a model peptide, *Biochemistry* 33(25) (1994) 7937-7947.

[158] D.J. Morré, D.M. Morré, Differential response of the NADH oxidase of plasma membranes of rat liver and hepatoma and HeLa cells to thiol reagents, *Journal of bioenergetics and biomembranes* 27(1) (1995) 137-144.

[159] M.J. Fernández, M.D. Fernández, M. Cobos, Synthesis, characterization and properties of telechelic hybrid biodegradable polymers containing polyhedral oligomeric silsesquioxane (POSS), *RSC Advances* 4(41) (2014) 21435-21449.

[160] A.R. Hernández, O.C. Contreras, J.C. Acevedo, L.G.N. Moreno, Poly (ϵ -caprolactone) degradation under acidic and alkaline conditions, *American Journal of Polymer Science* 3(4) (2013) 70-75.

[161] S. Xiaocheng, Y. Hao, W. Jianzu, M. Rujiang, A. Yingli, S. Linqi, Dual-responsive micelles based on boronic acid-modified polymer, *CHEMICAL JOURNAL OF CHINESE UNIVERSITIES-CHINESE* 35(7) (2014) 1570-1578.

[162] C. Wagner, A. Naumkin, A. Kraut-Vass, J. Allison, C. Powell, J. Rumble Jr, NIST standard reference database 20, Version 3.4 (Web version), National Institute of Standards and Technology: Gaithersburg, MD 20899 (2003).

- [163] G. Beamson, D. Briggs, High Resolution XPS of Organic Polymers. The Scienta ESCA300 Database. Chichester, New York, (1992).
- [164] S. Xu, K. Lin, Z. Wang, J. Chang, L. Wang, J. Lu, C. Ning, Reconstruction of calvarial defect of rabbits using porous calcium silicate bioactive ceramics, *Biomaterials* 29(17) (2008) 2588-2596.
- [165] J.-Y. Park, C. Yang, I.-H. Jung, H.-C. Lim, J.-S. Lee, U.-W. Jung, Y.-K. Seo, J.-K. Park, S.-H. Choi, Regeneration of rabbit calvarial defects using cells-implanted nano-hydroxyapatite coated silk scaffolds, *Biomaterials research* 19(1) (2015) 7.

한글 초록

폴리우레탄 스캐폴드 혹은 지지체는 의료용 생체응용 분야 중 특히 조직공학측면에서 많은 장점을 지니고 있다. 폴리우레탄은 간단한 발포공정을 통해 기공률이 높은 다공체로 제작될 수 있으며, 체내모방환경에서 화학적으로 안정하고, 분자구조를 선택적으로 변화시켜 필요한 기능성을 추가하기 쉬운 물질이기 때문이다. 하지만, 조직의 재생을 유도하고, 치료기작을 향상시키기 위한 생체활성도가 낮아 단일 재료로 사용되기에는 한계점이 존재한다. 그래서 우수한 재료적 성질을 갖는 우레탄의 장점을 더욱 강조하기 위해 한계점인 생체특성을 향상시키려는 연구가 많이 진행되고 있다. 본 연구에서는 3 종의 새로운 폴리우레탄 복합체 시스템을 제안하여 이를 극복하였다; 1) 솔/젤 변환과정을 통해 생체 특성이 좋은 실리카를 폴리우레탄 발포과정에 도입하는 방법, 2) 생체활성도가 높은 하이드록시아파타이트를 폴리우레탄에 고르게 석출시키는 기술 (우레탄의 분자구조단계에서 포스페이트 작용기를 도입), 3) 가역적으로 생분해 가능한 이황화결합을 도입하여 약물전달의 효율성과 안정성을 향상시키는 기술. 본 연구에서는 위 각각의 기술을 도입한 폴리우레탄 복합체의 향상된 생체 특성을 *in vitro* 그리고 *in vivo* 연구 등을 통해 면밀히 분석하였다.

폴리우레탄 기반의 드레싱 품은 우수한 흡수성, 우수한 기계적 특성 및 뛰어난 경제성 때문에 널리 사용되었다. 그러나, 폴리우레탄의 낮은 생체 활성도 및 수동적인 치유 능력은 복잡한 상처 치유 경우에 사용되기에 한계점이 존재한다. 본 연구에서는 폴리우레탄 창상재료의 치유력을 향상시키기 위해 생체활성도가 높은 실리카 나노 입자 제작방식인 솔/젤 공정을 발포 반응에 동시에 도입하여 복합체를 제작하였다. 그 결과 5~60nm 크기의 비정질 실리카 나노 입자가 폴리우레탄에 잘 분산되었다. 실리카는 폴리우레탄의 기계적 성능을 향상시켰으며 폴리우레탄의 우수한 수분 흡수력과 투습도는 적절히 유지하였다. 10wt% 함량의 폴리우레탄 실리카 복합체의 경우 실리카가 점진적으로 용해되어 14 일 동안 생리 조건 하에 지속적으로 방출되었다. 시험관내 세포 부착 및 증식 시험에서는 PU-Si 복합체의 생체 적합성이 현저히 향상되었음을 확인하였다. 더욱 중요하게는, 창상재료로서 PU-Si 의 치유 능력은 동물 실험을 통해 면밀히 입증되었다. 시험에서 PU-Si 품으로 처리한 상처는 새로 형성된 상피층으로 완전히 덮였으며 진피의 콜라겐 및 엘라스틴 섬유 재생 촉진과 함께 빠른 상처치료에 긍정적인 가능성을 보였다.

또한, 폴리우레탄에 포스페이트 작용기를 도입하여 고분자 표면에서 생체적합성이 뛰어난 하이드록시아파타이트(HA)가 고르게 석출될 수 있도록 연구를 진행하였다. 글리세롤포스페이트는 우레탄의 아이소시아네이트 기와 성공적으로 반응하였다. 도입된 포스페이트 기는 인산 칼슘 이온이 풍부한 조건 하에서 HA 의 핵 생성을 가속화시켰다. 또한 전기적인력이 작용하는 HA 와 PU 간의 견고한 계면은 복합체의 안정성을 향상 시켰다. 생체 활성도가 높은 HA 는 섬유아세포와 골아세포의 부착 및 증식을 향상시켰다. 생체 특성이 향상된 복합체는 두 종류의 연골대체용 지지체 (무릎 반월연골, 귀 연골)로서 응용될 수 있었다. 하지만 연골 대체용 지지체로 사용되기 위해서는 다공체가 갖는 물성보다 더 많은 기계적 물성의 향상이 이루어져야 했다. 기공률을 조절하기 위해 열과 압력을 가하는 고밀도화 공정이 진행되었다. 고밀도의 복합체 즉 PU-gp-HA (PUH)의 기공률은 압축 압력 (5, 1000, 2000 kgf)을 조절함으로써 쉽게 조절되었다 (30 %, 10 %, 7 %). 고밀도화 된 PUH 의 강도 및 탄성률은 고분자 내부에 HA 가 충전제로서 작용하여 다공성 PUH 의 강도 및 탄성 계수보다 현저히 높게 측정됐다. 또한 연골대체용 지지체로서 체내에 사용되었을 때 면역반응의 일종인 capsular contracture 의 정도를 동물실험을 통해 분석 및 평가 하였다. HA 는 이물반응을 급격히 완화시키고 임플란트의 생체 적합성을 향상시켰고, 두께가 얇고 콜라겐 밀도가 낮은 캡슐을 형성하는데 도움을 주었다.

마지막으로 타이올기를 첨가한 생분해성 폴리우레탄 (TG-DPU)은 functionalized chain extender 로 채택 된 thioglycerol 과 one-pot 반응을 사용하여 합성되었다. 양성자 핵 자기공명 분광학을 이용한 TG-DPU 의 화학적 구조를 분석한 결과, 디자인한 바와 같은 화학구조로 성공적으로 합성됨을 확인하였다. TG-DPU 의 타이올을 이용하여 BMP-2 와 가역적인 이황화결합을 형성하기 위해 산화조건하에 약물을 담지하였다. TG-DPU 와 BMP-2 간의 상호 작용은 X 선 광전자분광학 분석을 사용하여 조사되었다. 이황화 (S-S) 결합의 출현은 중합체/성장인자 접합 시스템의 성공적인 개발을 의미했다. 공유 결합을 통해 형성된 약물전달 시스템은 체외 방출 시험에서 장기적이고 지속적인 방출 성능을 갖는 약물 전달 효능을 제시하였다. TG-DPU 에 의해 전달 된 약물의 효과는 또한 골아세포 및 생체 내 골 재생 시험에서 면밀히 증명되었다.

Curriculum Vitae (CV)

Eunho Song

zinzan@snu.ac.kr

EDUCATION

Seoul National University, Seoul, Korea

Integrated M.S./Ph.D. in Materials Science and Engineering

Advisor: Professor Hyoun-ee Kim

Thesis: Advanced polyurethane based composites for biomedical applications

B.S. in Department of Materials Science and Engineering, Seoul National University, Seoul, Korea

RESEARCH FIELDS

Seoul National University, Seoul, Korea

Doctoral thesis research

Advisor: Professor Hyoun-ee Kim

- Polyurethane synthesis and chemically modifying technique : grafting a new functional groups for biologically improved polyurethane system
- Composite fabrication : fabrication of homogeneous polymer/ceramic composite
- Biological evaluation : in vitro cell test (attachment, proliferation, differentiation), in vivo animal test (full-thickness excision model, fibrous capsule model, calvarial defect model, etc)
- Material analysis : characterization (SEM, XRD, CLSM, UV spectroscopy, FT-IR,

Image J), mechanical property (UTM; compression, tensile, cyclic test, lap shear), *in vivo* animal study (micro CT, Histological evaluation)

PUBLICATIONS

1. **Song, E. H.**, Cho, K. I., Kim, H. E., & Jeong, S. H. (2017). Biomimetic Coating of Hydroxyapatite on Glycerol Phosphate-Conjugated Polyurethane via Mineralization. *ACS Omega*, 2(3), 981-987.
2. Park, J. U., Jung, H. D., **Song, E. H.**, Choi, T. H., Kim, H. E., Song, J., & Kim, S. (2017). The accelerating effect of chitosan-silica hybrid dressing materials on the early phase of wound healing. *Journal of Biomedical Materials Research Part B: Applied Biomaterials*, 105(7), 1828-1839.
3. **Song, E. H.**, Jeong, S. H., Park, J. U., Kim, S., Kim, H. E., & Song, J. (2017). Polyurethane-silica hybrid foams from a one-step foaming reaction, coupled with a sol-gel process, for enhanced wound healing. *Materials Science and Engineering: C*, 79, 866-874.
4. Seong, Y. J., Kang, I. G., **Song, E. H.**, Kim, H. E., & Jeong, S. H. (2017). Calcium Phosphate-Collagen Scaffold with Aligned Pore Channels for Enhanced Osteochondral Regeneration. *Advanced healthcare materials*, 6(24), 1700966.
5. Park, J. U., Jeong, S. H., **Song, E. H.**, Song, J., Kim, H. E., & Kim, S. (2018). Acceleration of the healing process of full-thickness wounds using hydrophilic chitosan-silica hybrid sponge in a porcine model. *Journal of biomaterials applications*, 32(8), 1011-1023.
6. Jeong, S. H., Shin, D. Y., Kang, I. K., **Song, E. H.**, Seong, Y. J., Park, J. U., & Kim, H. E. (2018). Effective Wound Healing by Antibacterial and Bioactive Calcium-

Fluoride-Containing Composite Hydrogel Dressings Prepared Using In Situ Precipitation. *ACS Biomaterials Science & Engineering*.

7. Park, J. U., **Song, E. H.**, Jeong, S. H., Song, J., Kim, H. E., & Kim, S. (2018). Chitosan-Based Dressing Materials for Problematic Wound Management. In *Novel Biomaterials for Regenerative Medicine* (pp. 527-537). Springer, Singapore.
8. **Song, E. H.**, Seong, Y. J., Kim, J., Kim, H. E., & Jeong, S. H. (2018). Multilayered Polyurethane–Hydroxyapatite Composite for Meniscus Replacements. *Macromolecular Materials and Engineering*, 1800352.
9. Shin, D. Y., Cheon, K. H., **Song, E. H.**, Seong, Y. J., Park, J. U., Kim, H. E., & Jeong, S. H. (2018). Fluorine-ion-releasing injectable alginate nanocomposite hydrogel for enhanced bioactivity and antibacterial property. *International journal of biological macromolecules*.
10. **Song, E. H.**, Seong, Y. J., Park, C., Kang, I. G., Kim, H. E., & Jeong, S. H. (2018). Use of thioglycerol on porous polyurethane as an effective theranostic capping agent for bone tissue engineering. *Journal of biomaterials applications*, 0885328218817173.